

Augusto César Caligula do Espírito Santo Pedreira

**Análise da Distribuição Energética Espectral do  
objeto multi-mensageiro  
GRB170817A/GW170817**

Brasil

Janeiro de 2019



Augusto César Caligula do Espírito Santo Pedreira

**Análise da Distribuição Energética Espectral do objeto  
multi-mensageiro GRB170817A/GW170817**

Dissertação apresentada ao programa de Pós-Graduação em Física da Universidade Federal do Rio Grande como requisito para a obtenção do título de mestre em Física.

Universidade Federal do Rio Grande – FURG

Instituto de Matemática, Estatística e Física – IMEF

Programa de Pós-Graduação em Física – PPG-Física

Orientador: Dr. Cristian Giovanny Bernal

Coorientador: Dr. Nissim Illich Fraija Cabrera

Brasil

Janeiro de 2019

## Ficha catalográfica

P371a Pedreira, Augusto César Caligula do Espírito Santo.  
Análise da distribuição energética espectral do objeto  
multi-mensageiro GRB170817A/GW170817 / Augusto César Caligula  
do Espírito Santo Pedreira. – 2019.  
107 f.

Dissertação (mestrado) – Universidade Federal do Rio Grande –  
FURG, Programa de Pós-Graduação em Física, Rio Grande/RN,  
2019.  
Orientador: Dr. Cristian Giovanny Bernal.  
Coorientador: Dr. Nissim Illich Fraija Cabrera.

1. Erupção de Raios Gama: Individual (GRB170817A) 2. Dados  
Físicos e Processos: Aceleração de Partículas 3. Dados Físicos e  
Processos: Mecanismos de Radiação: Não-Térmico 4. Meio  
Interestelar: Geral - Campos Magnéticos 5. Estrelas: Neutrons  
I. Bernal, Cristian Giovanny II. Cabrera, Nissim Illich Fraija III. Título.

CDU 52:539.184.2

Catalogação na Fonte: Bibliotecário José Paulo dos Santos CRB 10/2344

Augusto César Caligula do Espírito Santo Pedreira

## **Análise da Distribuição Energética Espectral do objeto multi-mensageiro GRB170817A/GW170817**

Dissertação apresentada ao programa de Pós-Graduação em Física da Universidade Federal do Rio Grande como requisito para a obtenção do título de mestre em Física.

Trabalho aprovado. Brasil, 18 de janeiro de 2019:

---

**Dr. Cristian Giovanny Bernal**  
Orientador

---

**Dr. Nissim Illich Fraija Cabrera**  
Banca

---

**Dr. Cristiano Brenner Mariotto**  
Banca

Brasil  
Janeiro de 2019



*Este trabalho é dedicado a todos os obstáculos com que nos deparamos em nossas jornadas, pois adversidade é o molde de um carácter de valor.*



# Agradecimentos

Nossa jornada como pessoa nos leva a uma estrada longa e difícil. Nessa caminhada, de solas nuas, através destas trilhas permeadas de espinhos nós dependemos dos ombros alheiros para sobrevivência, pois não há um que consiga carregar sozinho o peso do mundo em suas costas. Em minha jornada, muitos foram aqueles que me emprestaram seus ombros, me acolheram e me motivaram em tempos de dificuldade.

Primeiramente, agradeço a minha mãe, Sônia, sem qual jamais teria se quer ter tido a oportunidade de perseguir as estrelas. Sua força de carácter, bondade e resistência foram sempre o meu Norte como pessoa.

Em segundo, agradeço a meus amigos os quais me levantaram sempre que tropecei. Sem o apoio destes, nada teria acontecido. A Renato, Pedro, Gustavo, Walas, Abel, Laura, Geferson e todos os muitos outros que encontrei pelo caminho, eu vos saúdo.

Aos excelentíssimos Professores, a base intelectual de minha jornada, e orientadores Cristian Giovanny Bernal e Nissim Fraija que abriram-me as portas do mundo científico, criaram as oportunidades e acreditaram em mim em todos os momentos.

Agradeço também a todos os obstáculos em que esbarrei ao longo da minha vida, que moldaram quem eu sou hoje e me permitiram compreender as qualidades necessárias para superar a tragédia da vida.

Finalmente, agradeço à CAPES e à UNAM-DGAPA-PAPIIT. Fundações que financiaram esta pesquisa através do Código de Finança 001 e projetos IA102917 e IA102019, respectivamente.



*Igne Natura Renovatur Integra*



# Resumo

A Curta Erupção de Raios Gamma GRB170817A, detectado pelo Fermi Gamma-Ray Burst Monitor, satélites orbitais e telescópios terrestres, foi a contraparte eletromagnética de um transiente de onda gravitacional (GW170817) originado na fusão de um sistema binário de estrelas de nêutrons. Após esta fusão, a curva de luz em Raios Gama apresentou um pico fraco em  $\sim 1.7$  s enquanto outros comprimentos de onda como os Raios X, Óptico e Rádio demonstraram uma emissão estendida com brilho crescente até  $\sim 160$  dias. Neste trabalho nós mostramos que os fluxos de Raios X, Óptico e Rádio são consistentes com um modelo de sincrotron em choque dianteiro, visto fora do eixo, quando o fluxo de matéria é parametrizado através de uma distribuição de velocidades em lei de potência. Nós discutimos a origem do pico de Raios Gama em termos de choques internos e externos e mostramos que o fluxo de Raios Gama pode ser consistente com um modelo choque reverso com Síncrotron Auto-Compton quando observado em altas latitudes. Finalmente, comparando os valores de melhor ajuste encontrados após descrever os fluxos de Raios Gama, Raios X, Óptico e Rádio, através de Cadeias de Markov em Monte Carlo, com nosso modelo nós encontramos que o pós-brilho e a emissão gama ocorreram em diferentes regiões. Além disso, também encontramos evidência que sugere que o ambiente progenitor estivesse entranhado com campos magnéticos e, por sua vez, argumentar a existência de uma amplificação magnética na fusão do sistema binário.

**Palavras-chaves:** Erupção de Raios Gama: individual (GRB170817A). Dados físicos e processos: aceleração de partículas. Dados físicos e processos: mecanismos de radiação: não-termico. Meio Interestelar: Geral - Campos Magnéticos. Estrelas: Neutrons



# Abstract

The short GRB 170817A, detected by the Fermi Gamma-ray Burst Monitor, orbiting satellites and ground-based telescopes, was the electromagnetic counterpart of a gravitational-wave transient (GW170817) from a binary neutron star merger. After this merger the Gamma-Ray light curve exhibited a faint peak at  $\sim 1.7$  s and the X-Ray, Optical and Radio light curves displayed an extended emission which increased in brightness up to  $\sim 160$  days. In this work, we show that the X-Ray, Optical and Radio fluxes are consistent with the synchrotron forward-shock model viewed off-axis when the matter in the outflow is parametrized through a power law velocity distribution. We discuss the origin of the Gamma-Ray peak in terms of internal and external shocks and show that the Gamma-Ray flux might be consistent with a synchrotron self-Compton reverse-shock model observed at high latitudes. Comparing the best-fit values found, via Markov Chain Monte Carlo simulations, after describing the Gamma-Ray, X-Ray, Optical and Radio fluxes with our model, we find compelling that the afterglow and gamma-ray emissons occured in different regions and also evidence to propose that the progenitor environment was entrained with magnetic fields and, therefore, to argue a magnetic field amplification in the binary neutron star merger.

**Key-words:** Gamma-Ray Bursts: individual (GRB170817A). Physical Data and Processes: particle acceleration. Physical Data and Processes: radiation mechanism: nonthermal. Interstellar Medium: general - magnetic fields. Stars: Neutrons



# Listas de ilustrações

Figura 1 – Relação entre classificação temporal e propriedades físicas dos progenitores.	28
Figura 2 – Estrutura básica de um GRB, incluindo máquina central, jato e zonas de emissão . . . . .	29
Figura 3 – Evolução do sistema NS-NS gerador do evento GRB170817A/GW170817	33
Figura 4 – Curva de Luz e limites superiores na faixa de energia 10 - 1000 keV do GRB170817A, dados obtidos pelo GBM. A linha vermelha corresponde ao melhor ajuste utilizando a função $F(t) \propto \left(\frac{t-t_0}{t_0}\right)^{-\alpha} e^{-\frac{\tau}{t-t_0}}$ (Vestrand et al., 2006). . . . .	37
Figura 5 – Acima: SEDs das observações <i>afterglow</i> de Raios-X, Óptico e Rádio às $15 \pm 2$ (vermelho), $110 \pm 5$ (verde) e $145 \pm 20$ (azul) dias. Abaixo: Curvas de luz de Raios-X à 1 keV (dourado) (Troja et al., 2017; Margutti et al., 2018; Haggard; Nynka; Ruan, 2018; Margutti et al., 2017), Óptico (azul) (Margutti et al., 2018) e Rádio nas bandas 3 e 6 GHz (magenta) (Troja et al., 2017; Hallinan et al., 2017; Alexander et al., 2018). Os valores que descrevem tanto o SED quanto as curvas de luz são reportados na Tabela 3. . . . .	47
Figura 6 – Cornerplot apresentando os resultados obtidos nas simulações MCMC para cada parâmetro. Resultado do ajuste para os dados de Raios $\gamma$ do GBM utilizando um modelo de SSC em <i>reverse shock</i> para uma densidade homogênea como descrito em 3.1. A legenda acima de cada gráfico indica a mediana, 0.15 e 0.85 <i>quantiles</i> de cada parâmetro. O valor de melhor ajuste é mostrado em cor verde. . . . .	49
Figura 7 – Idem à Fig. 6, mas usando um modelo de síncrotron em <i>forward shock</i> para ajustar os dados de Rádio (3 GHz) quando o jato produzindo a emissão <i>afterglow</i> não está alinhado com a linha de visão do observador e a matéria no escoamento é parametrizada através de uma distribuição de velocidades de lei de potências. Modelo descrito em 3.2. . . . .	51
Figura 8 – Idem à Fig. 7, mas usando um modelo de síncrotron em <i>forward shock</i> para ajustar os dados de Rádio (6 GHz) quando o jato produzindo a emissão <i>afterglow</i> não está alinhado com a linha de visão do observador e a matéria no escoamento é parametrizada através de uma distribuição de velocidades de lei de potências. Modelo descrito em 3.2. . . . .	52

Figura 9 – Idem à Fig. 8, mas usando um modelo de síncrotron em *forward shock* para ajustar os dados de Raios-X quando o jato produzindo a emissão *afterglow* não está alinhado com a linha de visão do observador e a matéria no escoamento é parametrizada através de uma distribuição de velocidades de lei de potências. Modelo descrito em 3.2. . . . . 53

# Lista de tabelas

Tabela 1 – Análise Espectral dos dados do GBM . . . . .	35
Tabela 2 – Valores ajustados para os dados de raios $\gamma$ . minimização Chi quadrado ( $\chi^2$ / n.g.l.) é reportada em parênteses . . .	38
Tabela 3 – Valores ajustados para os dados de Raios-X, Óptico e Rádio. minimizações Chi-Quadrado ( $\chi^2$ / n.d.f.) são reportadas entre parênteses	44
Tabela 4 – A mediana e <i>quantiles</i> simétricos (0.15, 0.5, 0.85) como encontrados após descrever o pico de Raios $\gamma$ do GBM com nosso modelo. . . . .	48
Tabela 5 – A mediana e <i>quantiles</i> simétricos (0.15, 0.5, 0.85), truncados na segunda casa decima, como encontrados após descrever os Raios-X e Rádio em 3 e 6 GHz com nosso modelo. . . . .	50



# Lista de abreviaturas e siglas

GRB	Gamma Ray Burst.
sGRB	Gamma Ray Burst Curtos.
lGRB	Gamma Ray Burst Longos.
Fermi-GBM	Fermi Gamma Ray Burst Monitor.
CGRO	Compton-Gamma-Ray-Observatory.
ICM	Circumburst Medium.
IC	Inverse Compton.
NS	Neutron Star.
GW	Gravitational Wave.
BH	Black Hole.
SN	Supernova.
SNe	Supernovae.
ISM	Interstellar Medium.
SSC	Synchrotron Self-Compton.
LAT	Large Area Telescope.
IR	Infrared.
SSC	Synchrotron Self Compton.
LIGO	Large Interferometer Gravitational-Wave Observatory.
SED	Spectral Energy Distribution.
MCMC	Markov Chain Monte Carlo.
TTE	Time-Tagged Event.
CPL	Comptonized Power Law.
PL	Power law.



# Listas de símbolos

$\gamma$	Letra grega gama. Representa a faixa de comprimentos de onda equivalente aos Raios Gama.
eV	Electron-Volt. Unidade de energia. Pode vir acompanhado dos respectivos modificadores: kilo (k), Mega (M) e Giga (G).
$T_{90}$	Escala temporal utilizada em GRBs.
$\gtrsim$	Aproximadamente maior que.
$M_{\odot}$	Massa Solar.
ergs	Do grego ergon. Unidade de energia e trabalho.
$\approx$	Aproximadamente proporcional à.
pc	Parsec. Paralaxe anual. Unidade de distância astronômica.
$\Gamma$	Letra grega gama maiúscula. Representa o Fator de Lorentz de grupo, do sistema em estudo como um tudo.
G	Gauss. Unidade de densidade de campo magnético.
$\theta_{obs}$	Ângulo de observação.
$\theta_j$	Ângulo de abertura do jato.
J200	Ano Juliano 2000. Utilizado para determinar o equinócio do sistema de coordenadas equatorial.
RA	<i>Right Ascencion</i> . Ascensão Reta, coordenada azimutal do sistema de coordenadas equatorial.
DEC	<i>Declination</i> . Declinação, valor angular utilizado para determinar a posição de um astro no sistema de coordenadas equatorial.
NaI	Iodeto de Sódio.
$E_{\gamma,iso}$	Energia isotrópica correspondente a energia de corte da emissão $\gamma$ .
$F_{\nu}$	Fluxo em termos da frequência.
$t_0$	Tempo inicial.
$\tau$	Escala temporal de crescimento do fluxo.

$\alpha_\gamma$	Índice de potência do decaimento rápido.
$E_{peak}$	Energia do pico.
$\delta t_{var}$	Escala temporal de variabilidade.
$F_{obs}$	Fluxo observado.
$p$	Índice espectral para choques externos.
$\epsilon^{syn,off}$	Quebra espectral para síncrotron visto fora do eixo.
$\epsilon^{SSC,off}$	Quebra espectral para SSC visto fora do eixo.
$\epsilon^{syn,on}$	Quebra espectral para síncrotron visto no eixo.
$\epsilon^{SSC,on}$	Quebra espectral para SSC visto no eixo.
$B$	Campo magnético.
$\gamma_e$	Fator de Lorentz dos elétrons.
$U_e$	Densidade de energia fornecida para acelerar elétrons.
$N_e$	Densidade de número de elétrons.
$N_p$	Densidade de número de prótons.
$\gamma_s h$	Fator de Lorentz relativo através do choque interno.
$m_p$	Massa do próton.
$\gamma_{e,mi}$	Fator de Lorentz mínimo dos elétrons.
$\gamma_{e,ma}$	Fator de Lorentz máximo dos elétrons.
$L_j$	Luminosidade do jato.
$\epsilon_{pk}^{SSC,on}$	Energia de pico para radiação síncrotron vista no eixo.
$\varepsilon_e$	Fração de energia fornecida para acelerar elétrons.
$\varepsilon_B$	Fração de energia fornecida para gerar ou amplificar o campo magnético.
$b$	Parâmetro de reescalamento entre emissão no eixo e fora do eixo.
$\Delta\theta$	Diferença entre ângulo de observação e ângulo de abertura do jato.
$\gamma_{m,f}$	Fator de Lorentz mínimo para o caso de forward shock.
$\gamma_{c,f}$	Fator de Lorentz de resfriamento para o forward shock.

$\epsilon_{m,f}^{syn,off}$	Quebra espectral mínima de síncrotron no forward shock.
$\epsilon_{c,f}^{syn,off}$	Quebra espectral de resfriamento de síncrotron no forward shock.
$\epsilon_{m,f}^{SSC,off}$	Quebra espectral mínima de SSC no forward shock.
$\epsilon_{c,f}^{SSC,off}$	Quebra espectral de resfriamento de SSC no forward shock.
$\gamma_{m,r}$	Fator de Lorentz mínimo para o caso de forward shock.
$\gamma_{c,r}$	Fator de Lorentz de resfriamento para o forward shock.
$E$	Equivalente isotrópico da energia cinética.
$\eta$	Eficiência cinética.
$\epsilon_{m,r}^{syn,off}$	Quebra espectral mínima de síncrotron no reverse shock.
$\epsilon_{c,r}^{syn,off}$	Quebra espectral de resfriamento de síncrotron no reverse shock.
$\epsilon_{m,r}^{SSC,off}$	Quebra espectral mínima de SSC no reverse shock.
$\epsilon_{c,r}^{SSC,off}$	Quebra espectral de resfriamento de SSC no reverse shock.
$t_{cr}$	Tempo de cruzamento do choque.
$n$	Densidade numérica do ICM.
$\gamma_{34}$	Fator de Lorentz relativo entre as regiões com sentido de propagação contrários.
$\Gamma_r$	Fator de Lorentz de grupo para o reverse shock.
$\epsilon_\gamma$	Energia de quebra característica.
Jy	Jansky. Unidade de fluxo.
$\beta\Gamma$	Multipliação entre velocidade em unidades de velocidade da luz e o fator de Lorentz.
$\tilde{E}$	Energia fiducial.
$R$	Raio de desaceleração.
$k$	Parâmetro de correlação entre os tempos de pico de fluxo e jet break, através dos valores ângulares.
$H_0$	Constante de Hubble.
$\Omega_m$	Parâmetro de densidade de matéria.
$\Omega_\lambda$	Parâmetro de densidade de energia escura.



# Sumário

<b>1</b>	<b>INTRODUÇÃO</b>	<b>27</b>
1.1	<b>Erupções de Raios Gama: GRBs</b>	27
1.2	<b>GRBs Curtos</b>	31
1.3	<b>17/08/17: A Mina de Ouro da Astrofísica Multi-mensageira</b>	32
1.4	<b>Objetivos e Justificativas</b>	33
<b>2</b>	<b>REDUÇÃO DE DADOS</b>	<b>35</b>
2.1	<b>Cadeias de Markov em Monte Carlo (MCMC)</b>	36
<b>3</b>	<b>RESULTADOS E ANÁLISE</b>	<b>37</b>
3.1	<b>Modelando o Fluxo de Raios Gama</b>	37
3.1.1	Análise e Descrição da Curva de Luz	37
3.1.2	Modelo Teórico	42
3.2	<b>Modelando os Fluxos de Raios-X, Óptico e Rádio</b>	43
3.2.1	Análise e Descrição da Curva de Luz	43
3.2.2	Modelo Teórico	45
3.3	<b>Cadeias de Markov em Monte Carlo (MCMC)</b>	48
3.4	<b>Análise e Implicações</b>	54
3.4.1	Os parâmetros microfísicos magnéticos	54
3.4.2	Outros Parâmetros	55
<b>4</b>	<b>CONCLUSÕES E PERSPECTIVAS</b>	<b>57</b>
	<b>REFERÊNCIAS</b>	<b>61</b>
	<b>ANEXO A – ARTIGOS ACEITOS PARA PUBLICAÇÃO</b>	<b>71</b>



# 1 Introdução

## 1.1 Erupções de Raios Gama: GRBs

Um dos eventos extragaláticos mais fascinantes já observados são as Erupções de Raios Gama (do inglês *Gamma Ray Burst*, GRB). GRBs são pulsos irregulares, altamente relativísticos, de radiação gama (representado pelo símbolo  $\gamma$ ) com um espectro não-térmico e ponto máximo em  $10 - 10^4$  keV (Band et al., 1993; Meegan et al., 1992). Baseado em durações e dureza espectral<sup>1</sup> padrões, dois tipos de populações progenitoras são amplamente aceitas, curtos (sGRBs,  $T_{90}^2 < 2$  s) e longos (lGRBs,  $T_{90} > 2$  s) (Zhang; Mészáros, 2004; Kumar; Zhang, 2015). Recentes observações confirmaram que lGRBs são um dos possíveis resultados do colapso de estrelas massivas ( $\gtrsim 15 M_\odot$ ) e que, pelo menos alguns dos sGRBs surgem da fusão de objetos compactos (estrelas de nêutrons ou buracos negros estelares) em sistemas binários, como demonstrado na Figura 1.

Até o lançamento do *Compton-Gamma-Ray-Observatory* (CGRO), as distâncias dos GRBs observados eram um ponto de incerteza. Este observatório, em órbita da Terra de 5 de Abril de 1991 à 4 de Junho de 2000, estabeleceu que estas erupções estão distribuídas isotropicamente (Meegan et al., 1992) e que seus números desviam da contagem Euclidiana esperada<sup>3</sup>,  $N(> f) \propto f^{-3/2}$  (Mao; Paczynski, 1992; Piran, 1992). Estas descobertas convenceram os astrônomos que GRBs são, de fato, eventos extragaláticos.

Em 28 de Fevereiro de 1997 uma emissão em Raios-X e Óptico foi detectada um dia após a emissão de Raios  $\gamma$  de um GRB. Esta emissão foi nomeada de pós-brilho (do inglês *afterglow*) (Costa et al., 1997; Frontera et al., 1998). O estudo do *afterglow* trouxe uma nova era na análise de GRBs que permitiu uma compreensão muito mais profunda sobre estas erupções enigmáticas e altamente energéticas.

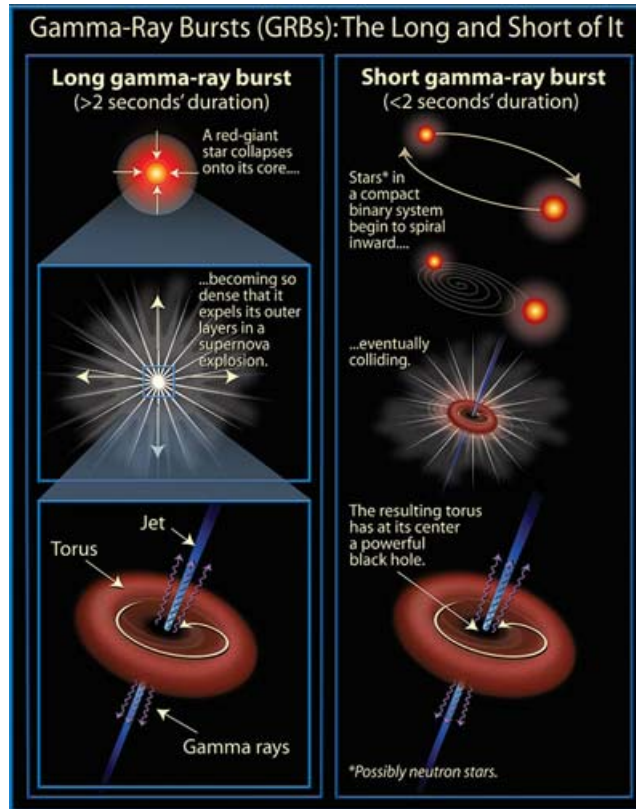
Através do estudo de *afterglow* foi descoberto que, pelas quebras nas curvas de luz (quebras espectrais, uma mudança brusca na curva de luz caracterizando uma modificação no perfil da curva) de Raios-X e Óptico, que os GRBs são altamente colimados (Rhoads, 1999; Sari; Piran, 1995) e que a energia emitida nessas erupções é da faixa de  $10^{48} - 10^{52}$  ergs (Frail et al., 2001; Panaiteescu; Kumar, 2001; Berger; Kulkarni; Frail, 2003; Curran;

<sup>1</sup> Análogo à cor para radiação visível, quanto mais duro o espectro, menor o comprimento de onda e maior a frequência.

<sup>2</sup> Escala temporal utilizada para GRBs. Representa a duração em que 90% das contagens foram observadas.

<sup>3</sup> Considere fontes de mesma luminosidade intrínseca,  $L$ , uniformemente distribuídas em um espaço Euclidiano. O fluxo observado decai com a distância  $R$  em  $R^{-2}$  e o número total de fontes contidas em  $R$  cresce com  $R^3$ . O fluxo observado destas fontes é  $> f = \frac{L}{4\pi R^2}$ . Então o número total de objetos observados como fluxo descrito escala como  $f^{-3/2}$ .

Figura 1 – Relação entre classificação temporal e propriedades físicas dos progenitores.

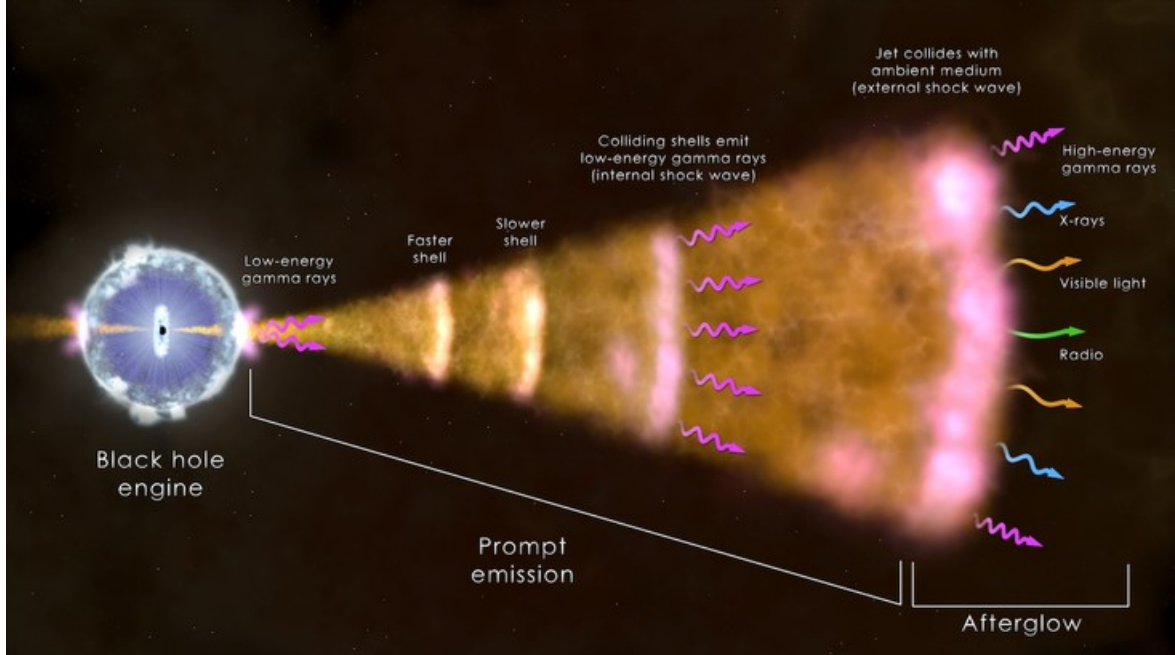


Fonte: ([NASA, 2006](#))

[van der Horst; Wijers, 2008; Liang et al., 2008; Racusin et al., 2009; Cenko et al., 2010](#)). O estudo destes comprimentos de onda mais longos também estabeleceu que as curvas de luz (fluxo integrado por tempo) do *afterglow* normalmente decaem no tempo com uma lei de potência ( $F_\nu \propto t^{-1.0}$ ) e tem um espectro (fluxo integrado em todos os comprimentos de onda) de lei de potência ( $F_\nu \propto \nu^{-0.9 \pm 0.5}$ ). A radiação síncrotron de um choque dianteiro (do inglês *forward shock*) externo - resultante da interação do material ejetado pelo GRB com o meio circum-explosão (do inglês *circumburst medium*, ICM) - fornece um ajuste particularmente bom para os dados de múltiplos comprimentos de onda do *afterglow* de GRBs ([Panaitescu; Kumar, 2002](#)).

Esse estudo do *afterglow* levou à criação de um contexto geral para GRBs. Como visto na Figura 2, a estrutura de um GRB é tal que contém uma máquina central, carregando um forte campo gravitacional, que ejeta um fluxo ultra relativístico composto de léptons e bósons. Enquanto a estrutura do jato em si ainda não é perfeitamente descrita, os modelos de choques externos atuais consideram que, após a interação do jato com o meio ambiente ao redor, ondas de choque se formam e propagam em direções opostas. Uma continua se propagando em direção ao meio interestelar, o *forward shock* e outra propaga em direção ao interior do jato, o *reverse shock*. O *forward shock* normalmente possui um tempo de vida longo e continua se propagando, interagindo com o ISM e

Figura 2 – Estrutura básica de um GRB, incluindo máquina central, jato e zonas de emissão



Fonte: ([CENTER, 2015](#))

eventualmente formando o *afterglow*. Apesar de ser necessário uma análise mais profunda para obter o exato processo de emissão, o processo síncrotron, a emissão de fótons causada pela aceleração radial de partículas carregadas, é o modelo mais utilizado, devido sua simplicidade e elegância.

O *reverse shock*, por sua vez, tende a ter pouca duração devido ao fato de que se propaga em sentido oposto ao jato. Os processos de emissão tendem a ser mais complexos de se especificar devido a grande quantidade possíveis de emissões que podem ser causadas pelo *reverse shock*, desde rajadas de luz Óptica/IR e erupções de Rádio na estrutura de uma emissão síncrotron até Fótons sub-GeV, neutrinos ultra energéticos e emissões de Raios-X e Raios  $\gamma$  em modelos que consideram a emissão com Síncrotron Auto-Compton (do inglês *Synchrotron Self Compton*, SSC) — O espalhamento Compton Inverso de um fóton gerado por um processo síncrotron — ou Compton Inverso entre os elétrons e fótons das diferentes zonas de choque. De tal maneira o *reverse shock* normalmente requer uma análise mais cuidadosa.

Em muitos casos, o decaimento da curva de luz do *afterglow* para Raios-X e Óptico se acentua para  $F_\nu \propto t^{-2.2}$  em  $\sim 1$  dia após a erupção. A explicação mais natural para essa acentuação é que isto ocorre devido à colimação do fluxo e a natureza angular finita do material ejetado que leva a um decaimento acromático mais rápido para as curvas de luz de Raios-X e Óptico. Essa transição acromática de um decaimento lento para um rápido é chamado de "quebra de jato" (do inglês *jet break*).

Evidências sugerem que os fótons de alta energia (100 MeV) observados durante a fase imediata ( $t \gtrsim 10$  s) são produzidos no *forward shock* externo via o processo de síncrotron (Kumar; Barniol Duran, 2009). Por outro lado os processos que levam à origem da emissão de Raios  $\gamma$ , seja em altas ou baixas energias, ainda são pontos de debate. Alguns dos modelos propostos são: Síncrotron e Compton Inverso (do inglês *Inverse-Compton*, IC) ocorrentes em choques, internos ou externos, ou em locais onde o campo magnético no jato de *Poynting*<sup>4</sup> é dissipado (Rees; Meszaros, 1992; Zhang; Yan, 2011); e radiação fotosférica com contribuição de múltiplos espalhamentos IC (Thompson, 1994; Ghisellini; Celotti, 1999; Pe'er, 2008; Giannios; Spruit, 2007; Ioka et al., 2007). Outros parâmetros de interesse foram encontrados através do estudo do *afterglow*. O ângulo de abertura inicial, por exemplo, e a energia cinética puderam ser encontradas modelando a emissão em banda larga (Rádio até Raios-X). O ângulo de abertura é estimado de estar no intervalo de 2 – 10 graus, de maneira que a colimação equivalente diminui o orçamento energético em um fator de  $10^2 - 10^3$  para o caso isotrópico. O meio dentro de um raio de  $\sim 0.1$  pc da erupção é estimado de ter densidade numérica uniforme, em muitos casos, na ordem de alguns prótons por  $\text{cm}^3$  (Panaitescu; Kumar, 2002). Este resultado em particular é surpreendente considerando o progenitor assumido para lGRBs, os colapsos de estrelas supermassivas, onde se espera que a densidade caia com a distância do centro por  $r^{-2}$  devido os ventos da estrela progenitora (Dai; Lu, 1998; Chevalier; Li, 1999).

As evidências da associação de lGRBs com SNe de colapso nuclear vem de dois tipos de observações:

- lGRBs são tipicamente encontrados em regiões de formação estelar em suas galáxias hospedeiras. (Bloom et al., 2002)
- Para vários lGRBs, SNe de tipo Ic foram detectadas espectroscopicamente e associadas com os eventos. A maioria destes lGRBs associados com SN possuem luminosidade significativamente mais baixa que os valores típicos, e.g. GRB980425<sup>5</sup> (Galama et al., 1998), GRB030329 (Hjorth et al., 2003; Stanek et al., 2003), GRB060218 (Modjaz et al., 2006; Campana et al., 2006; Pian et al., 2006), GRB100316D (Chornock et al., 2010; Starling et al., 2011), GRB101219B (Sparre et al., 2011) e GRB120422A (Melandri et al., 2012). Adicionalmente, aproximadamente uma dúzia de GRBs demonstram, em períodos tardios ( $\sim 10$  dias), uma "saliência" no sinal Óptico simultaneamente à uma mudança de cor inconsistente com emissão síncrotron, o que sugere que um fluxo Óptico da SN subjacente está começando a superar o fluxo do *afterglow* (Bloom et al., 1999).

---

<sup>4</sup> Um Jato de *Poynting* é a definição fornecida para quando a matéria num jato é negligível e a energia e momento angular são propagados predominantemente pelo campo eletromagnético.

<sup>5</sup> A nomenclatura padrão para GRBs é do tipo Ano/Mês/Dia.

## 1.2 GRBs Curtos

Enquanto a descoberta e subsequente estudo dos IGRBs foi marcada por sucessos, o estudo de sGRBs provou ser muito mais desafiante. Similarmente aos IGRBs, avanços significantes vieram através da observação de galáxias hospedeiras e do estudo de *afterglow* em múltiplos comprimentos de onda (Zhang; Mészáros, 2004). Múltiplas evidências permitiram associar progenitores de sGRBs com a fusão de sistemas binários de objetos compactos, compreendidos de Estrelas de Nêutrons (do inglês *Neutron Star*, NS) ou NS-Buraco Negro (do inglês *Black Hole*, BH) (Eichler et al., 1989; Narayan; Paczynski; Piran, 1992; Lee; Ramirez-Ruiz, 2007; Lee; Ramirez-Ruiz; Page, 2004; Lee et al., 2005; Nakar, 2007). Estes progenitores são possíveis candidatos para a formação de Ondas Gravitacionais (do inglês *Gravitational Wave*, GW) acompanhadas por sua contraparte Óptica/Infravermelha isotrópica, conhecida como kilonova ou macronova (Li; Paczyński, 1998; Rosswog, 2005; Metzger et al., 2010; Kasen; Badnell; Barnes, 2013; Metzger; Berger; Margalit, 2017). Devido a riqueza de nêutrons no material ejetado por estes progenitores, uma kilonova/macronova é produzida via decaimento radioativo de núcleos pesados e instáveis criados na nucleossíntese de captura neutrônica rápida (Processo r) (Lattimer; Schramm, 1974; Lattimer; Schramm, 1976). Adicionalmente, emissão tardia em Rádio, originada da interação do material ejectado pela fusão com o ICM, é esperada neste tipo de evento. (Nakar, 2007; Piran; Nakar; Rosswog, 2013; Hotokezaka; Piran, 2015a).

Usando um sistema binário NS onde as estrelas não possuem rotação, estão magnetizadas, separadas inicialmente a uma distância de 48 km e com  $1.4 M_{\odot}$ , os autores (Price; Rosswog, 2006) apresentaram, através de simulações computacionais, a evolução do campo magnético durante a fusão de um sistema NS-NS. O principal resultado é que o campo magnético correspondente, de  $\sim 10^{12}$  G, presente em uma NS pode ser amplificado em várias ordens de grandeza após a fusão. A magnitude do campo magnético que pode ser obtida durante os primeiros milissegundos, através de instabilidades de Kelvin-Helmholtz e turbulência, é muito maior que  $\sim 10^{15}$  G (Price; Rosswog, 2006; Zrake; MacFadyen, 2013; Giacomazzo; Rezzolla; Baiotti, 2009; Obergaulinger; Aloy; Müller, 2010; Fraija et al., 2017). Desta maneira, pode-se esperar que exista magnetização no material ejetado num cenário de fusão de NS.

Utilizando uma casca em *reverse shock*, e as suposições padrões para este processo, os picos brilhantes de Raios  $\gamma$ , Raios-X e Óptico exibidos durante as fases imediata e inicial do *afterglow* foram interpretados em modelos com base de radiação síncrotron (Chevalier; Li, 2000; Zhang; Kobayashi; Mészáros, 2003; Zhang; Kobayashi, 2005a; Kobayashi; Zhang, 2003; Fraija; Lee; Veres, 2016) e espalhamento IC externo/SSC (Wang; Dai; Lu, 2001b; Wang; Dai; Lu, 2001a; Kobayashi et al., 2007; Fraija; González; Lee, 2012a; Fraija, 2015; Fraija et al., 2016). O resultado destas modelagens juntamente com detecção de polarização (Gorbovskoy et al., 2016; Pruzhinskaya et al., 2014; Kopač et al., 2015; Steele et al., 2009;

Mundell et al., 2007; Mundell et al., 2013; Troja et al., 2017; Fraija et al., 2017) proveram evidências suficientes que alguns progenitores de lGRBs possuem campos magnéticos intensos intrinsecamente ligados ao material ejetado (Usov, 1992; Coburn; Boggs, 2003; Wheeler et al., 2000).

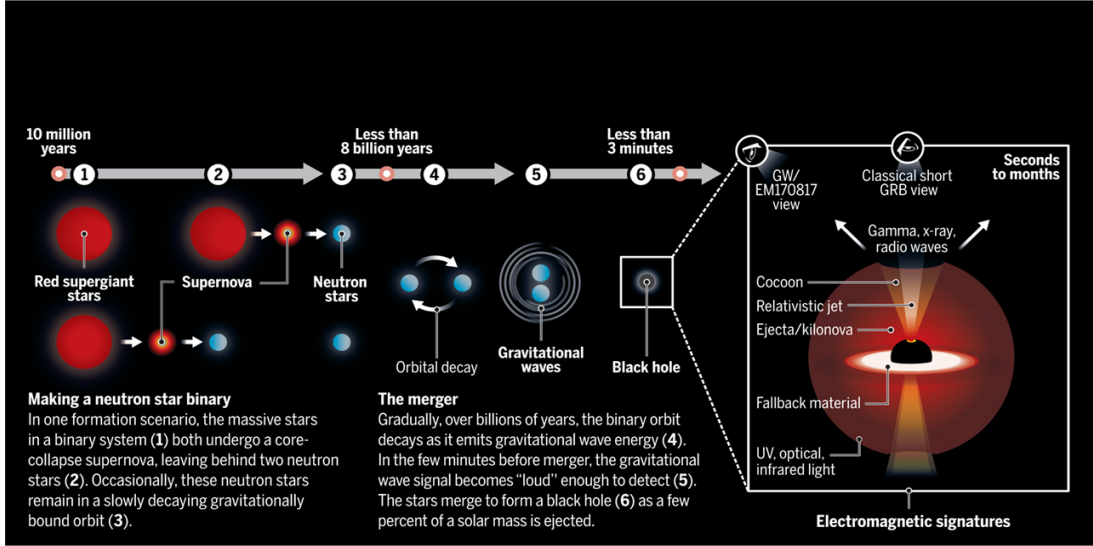
No contexto de sGRBs, (Fraija et al., 2016) propôs que o pico brilhante existente durante a fase imediata e inicial do *afterglow* pode ser correlacionado com o grau de magnetização presente no jato. Em particular, o pico apresentado na curva de luz do *Large Area Telescope* (LAT), quando interpretado num contexto de *reverse shock*, indica que a máquina central do GRB em estudo (GRB090510) era magnetizada. Similarmente, amplificação magnética na fusão do sistema binário é o modelo mais promissor.

Em contrapartida, a transição entre a emissão imediata e o *afterglow* é uma das fases mais interessantes e menos entendidas. O decaimento na fase imediata é atribuído à emissão de regiões localizadas em altas latitudes, i.e. de regiões localizadas em ângulos de observação ( $\theta_{obs}$ ) maior por pelo menos um fator  $\theta_j \sim \frac{1}{r}$  com respeito a linha de visão do observador. Este regime é conhecido como emissão de alta latitude ou efeito de curvatura. Quando este efeito está presente, após a emissão de Raios  $\gamma$  da linha de visão do observador ter terminado, o fluxo fora do eixo de observação em  $\theta_{obs} > \theta_j$  é dramaticamente suprimido se o fluxo não for extremamente luminoso ou visto próximo de suas bordas. Devido ao efeito de curvatura, a fase inicial do *afterglow* pode sobrepor a emissão de altas latitudes. Radiação gerada no *reverse shock* decairia rapidamente devido ao efeito de atraso de tempo angular (Kumar; Panaiteescu, 2000) e uma vez que a emissão de altas latitudes, que está rapidamente decaindo, for pequena o suficiente a emissão do *afterglow* pode ser observada (Dermer; Chiang; Mitman, 2000; Granot et al., 2002; Rees, 1999).

### 1.3 17/08/17: A Mina de Ouro da Astrofísica Multi-mensageira

O GRB170817A foi detectado pelo *Fermi-GBM Telescope* às 12:41:06 UTC, em 17 de Agosto de 2017 (von Kienlin; Meegan; Goldstein, 2017; Goldstein et al., 2017). Esta detecção foi consistente com o transiente de onda gravitacional encontrado pelos observatórios LIGO e Virgo. Este transiente observational foi associado com a fusão de um sistema NS-NS (GW170817) de tempo de fusão 12:41:04 UTC, aproximadamente 2 s antes da detecção reportada pelo Fermi-GBM, sendo assim o GRB170817A a contraparte eletromagnética associada à fusão (Abbott et al., 2017a; Abbott et al., 2017b). Imediatamente em seguida uma campanha exaustiva foi lançada para monitorar múltiplas bandas em busca da contraparte eletromagnética isotrópica nas faixas do Óptico e Infravermelho (Coulter et al., 2017). Figura 3 ilustra a mais provável evolução do sistema que levou a criação do evento GW170817/GRB170817A, partindo da geração do sistema binário, sua fusão e subsequente emissão eletromagnética.

Figura 3 – Evolução do sistema NS-NS gerador do evento GRB170817A/GW170817



Fonte: ([BLOOM; SIGURDSSON, 2017](#))

Um transiente brilhante na banda Óptica-i, com magnitude  $m_i = 17.057 \pm 0.0018$ , foi observado pelo telescópio *Swope* no Observatório de Las Campanas, Chile, em 17 de Agosto de 2017, 23:33 UTC e em seguida, durante as 12 horas seguintes, por múltiplos telescópios, terrestres e orbitais, na faixa Óptica/IR. Em adição, polarização linear em bandas ópticas foi reportada, revelando a geometria da região emissora. Com estas informações o transiente foi localizado vindo do centro da galáxia NGC 4993 a uma distância de 40 Mpc.

Observações distintas em Raios-X foram feitas por diversos satélites orbitais durante os 8 dias após a fusão. Detecções não foram obtidas, entretanto as observações forneceram os limites ([Margutti et al., 2017](#)). Do 9th até o 256th dia após a fusão, detecções em Raios-X foram reportadas pelos observatórios *Chandra* e *XMM-Newton* ([Troja et al., 2017; Margutti et al., 2018; Alexander et al., 2018](#)). Observações Ópticas, juntamente com seus limites superiores, foram coletadas pela *Advanced Camera for Survey's Wide Field Camera* a bordo do *Hubble Satellite Telescope* (HST) desde aproximadamente 100 dias após a centelha inicial ([Lyman et al., 2018; Margutti et al., 2018; Alexander et al., 2018](#)). No 16th dia após a centelha inicial, e por mais de 7 meses, a contraparte em Rádio (3 e 6 GHz), foi obtida pelo *Very Large Array* (VLA) ([Abbott et al., 2017b; Dobie et al., 2018; Hallinan et al., 2017](#)).

## 1.4 Objetivos e Justificativas

Com a descoberta do GRB170817A, observado de maneira minuciosa e confirmado ter um progenitor consistente com a fusão de um sistema binário NS-NS, além de ser um emissor de ondas gravitacionais, se torna bastante importante o estudo deste objeto

multi-mensageiro em todas suas épocas e bandas. Tais estudos são promissores fontes de informação sobre a fusão de sistemas binários e sGRBs - que continuam processos não totalmente compreendidos - o estado de magnetização de um sistema binário, processos radiativos, ondas gravitacionais e o diagnóstico de futuros, e passados, progenitores de GRBs.

Para nosso caso de estudo, GRB170817A, a contraparte eletromagnética do transiente de onda gravitacional, GW170817, um pico fraco foi exibido na curva de luz dos Raios  $\gamma$  após 1.7 s enquanto as curvas de luz de Raios-X, Óptico e Rádio demonstraram uma emissão estendida que aumentou em brilho até  $\sim 160$  dias. Neste trabalho, nós realizamos a construção e análise da distribuição energética espectral (do inglês, SED) demonstrando que os fluxos de Raios-X, Óptico e Rádio são consistentes com o modelo de emissão síncrotron em *forward shock* visto fora do eixo quando a matéria no fluxo é descrita por uma distribuição de velocidade parametrizada através de uma lei de potência. Nós discutimos a origem do pico de Raios  $\gamma$  em termos de choques internos e externos mostrando, também, que o fluxo de Raios  $\gamma$  pode ser consistente com um modelo de SSC em *reverse shock* observado em altas latitudes. Comparando os resultados de melhor ajuste encontrados, através de Cadeias de Markov em Monte Carlo (do inglês *Markov Chain Monte Carlo*, MCMC), após descrever os fluxos de Raios  $\gamma$ , Raios-X, Óptico e Rádio com nosso modelo, nós encontramos que o *afterglow* e emissão de Raios  $\gamma$  ocorreram em regiões diferentes, além disso, encontramos também evidências que sugerem que o ambiente progenitor estava entranhado com campos magnéticos e por sua vez, argumentar a favor de uma amplificação magnética na fusão do sistema binário.

## 2 Redução de Dados

Os arquivos de dados relacionados ao evento foram obtidos utilizando o tempo de observação do *Fermi Gamma-Ray Burst Monitor* para o GRB170817A, 04:47:43 UTC em 17 de Agosto de 2017 (von Kienlin; Meegan; Goldstein, 2017; Ackermann et al., 2013). Dados do *Fermi-GBM* foram reduzidos utilizando a base de dados pública do *Fermi Website*<sup>1</sup> e a posição desta erupção foi encontrada nas coordenadas (J2000) AR = 176°.8, DEC = −39°.8, com um erro de 11.6°. Nenhuma outra fonte no catálogo do LAT ou emissão de fundo são consideradas devido a duração do evento.

Valores de fluxo são derivados utilizando o pacote de análise espectral RMFit, versão 432<sup>2</sup>. Para analisar o sinal, nós utilizamos os arquivos de eventos marcados por tempo (do inglês *time-tagged event*, TTE) dos três detectores NaI<sup>3</sup> acionados,  $n_1$ ,  $n_2$  e  $n_5$ . Diferentes modelos espectrais são utilizados para ajustar o espectro através de diferentes períodos de duração. Cada *bin* temporal é escolhido adotando um compromisso entre o menor sinal necessário para derivar um espectro e a resolução mínima requerida para preservar a forma da evolução temporal. As funções de lei de potência Comptonizadas (uma lei de potência com valor de corte exponencial, futuramente referida como CPL) e simples (PL) são utilizadas para ajustar o espectro até 0.448 s ao redor do tempo de observação do *Fermi-GBM*. A análise espectral durante o intervalo de tempo [−0.320 s, 0.448 s] após a observação é demonstrada na Tabela 1. Esta tabela mostra o intervalo de tempo (coluna 1), modelo espectral (coluna 2), índice espectral (coluna 3), energia do pico (coluna 4), temperatura da função de corpo negro (BB) e o teste C-Stat/dof(ultima coluna)<sup>4</sup>. Após 0.512 s o espectro é melhor ajustado com um modelo de corpo negro.

Tabela 1 – Análise Espectral dos dados do GBM

Intervalo Temporal (s) <sup>a</sup>	Modelo <sup>b</sup>	$\beta$	$E_{pk}$ (keV)	kT (keV)	C-Stat/dof
[−0.320 , 0.320]	CPL	-1.016±0.293	338.3±229	-	406.64/361
[−0.320 , 0.256]	CPL	-0.955±0.309	331.6±212	-	414.34/361
[0.256 , 0.320]	PL	-1.749±0.434	-	-	296.47/362
[0.320 , 0.448]	PL	-2.150±0.472	-	-	341.51/362
[0.512 , 1024]	BB	-	-	13.84 ± 4.67	446.40/362
[1.024 , 1.536]	BB	-	-	11.78 ± 2.41	399.07/362
[1.536 , 2.048]	BB	-	-	9.480 ± 1.61	416.05/362

<sup>a</sup> Intervalo de tempo ao redor da observação inicial.

<sup>b</sup> CPL = Função Comptonizada. PL = Função de lei de potências simples. BB= Função de Corpo Negro

<sup>1</sup> <http://fermi.gsfc.nasa.gov/ssc/data>

<sup>2</sup> <https://fermi.gsfc.nasa.gov/ssc/data/analysis/rmfit/>

<sup>3</sup> Detector de radiação gama por espectroscopia com Iodeto de Sódio (NaI)

<sup>4</sup> Também chamada de Estatística de "Concordância", é uma medida da qualidade de um ajuste.

## 2.1 Cadeias de Markov em Monte Carlo (MCMC)

Para encontrarmos os valores de ajuste para os parâmetros, nós utilizamos do método da estatística Bayesiana de Cadeias de Markov em Monte Carlo (*Markov Chain Monte Carlo*, MCMC) (Hastings, 1970). O método consiste em utilizar distribuições priores e uma distribuição de probabilidades para encontrar distribuições posteriores dentro de uma amostra por meio de caminhadas aleatórias.

Considere a fórmula de Bayes

$$P(\theta|x) = \frac{P(x|\theta)P(\theta)}{P(x)}, \quad (2.1)$$

onde  $P(\theta|x)$  é a probabilidade dos parâmetros do modelo  $\theta$ , tendo os dados  $x$ ,  $P(\theta)$  a distribuição prior,  $P(x|\theta)$  a probabilidade e  $P(x)$  a evidência de que os dados  $x$  foram gerados pelo nosso modelo. Enquanto  $P(x)$  é consideravelmente difícil de se resolver, até para o caso mais simples possível, o método de MCMC nos permite construir uma Cadeia de Markov para realizar uma aproximação de Monte Carlo, simplificando drasticamente os cálculos, removendo o termo de evidência. Neste trabalho nós fazemos simulações MCMC para derivar as distribuições posteriores e valores de melhor ajuste utilizados no nosso modelo.

# 3 Resultados e Análise

## 3.1 Modelando o Fluxo de Raios Gama

### 3.1.1 Análise e Descrição da Curva de Luz

A Figura 4 mostra a curva de luz e limites superiores para os dados obtidos pelo *Fermi-GBM*, na faixa de energia de  $10 - 10^3$  keV, apesar de nenhum fluxo significante ter sido observado acima de 300 keV. A função CPL demonstrou uma energia de corte de 185 keV e a energia isotrópica correspondente obtida foi  $E_{\gamma,iso} \simeq 5 \times 10^{46}$  erg, com  $T_{90} = 2$  s (von Kienlin; Meegan; Goldstein, 2017). A curva de luz *Fermi-GBM* exibiu um pico em torno de  $\sim 1.7$  s após as observações iniciais das ondas gravitacionais, seguido por um decaimento rápido. O método de minimização Chi quadrado ( $\chi^2$ ), desenvolvido no *software* ROOT (Brun; Rademakers, 1997), foi utilizado para ajustar a curva de luz *Fermi-GBM* com a função:  $F_\nu(t) \propto \left(\frac{t-t_0}{t_0}\right)^{-\alpha_\gamma} e^{-\frac{\tau}{t-t_0}}$  (Vestrand et al., 2006), onde  $t_0$  é o tempo inicial,  $\tau$  é a escala temporal de crescimento do fluxo e  $\alpha_\gamma$  é o índice de potência do decaimento rápido. Os valores de melhor ajuste são reportados na Tabela 2.

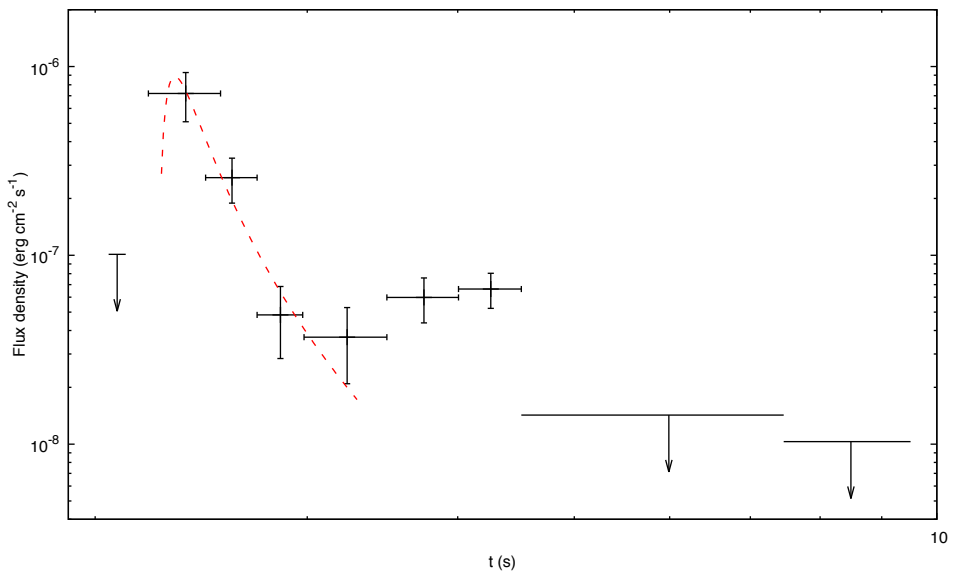


Figura 4 – Curva de Luz e limites superiores na faixa de energia  $10 - 1000$  keV do GRB170817A, dados obtidos pelo GBM. A linha vermelha corresponde ao melhor ajuste utilizando a função  $F(t) \propto \left(\frac{t-t_0}{t_0}\right)^{-\alpha} e^{-\frac{\tau}{t-t_0}}$  (Vestrand et al., 2006).

Nós derivamos os parâmetros espectrais dos dados do *Fermi-GBM* para diferentes intervalos de tempo, como mostrado na Tabela 1. Dois intervalos de tempo diferentes, começando de  $-0.320$  s, foram utilizados com a função CPL. O valor de melhor ajuste para

Tabela 2 – Valores ajustados para os dados de raios  $\gamma$ .  
A minimização Chi quadrado ( $\chi^2$  / n.g.l.) é reportada em parênteses

Fluxo de Raios $\gamma$		
Inclinação de Decaimento	$\alpha_\gamma$	$2.85 \pm 0.35$ (4.27/4)
Tempo Inicial (s)	$t_0$	$2.0 \pm 0.1$ (4.27/4)
Escala temporal de crescimento do fluxo (s)	$\tau$	$0.4 \pm 0.1$ (4.27/4)

o índice espectral no intervalo  $[-0.320 \text{ s}, 0.256 \text{ s}]$  foi  $-0.955 \pm 0.309$ . O intervalo de tempo restante foi dividido em dois e analisado com uma função PL. Para o intervalo  $[0.256 \text{ s}, 0.320 \text{ s}]$  um índice de  $-1.749 \pm 0.434$  foi encontrado e para o intervalo  $[0.320 \text{ s}, 0.448 \text{ s}]$  o índice espectral correspondente foi  $-2.150 \pm 0.472$ . Os parâmetros de ajuste espectral associados ao pico de Raios  $\gamma$  revelam uma evolução espectral do tipo duro-para-suave<sup>1</sup>.

(Veres et al., 2018) analisaram, com os dados do *Fermi-GBM*, a evolução temporal da energia do pico com um modelo CPL. Utilizando de uma PL simples com  $E_{peak} \propto (t - t_{shift})^{-q}$  para modelar a fase de decaimento, eles obtiveram um valor de melhor ajuste  $q = 0.97 \pm 0.35$  para  $t_{shift} = -0.15 \pm 0.04 \text{ s}$ .

Baseado nos valores de melhor ajuste, obtidos na análise dos dados do *Fermi-GBM* e reportados nas Tabelas 1 e 2, nós discutimos a origem da curva de luz de Raios  $\gamma$  em termos de choques internos e externos.

1. *O pico de Raios  $\gamma$  não mostra alta variabilidade,  $\delta t_{var}/T_{90} \simeq 1$ , o que desfavorece o modelo de choques internos.* — A principal motivação para evocar o modelo de choques internos está relacionado com a observação de curvas de luz de Raios  $\gamma$  variáveis. Na estrutura de colisões internas mais de um pico de Raios  $\gamma$  é esperado, com escala temporal de variabilidade muito menor do que a duração da emissão,  $\delta t_{var}/T_{90} \ll 1$  (Kobayashi; Piran; Sari, 1997; Rees; Meszaros, 1994; Burrows et al., 2005). As propriedades de diversas curvas de luz exibindo um único pico, sem variabilidade, foram satisfatoriamente explicadas através de uma estrutura de *forward/reverse shocks* e emissões de alta latitude (e.g. GRB970508, GRB021211, GRB050406) (Kumar; Panaiteescu, 2003; McMahon; Kumar; Panaiteescu, 2004; McMahon; Kumar; Piran, 2006; Nakar; Piran, 2004; Kobayashi et al., 2007; Lu; Hou; Liang, 2010; Peng et al., 2009). No caso de um *reverse shock* de curta duração, este pode gerar um pico de Raios  $\gamma$ , Raios-X ou Óptico com  $\delta t_{var}/T_{90} \simeq 1$  dependendo dos parâmetros microfísicos e a densidade do ICM (Kobayashi et al., 2007; Fraija et al., 2016). Portanto, a emissão gerada por um *reverse shock* pode, em princípio, descrever naturalmente a escala temporal de variabilidade da curva de luz de Raios  $\gamma$ .

<sup>1</sup> Análogo às cores do espectro Óptico

2. O valor do índice temporal,  $\alpha_\gamma = 2.85 \pm 0.35$ , observado durante a fase de decaimento do pico é consistente com emissão *afterglow* de altas latitudes. — A interpretação mais utilizada para levar em conta a fase de decaimento do pico nas bandas  $\gamma$ , Raios-X e Óptico é a de fótons atrasados devido efeito de curvatura. (Kumar; Panaitescu, 2000) mostraram que a evolução do fluxo observado, quando emitido em altas latitudes, é  $F_{obs} \propto t^{\beta-2}$ . Os valores do índice espectral  $\beta$  correspondem aos índices dos fótons de baixa e alta energia para o espectro SSC/Síncrotron nos regimes de resfriamento lento —  $-\frac{1}{2}$  e  $-\frac{p}{2}$  — e rápido —  $\frac{1-p}{2}$  e  $-\frac{p}{2}$ . Levando em consideração os valores típicos do índice espectral para choques externos,  $2.2 \leq p \leq 2.6$  (Kumar; Zhang, 2015), espera-se que o fluxo *afterglow* em altas latitudes evoluía como  $F_\nu \propto t^{-\alpha}$ , com  $2.5 \leq \alpha \leq 3.2$ , o que está em concordância com o valor encontrado para o índice de decaimento do pico  $\alpha_\gamma = 2.85 \pm 0.35$ . Resultados semelhantes foram encontrados em um grande grupo de GRBs quando o pico foi modelado através de emissões SSC/Síncrotron de alta latitude em *reverse shock* (O'Brien et al., 2006; Kobayashi et al., 2007; Fraija et al., 2016; Zhang; Kobayashi, 2005b; Zhang et al., 2006; Fraija et al., 2017). Por outro lado, os valores típicos do índice de decaimento do pico associado aos choques internos são  $5 \lesssim \alpha \lesssim 7$  (Zhang et al., 2006; Kumar; Zhang, 2015) que decai mais rápido do que o observado nesta erupção.
  
3. A evolução da energia do pico em centenas de keVs,  $q = 0.97 \pm 0.35$  (Veres et al., 2018), durante a fase de decaimento é consistente com a energia de quebra do *reverse shock* em emissões SSC de altas latitudes. — Múltiplos autores estudaram a evolução espectral de pulsos distintos durante a emissão imediata de Raios  $\gamma$ . Analisando a fase de decaimento do pico durante a emissão imediata algumas erupções proveram evidências de emissão síncrotron, tanto em resfriamento lento quanto rápido, em choques externos (Zhang; Kobayashi; Mészáros, 2003; Panaitescu, 2007; Fraija et al., 2017). Quando as quebras espetrais de SSC/Síncrotron são observadas vindo de altas latitudes ou fora do eixo de observação ( $\epsilon^{i,off}$  para síncrotron ou SSC), (Ioka et al., 2007) propuseram que estas quebras espetrais têm que ser reescaladas como  $\epsilon^{i,off} \propto \Gamma^{-2} \epsilon^{syn,on}$ , com  $\Gamma$  sendo o fator de Lorentz e  $\epsilon^{syn,on}$  a quebra de energia de um escoamento visto no eixo. Seguindo os passos de (Kobayashi, 2000; Fraija et al., 2016; Sari; Piran; Narayan, 1998) nós reescalamos as quantidades associadas aos choques externos e internos.
  - a) Choques internos: Dado o fator de Lorentz de grupo, o fator de Lorentz do sistema em estudo como um todo, na fase de acostamento  $\Gamma \propto t^0$  e o campo magnético no regime de congelamento  $B \propto t^0$ , a emissão síncrotron evolui como  $\epsilon_{pk}^{syn,off} \propto \Gamma^{-2} (\Gamma \gamma_e^2 B) \propto B^{-3} \Gamma^{-3} t^{-2} \propto t^{-2}$  (Derishev, 2007). Nós consideramos um fator de Lorentz típico como a média da distribuição de elétrons  $\langle \gamma_e \rangle = \frac{U_e}{m_e N_e}$  (Piran, 1999). Estas quantidades podem ser calculadas utilizando duas

maneiras diferentes: (i) A densidade de energia fornecida para acelerar os elétrons é  $U_e = \epsilon_e U = \epsilon_e \gamma_{sh} N_p m_P$  e densidade de número de elétrons pode ser estimada como  $N_e \simeq N_p$  (Piran, 1999). Neste caso, o fator de Lorentz médio dos elétrons se torna  $\langle \gamma_e \rangle = \frac{m_p}{m_e} \epsilon_e \gamma_{sh}$ . (ii) A densidade de energia fornecida para acelerar elétrons é  $U_e = \frac{m_e A_e}{(p-1)} \gamma_{e,mi}^{-p+2}$  e a densidade de número de elétrons pode ser estimada como  $N_e = \frac{m_e A_e}{(p-1)} \gamma_{e,mi}^{-p+1}$  para  $p > 2$  e  $\gamma_{e,mi} \ll \gamma_{e,ma}$ . Portanto, neste caso,  $\langle \gamma_e \rangle = \frac{p-1}{p-2} \gamma_{e,mi}$ , onde  $\gamma_{mi}$  e  $\gamma_{ma}$  são, respectivamente, os fatores de Lorentz mínimo e máximo para os elétrons e  $\gamma_{sh}$  é o fator de Lorentz relativo através do choque interno (Piran, 1999). Considerando ambos e o campo magnético dado por  $B \simeq \sqrt{\gamma_{sh}} \epsilon_B^{1/2} \Gamma^{-3} L_j^{1/2} t_\nu^{-1}$ , os elétrons acelerados e resfriados em choques internos via radiação síncrotron alcançam uma energia pico de (Fraija et al., 2017)

$$\epsilon_{pk}^{syn,on} \simeq \begin{cases} 0.4 \text{ MeV } \varepsilon_{e,-0.3}^2 \gamma_{sh}^2 & \times \left( \frac{1.01}{1+z} \right) \sqrt{\gamma_{sh}} \varepsilon_{B,-1}^{1/2} \delta t_{\nu,0}^{-1} \Gamma_3^{-2} L_{j,49}^{1/2}. \\ 0.6 \text{ MeV } \gamma_{mi,3}^2 \end{cases} \quad (3.1)$$

Os parâmetros microfísicos  $\varepsilon_e$  e  $\varepsilon_B$  são as frações de energia fornecida para acelerar elétrons e gerar ou amplificar o campo magnético, respectivamente, enquanto  $L_j$  é a luminosidade do jato. Daqui em diante a notação  $Q_x = Q/10^x$  em unidades c.g.s. é adotada. Incluindo formação de pares, o limite superior para o pico de energia ser estimado como (Guetta; Spada; Waxman, 2001)

$$\epsilon_{pk}^{syn,on} \lesssim 3.3 \text{ MeV } \left( \frac{1+z}{1.01} \right)^{-1} L_{j,49}^{-1/5} \Gamma_3^{4/3} t_{\nu,0}^{1/6} \epsilon_{B,-1}^{1/2} \epsilon_{e,-0.3}^{4/3}. \quad (3.2)$$

O pico de energia observado em altas latitudes ou em um jato fora do eixo tem que ser reescalado por  $\epsilon_{pk}^{off} \simeq b^{-1} \epsilon_{pk}^{syn,on}$  com  $b = 1 + \Gamma^2 \Delta\theta^2$  e  $\Delta\theta = \theta_{obs} - \theta_j$ . Neste caso, a energia observada  $\epsilon_{pk}^{syn,off} \simeq 10 \text{ eV } \Gamma_3^{-2} \Delta\theta_{15^\circ}^{-2}$  indica que dificilmente alcançará valores tão altos quanto centenas de keVs. Portanto, o modelo padrão de choques internos não pode explicar diretamente a evolução temporal do pico de energia em centenas de keVs.

- b) *Forward shock*: Dada a evolução do campo magnético,  $B \propto t^{-3/8}$ , o fator de Lorentz do grupo  $\Gamma \propto t^{-3/8}$ , os fatores de Lorentz mínimo e de resfriamento  $\gamma_{m,f} \propto t^{-3/8}$  e  $\gamma_{c,f} \propto t^{1/8}$  (Sari; Piran; Narayan, 1998), respectivamente, as quebras espectrais de síncrotron evoluem como  $\epsilon_{m,f}^{syn,off} \propto B \Gamma^{-3} \gamma_{m,f} \propto t^{-3/4}$  e  $\epsilon_{c,f}^{syn,off} \propto B^{-5} \Gamma^{-3} t^{-2} \propto t^{1/4}$ . As quebras espectrais de SSC, por sua vez, evoluem como  $\epsilon_{m,f}^{SSC,off} \propto \gamma_{m,f}^2 \epsilon_{m,f}^{syn,off} \propto t^{-3/2}$  e  $\epsilon_{c,f}^{SSC,off} \propto \gamma_{c,f}^2 \epsilon_{c,f}^{syn,off} \propto t^{1/2}$ . O sub-índice "f" indica o que a variável é para o *forward shock*.

A quebra espectral de síncrotron  $\epsilon_{m,f}^{syn,off}$  é a única quebra que concorda com a evolução do pico de energia. Esta quebra é dada por

$$\epsilon_{m,f}^{syn,off} \simeq 0.3 \text{ keV } \left( \frac{1+z}{1.01} \right)^{\frac{1}{2}} \varepsilon_{e,-0.3}^2 \varepsilon_{B,f,-1}^{\frac{1}{2}} E_{51}^{\frac{1}{2}} \Gamma_{2.5}^{-2} \Delta\theta_{10^\circ}^{-2} t_0^{-\frac{3}{2}}, \quad (3.3)$$

onde  $E = E_{\gamma,iso}/\eta$  é o equivalente isotrópico da energia cinética com  $\eta$  a eficiência cinética. Isto mostra que apesar da quebra espectral do síncrotron ( $\epsilon_{m,f}^{syn,off}$ ) concordar com a evolução do pico de energia, essa não pode alcançar valores de energias na ordem de centenas de keVs.

- c) *Reverse shock* no caso de casca grossa e (fina): Dada a evolução do campo magnético,  $B \propto t^{-1/4}(t^0)$ , o fator de Lorentz do grupo  $\Gamma \propto t^{-1/4}(t^0)$  e os fatores de Lorentz mínimo e de resfriamento,  $\gamma_{m,r} \propto t^{1/4}(t^3)$  e  $\gamma_{c,r} \propto t^{-1/4}(t^{-1})$  (Kobayashi, 2000), respectivamente, antes do tempo de cruzamento, as quebras espetrais de síncrotron evoluem como  $\epsilon_{m,r}^{syn,off} \propto t^{1/2}(t^6)$  e  $\epsilon_{c,r}^{syn,off} \propto t^{-1/2}(t^{-2})$ . As quebras espetrais de SSC, por sua vez, evoluem como  $\epsilon_{m,r}^{SSC,off} \propto t(t^{12})$  e  $\epsilon_{c,r}^{SSC,off} \propto t^{-1}(t^{-4})$ . Levando em conta que as quantidades após o tempo de cruzamento variam como  $B \propto t^{-13/24}(t^{-4/7})$ ,  $\Gamma \propto t^{-7/16}(t^{-2/5})$ ,  $\gamma_{m,r} \propto t^{-13/48}(t^{-2/7})$  e  $\gamma_{c,r} \propto t^{25/48}(t^{19/35})$ , as quebras espetrais de síncrotron evoluem como  $\epsilon_{m,r}^{syn,off} \propto t^{-0.65}(t^{-0.74})$  e  $\epsilon_{c,r}^{syn,off} \propto t^{-0.94}(t^{0.91})$ . E as quebras espetrais de SSC evoluem como  $\epsilon_{m,r}^{SSC,off} \propto t^{-1.18}(t^{-1.31})$  e  $\epsilon_{c,r}^{SSC,off} \propto t^{1.98}(t^{1.99})$ . Onde o subíndice "r" indica o *reverse shock*.

As quebras espetrais, tanto de SSC quanto síncrotron, são  $\epsilon_{m,r}^{syn,off} \propto t^{-0.65}(t^{-0.74})$  e  $\epsilon_{m,r}^{SSC,off} \propto t^{-1.18}(t^{-1.31})$ , respectivamente. De acordo com (Kobayashi et al., 2007; Fraija et al., 2017) as quebras espetrais para síncrotron e SSC são dados por

$$\epsilon_{m,r}^{syn,on} \simeq 16.2 \text{ eV} \left( \frac{1+z}{1.01} \right)^{-1} \varepsilon_{e,-0.3}^2 \varepsilon_{B,r,-1}^{\frac{1}{2}} \Gamma_{2.8}^2 n_0^{\frac{1}{2}}, \quad (3.4)$$

$$\epsilon_{m,r}^{ssc,on} \simeq 13.4 \text{ MeV} \left( \frac{1+z}{1.01} \right)^{-\frac{7}{4}} \varepsilon_{e,-0.3}^4 \varepsilon_{B,r,-1}^{\frac{1}{2}} \Gamma_{2.8}^4 n_0^{\frac{3}{4}} E_{51}^{-\frac{1}{4}} t_{cr,0}^{\frac{3}{4}}, \quad (3.5)$$

que necessita ser reescalado por  $(1 + \Gamma^2 \Delta \theta^2)^{-1}$  (Ioka; Nakamura, 2017). O termo  $t_{cr}$  é o tempo de cruzamento do choque. O parâmetro  $n$ , por sua vez, corresponde à densidade do ICM. Para essa análise, o fator de Lorentz de grupo corresponde ao associado com o *reverse shock*. Este valor pode ser estimado levando em consideração a estrutura de quatro regiões ao redor do choque: (i) O ISM, onde não houve choque, com densidade  $n_1$ ; (ii) O ISM onde houve choque; (3) o material chocado da casca e (4) o material da casca onde não houve choque, com densidade  $n_4$ , e as equações governando os choques com as condições de pulo  $\frac{n_4}{n_1} \simeq \frac{(\gamma_3 - 1)(4\gamma_3 + 3)}{(\gamma_{34} - 1)(4\gamma_{34} + 3)}$  e  $\gamma_{34} \simeq \frac{1}{2} \left( \frac{\gamma_4}{\gamma_3} + \frac{\gamma_3}{\gamma_4} \right)$  (Blandford; McKee, 1976; Sari; Piran, 1995), com  $\gamma_{34}$  o fator de Lorentz relativo entre as regiões no sentido de propagação de fluxo e no sentido contrário,  $\gamma_3 = \Gamma_r$  e  $\gamma_4 = \Gamma$  os fatores de Lorentz do *reverse shock* e inicial, respectivamente (Kobayashi et al., 2007). Para o caso relativístico, i.e.  $\gamma_{34} \gg 1$ , o fator de Lorentz de grupo do *reverse*

*shock* é

$$\Gamma_r \simeq \sqrt{\frac{\Gamma}{2}} \left( \frac{n_4}{n_1} \right)^{1/4}. \quad (3.6)$$

Para valores típicos do fator de Lorentz de grupo inicial  $300 \leq \Gamma \leq 600$  e densidades do ISM onde não houve choque se torna  $12.3 \leq \Gamma_r \leq 17.3$ . Para o caso de  $\Gamma_r = 15$ , as quebras espectrais de síncrotron e SSC tem que ser reescaladas por  $\sim 7^{-2} \Gamma_{r,1.2}^{-2} \Delta\theta_{15^\circ}^{-2}$ . Portanto, a quebra característica da emissão SSC do *reverse shock* concorda com a evolução do pico de energia em centenas de keVs durante a fase de decaimento.

- d) *A evolução do índice espectral de duro para suave (de  $-1.749 \pm 0.434$  para  $-2.150 \pm 0.472$ ) aparenta ser consistente com um espectro SSC/síncrotron originado em choques externos.* — Elétrons ultra relativísticos confinados em um campo magnético são resfriados por radiação síncrotron e SSC. Os índices espectrais altos e baixos nos regimes de resfriamento rápido(lento) são  $-\frac{1}{2}(-\frac{p-1}{2})$  e  $-\frac{p}{2}(-\frac{p}{2})$ , respectivamente. Dado os valores típicos do índice de potência espectral para choques externos,  $2.2 \leq p \leq 2.6$  ([Kumar; Panaiteescu, 2003](#)), o espectro SSC/síncrotron  $\nu F_\nu \propto \nu^{-(\beta+1)}$ , com  $1.5(1.6) \leq \beta + 1 \leq 2.3(2.3)$ , concorda com a evolução do índice espectral para os regimes de resfriamento rápido(lento).

A análise anterior, realizada nas características temporais e espectrais da curva de luz de Raios  $\gamma$ , ([Figura 4](#), [Tabelas 1 e 2](#)) ilustra que: (i) A quebra característica de SSC do *reverse shock* concorda com a evolução do pico de energia em centenas de keVs durante a fase de decaimento, enquanto a emissão síncrotron do choque interno e *forward shock* não explica essa evolução; (ii) A emissão de *reverse shock* pode reproduzir, de maneira mais natural, a escala de variabilidade temporal observada melhor do que uma emissão de choques internos e (iii) Os índices espectrais e temporais da emissão SSC/síncrotron, originadas em choques externos, são consistentes com a evolução do índice espectral e o modelo de *afterglow* de alta latitude. Portanto nós argumentamos que a emissão SSC em *reverse shock*, no regime de resfriamento rápido, pode reproduzir as características temporais e espectrais da curva de luz de Raios  $\gamma$ . Nas próximas subsecções o espectro SSC em regime de resfriamento rápido é utilizado para descrever o fluxo de raios  $\gamma$ .

### 3.1.2 Modelo Teórico

As quebras espectrais e fluxos SSC são determinadas pela evolução da quebra espectral entre o *forward shock* e *reverse shock* ([Zhang; Kobayashi, 2005b; Fraija, 2015; Fraija et al., 2016](#)). O espectro SSC no regime de resfriamento rápido é dado por ([Ioka;](#)

Nakamura, 2017)

$$F_{\nu,r}^{SSC,on} = F_{max,r}^{SSC,on} \left( \frac{\epsilon_\gamma}{\epsilon_{c,r}^{SSC,on}} \right)^{-\frac{1}{2}} \quad \text{para } \epsilon_{c,r}^{SSC,on} < \epsilon_\gamma < \epsilon_{m,r}^{SSC,on} \quad (3.7)$$

e uma vez que a energia de quebra característica atravessa a banda de Raios  $\gamma$ ,  $\epsilon_\gamma \approx 100 \text{ keV}$  em aproximadamente  $t_c r \epsilon_{m,r}^{SSC,on} / \epsilon_\gamma$ , o fluxo SSC começa a evoluir seguindo a lei de potência da curva de luz,  $F_{max,r}^{SSC,on} \left( \frac{\epsilon_{m,r}^{SSC,on}}{\epsilon_{c,r}^{SSC,on}} \right)^{-\frac{1}{2}} \left( \frac{\epsilon_\gamma}{\epsilon_{m,r}^{SSC,on}} \right)^{-\frac{p}{2}}$ , para  $\epsilon_{c,r}^{SSC,on} < \epsilon_{m,r}^{SSC,on} < \epsilon_\gamma$ . As quebras de energia e fluxo máximo, para SSC, quando o *reverse shock* evolui em uma casca grossa são dadas explicitamente em (Fraija; González; Lee, 2012b). Essas quantidades quando vistas fora do eixo precisam ser corrigidas por

$$\epsilon_{c,r}^{SSC,off} = b^{-1} \epsilon_{c,r}^{SSC,on} \quad \epsilon_{m,r}^{SSC,off} = b^{-1} \epsilon_{m,r}^{SSC,on} \quad F_{max,r}^{SSC,off} = b^{-3} F_{max,r}^{SSC,on} \quad (3.8)$$

onde  $b = 1 + \Gamma^2 \Delta \theta^2$ .

## 3.2 Modelando os Fluxos de Raios-X, Óptico e Rádio

### 3.2.1 Análise e Descrição da Curva de Luz

Múltiplas observações em Raios-X foram realizadas durante os primeiros 8 dias após a fusão, fornecendo os limites (Margutti et al., 2017). No nono dia, o observatório *Chandra* reportou um fluxo de Raios-X fraco vindo da direção do sistema binário (Troja et al., 2017). Do 108th até o 256th dia após a centelha inicial do GW/GRB, os observatórios *Chandra* e *XMM-Newton* relataram várias detecções (Margutti et al., 2017; Haggard; Nynka; Ruan, 2018). O *Hubble Space Telescope* (HST) observou fluxos Ópticos não-térmicos com magnitudes  $26.44 \pm 0.14$  mag (Lyman et al., 2018) e  $26.90 \pm 0.14$  mag (Margutti et al., 2018) em  $\sim 100$  e  $137$  dias, respectivamente, após a fusão. Em 23 de Março de 2018, HST forneceu um limite superior de  $> 0.070 \mu\text{Jy}$  (Alexander et al., 2018). Desde o 16th dia após a fase imediata, e por mais de 6 meses, o *Very Large Array* (VLA) reportou um fraco fluxo de Rádio em 3 e 6 GHz (Troja et al., 2017; Hallinan et al., 2017; Alexander et al., 2018). Para descrever, primeiramente, as curvas de luz de Raios-X, Óptico e Rádio durante a fase de crescimento, nós consideramos essas curvas de luz até  $140 \pm 20$  dias e a Distribuição Energética Espectral (do inglês *Spectral Energy Distribution*, SED) em três períodos distintos: em  $15 \pm 2$ ,  $110 \pm 5$ ,  $145 \pm 20$  dias. As curvas de luz de Raios-X e Rádio (6 e 3 GHz) do período de  $145 \pm 20$  dias foram ajustados com leis de potência simples  $F_v \propto \nu^{-\beta_t}$ . Os valores de melhor ajuste dos índices espectrais e temporais obtidos com o teste  $\chi^2$  implementado no pacote de software ROOT são reportados na Tabela 3. Dado os valores de melhor ajuste obtidos para o período  $145 \pm 20$  dias, os fluxos de múltiplos comprimentos de onda podem ser descritos como  $\propto t^{0.76 \pm 0.18} \nu^{-0.58 \pm 0.15}$  para os dados de Raios-X, Óptico e Rádio.

Tabela 3 – Valores ajustados para os dados de Raios-X, Óptico e Rádio.  
As minimizações Chi-Quadrado ( $\chi^2$  / n.d.f.) são reportadas entre parênteses

<b>Curva de Luz</b>		
<b>Fluxo Raios-X</b>		
Inclinação Crescente	$\alpha_X$	$0.76 \pm 0.12$ (0.45/4)
<b>Fluxo Óptico</b>		
Inclinação Crescente	$\alpha_{opt}$	—
<b>Fluxo Rádio</b>		
3 GHz		
Inclinação Crescente	$\alpha_{3GHz}$	$0.85 \pm 0.12$ (1.67 / 3)
6 GHz		
Inclinação Crescente	$\alpha_{6GHz}$	$0.75 \pm 0.15$ (11.16 / 6)
<b>Distribuição de Energia Espectral</b>		
Inclinação Espectral(16 ± 2 d)	$\beta_{16d}$	$-0.59 \pm 0.06$ (3.796 / 7)
Inclinação Espectral (110 ± 5 d)	$\beta_{110d}$	$-0.58 \pm 0.15$ (19.19 / 20)
Inclinação Espectral (145 ± 20 d)	$\beta_{145d}$	$-0.59 \pm 0.15$ (19.19 / 20)

Emissão *afterglow* é gerada quando o jato relativístico encontra o meio homogêneo e carrega suficiente material do ICM. O modelo de síncrotron em *forward shock* é o mais favorável para descrever as observações em múltiplos comprimentos de ondas existentes em tempos tardios. Levando em conta as relações de fechamento do modelo padrão para síncrotron em *forward shock*, os fluxos de Raios-X, Óptico e Rádio (6 e 3 GHz) estão evoluindo no regime de resfriamento lento correspondente ao segmento da lei de potência (Sari; Piran; Narayan, 1998)

$$F_{\nu,f}^{syn,on} = F_{max,f}^{syn,on} \left( \frac{\epsilon_\gamma}{\epsilon_{m,f}^{syn,on}} \right)^{-\frac{p-1}{2}} \quad \text{para } \epsilon_{m,f}^{syn,on} < \epsilon_\gamma < \epsilon_{c,f}^{syn,on} \quad (3.9)$$

com  $p = 2\beta + 1 \approx 2.2$  e

$$\epsilon_{m,f}^{syn,on} \propto t^0 \Gamma^4, \quad \epsilon_{c,f}^{syn,on} \propto t^{-2} \Gamma^{-4} \quad \text{e} \quad F_{max,f}^{syn,on} \propto E t^0 \Gamma^0. \quad (3.10)$$

Considerando a evolução do fator de Lorentz de grupo,  $\Gamma \propto t^{-\frac{3}{8}}$ , o fluxo varia como  $F_{\nu,f}^{syn,on} \propto t^{-\frac{3(p-1)}{4}}$ . Dado o índice temporal observado e reportado na Tabela 3, o valor da distribuição de elétrons seria  $p \approx -0.07$  que é inconsistente com o valor obtido do SED de banda larga ( $p \approx 2.2$ ). Enquanto a evolução do fluxo de síncrotron como função da energia é bem descrito, a evolução temporal não é. Esta inconsistência ocorre devido a evolução do fator de Lorentz de grupo.

Considerando que o modelo padrão de *afterglow* síncrotron não pode explicar as curvas de luz para Raios-X, Óptico e Rádio do GRB170817A, nós consideramos o modelo de síncrotron em *forward shock* ser fora do eixo quando a matéria no escoamento é parametrizada através de uma distribuição de velocidades de lei de potências.

### 3.2.2 Modelo Teórico

Nós consideramos que o jato, concentrado dentro de um ângulo de abertura  $\theta_j$  (jato "top-hat"), produzindo a emissão *afterglow* não está alinhado com a linha de visão do observador e o material ejetado possui uma energia cinética equivalente parametrizada por uma distribuição lei de potências,  $\tilde{E}(\beta\Gamma)^{-\alpha_s}$  onde  $\tilde{E}$  é a energia fiducial,  $\alpha_s = 1.1$  para  $\beta\Gamma \gg 1$  e  $\alpha_s = 5.2$  para  $\beta\Gamma \ll 1$  para o caso adiabático (Tan; Matzner; McKee, 2001; Sari; Mészáros, 2000; Barniol Duran et al., 2015; Hotokezaka; Piran, 2015a; Hotokezaka et al., 2013; Hotokezaka; Piran, 2015b; Kyutoku; Ioka; Shibata, 2014; Fraija; Pedreira; Veres, 2018). Levando em consideração o regime relativístico ( $\beta\Gamma \gg 1$ ), nós propomos que a energia cinética equivalente para  $\theta_{obs} \gtrsim 2\theta_j$  é dada por

$$E_k = b^{-3}\tilde{E}\Gamma^{-\alpha_s} \quad (3.11)$$

$$\simeq \Delta\theta^{-6}\Gamma^{-\delta}\tilde{E}, \quad (3.12)$$

para  $\Gamma^2\Delta\theta^2 \gg 1$ , com  $\Delta\Theta = \theta_{obs} - \theta_j$  e  $\delta = \alpha_s + 6$ .

Considerando a evolução adiabática de um *forward shock*, a energia fiducial é dada por  $\tilde{E} = 16/17\pi\Delta\theta^6\Gamma^{\delta+2}R^3nm_p$  (Blandford; McKee, 1976), com  $m_p$  a massa do próton e  $R$  o raio de desaceleração, onde o jato relativístico tipicamente começa a desacelerar. Nesse caso o fator de Lorentz de grupo evolui como

$$\Gamma = 7.8 \left( \frac{1+z}{1.01} \right)^{\frac{3}{\delta+8}} n_{-4}^{-\frac{1}{\delta+8}} \tilde{E}_{51}^{\frac{1}{\delta+8}} \Delta\theta_{20^\circ}^{-\frac{6}{\delta+8}} t_{1d}^{-\frac{3}{\delta+8}}. \quad (3.13)$$

Substituindo as equações 3.13 e 3.11 em 3.10, as quebras espectrais de síncrotron e fluxo máximo são

$$\begin{aligned} \epsilon_{m,f}^{syn} &\simeq 7.7 \times 10^{-4} \text{ GHz} \left( \frac{1+z}{1.01} \right)^{\frac{4-\delta}{\delta+8}} \varepsilon_{e,-1}^2 \varepsilon_{B,-4}^{\frac{1}{2}} n_{-4}^{\frac{\delta}{2(\delta+8)}} \tilde{E}_{51}^{\frac{4}{\delta+8}} \Delta\theta_{20^\circ}^{-\frac{24}{\delta+8}} t_{100d}^{\frac{12}{\delta+8}} \\ \epsilon_{c,f}^{syn} &\simeq 5.2 \text{ keV} \left( \frac{1+z}{1.01} \right)^{\frac{\delta-4}{\delta+8}} (1+x)^{-2} \varepsilon_{B,-4}^{-\frac{3}{2}} n_{-4}^{\frac{-16+3\delta}{2(\delta+8)}} \tilde{E}_{51}^{-\frac{4}{\delta+8}} \Delta\theta_{20^\circ}^{\frac{24}{\delta+8}} t_{100d}^{-\frac{2\delta+4}{\delta+8}} \\ F_{max,f}^{syn} &\simeq 1.4 \text{ mJy} \left( \frac{1+z}{1.01} \right)^{\frac{8-2\delta}{\delta+8}} \varepsilon_{B,-4}^{\frac{1}{2}} n_{-4}^{\frac{3\delta+8}{2(\delta+8)}} D_{26.1}^{-2} \tilde{E}_{51}^{\frac{8}{\delta+8}} \Delta\theta_{20^\circ}^{-\frac{48}{\delta+8}} t_{100d}^{\frac{3\delta}{\delta+8}}. \end{aligned} \quad (3.14)$$

Dada a nova evolução da emissão síncrotron, pelas equações 3.17 e 3.9, o segmento da lei de potência do espectro de síncrotron em regime de resfriamento lento se torna

$$F_{\nu,inc} \simeq F_{\nu,i} t_{100d}^{\frac{3\delta-6(p-1)}{\delta+8}} \epsilon_{\gamma}^{-\frac{p-1}{2}} A_{\nu,inc}, \quad (3.15)$$

onde

$$A_{\nu,inc} = \left( \frac{1+z}{1.01} \right)^{-\frac{7\delta+12+p\delta+4p}{2(\delta+8)}} \varepsilon_{e,-1}^{p-1} \varepsilon_{B,-4}^{\frac{p+1}{4}} n_{-4}^{\frac{16+\delta(p+5)}{4(\delta+8)}} D_{26.1}^{-2} \tilde{E}_{51}^{\frac{6+2p}{\delta+8}} \Delta\theta_{20^\circ}^{-\frac{12(p+3)}{\delta+8}}, \quad (3.16)$$

e  $F_{\nu,i} = \{9.8 \times 10^{-3}, 6.5 \times 10^{-3}, 1.1 \times 10^{-5}, 1.8 \times 10^{-7}\}$  mJy para  $\epsilon_\gamma = \{3 \text{ GHz}, 6 \text{ GHz}, 1 \text{ eV}, 1 \text{ keV}\}$ , respectivamente. Para esse caso o fluxo varia como  $F_\nu \propto t^{\frac{3\delta-6(p-1)}{\delta+8}} \nu^{-\frac{p-1}{2}}$ , para qual usando  $\alpha_s \approx 1.1$  e  $p \approx 2.2$  o fluxo evolui como encontrado após ajuste do SED, em  $15 \pm 2$ ,  $110 \pm 5$  e  $145 \pm 20$  dias, como reportado na Tabela 3. Vale a pena notar que para  $\delta = 0$ , o fluxo  $F_{\nu,dec} \propto t^{-\frac{3(p-1)}{4}}$  derivado em (Sari; Piran; Narayan, 1998) é recuperado.

Como o feixe conoidal de radiação amplia cada vez mais, eventualmente chegará em nossa linha de visão ( $\Gamma \sim \Delta\theta^{-1}$ ) (Rees, 1999; Sari; Piran; Halpern, 1999). Uma vez que o fluxo alcança nosso campo de visão, as quebras espectrais e fluxo máximo de sincrotron se tornam

$$\begin{aligned} \epsilon_{m,f}^{syn} &\simeq 2.9 \times 10^{-4} \text{ GHz} \left( \frac{1+z}{1.01} \right)^{\frac{6-\alpha_s}{\alpha_s+6}} \varepsilon_{e,-1}^2 \varepsilon_{B,-4}^{\frac{1}{2}} n_{-4}^{\frac{\alpha_s-2}{2(\alpha_s+6)}} \tilde{E}_{51}^{\frac{4}{\alpha_s+6}} t_{200d}^{-\frac{12}{\alpha_s+6}} \\ \epsilon_{c,f}^{syn} &\simeq 3.4 \text{ keV} \left( \frac{1+z}{1.01} \right)^{\frac{\alpha_s-6}{\alpha_s+6}} (1+x)^{-2} \varepsilon_{B,-4}^{-\frac{3}{2}} n_{-4}^{\frac{3\alpha_s+10}{2(\alpha_s+6)}} \tilde{E}_{51}^{-\frac{4}{\alpha_s+6}} t_{200d}^{-\frac{2\alpha_s}{\alpha_s+6}} \\ F_{max,f}^{syn} &\simeq 1.1 \text{ mJy} \left( \frac{1+z}{1.01} \right)^{-\frac{4\alpha_s}{\alpha_s+6}} \varepsilon_{B,-4}^{\frac{1}{2}} n_{-4}^{\frac{3\alpha_s+2}{2(\alpha_s+6)}} D_{26.1}^{-2} \tilde{E}_{51}^{\frac{8}{\alpha_s+6}} t_{200d}^{\frac{3(2-\alpha_s)}{\alpha_s+6}}. \end{aligned} \quad (3.17)$$

Como  $\epsilon_{m,f}^{syn} \leq \epsilon_\gamma \leq \epsilon_{c,f}^{syn}$ , o fluxo se encontra no mesmo segmento da lei de potências. Esse começa a decrescer de maneira

$$F_{\nu,dec} \simeq F_{\nu,j} t_{200d}^{-\frac{3(\alpha_s-2p)}{\alpha_s+6}} \epsilon_\gamma^{-\frac{p-1}{2}} A_{\nu,dec}, \quad (3.18)$$

onde

$$A_{\nu,dec} = \left( \frac{1+z}{1.01} \right)^{\frac{6p-7\alpha_s-p\alpha_s-6}{2(\delta+8)}} \varepsilon_{e,-1}^{p-1} \varepsilon_{B,-4}^{\frac{p+1}{4}} n_{-4}^{\frac{5\alpha_s+6+\alpha_sp-2p}{4(\alpha_s+6)}} \tilde{E}_{51}^{\frac{2(p+3)}{\alpha_s+6}} \quad (3.19)$$

e  $F_{\nu,j} = \{6.1 \times 10^{-3}, 4.0 \times 10^{-3}, 6.9 \times 10^{-6}, 1.1 \times 10^{-7}\}$  mJy para  $\epsilon_\gamma = \{3 \text{ GHz}, 6 \text{ GHz}, 1 \text{ eV}, 1 \text{ keV}\}$ , respectivamente. Novamente, vale a pena notar que para  $\alpha_s = 0$ , o fluxo  $F_{\nu,dec} \propto t^{-p}$  encontrado por (Sari; Piran; Halpern, 1999) é recuperado.

Portanto, o fluxo usado para modelar os dados de Raios-X, Óptico e Rádio pode ser resumido como

$$F_\nu = \begin{cases} F_{\nu,inc}, & \text{se } t < t_{pico} \\ F_{\nu,dec}, & \text{se } t > t_{pico} \end{cases} \quad (3.20)$$

onde

$$t_{pico} \simeq 86.6 \text{ dias} k \frac{1+z}{0.01} n_0^{-\frac{1}{3}} E_5^{\frac{1}{3}} \Delta\theta^{-\frac{\alpha_s+6}{3}} \quad (3.21)$$

e o parâmetro  $k$  varia de um modelo para outro. Este parâmetro é introduzido para correlacionar os tempos de pico de fluxo e *jet break* através dos ângulos de visualização e abertura (Nakar; Piran, 2011). Os ajustes são demonstrados na Figura 5, na página a seguir.

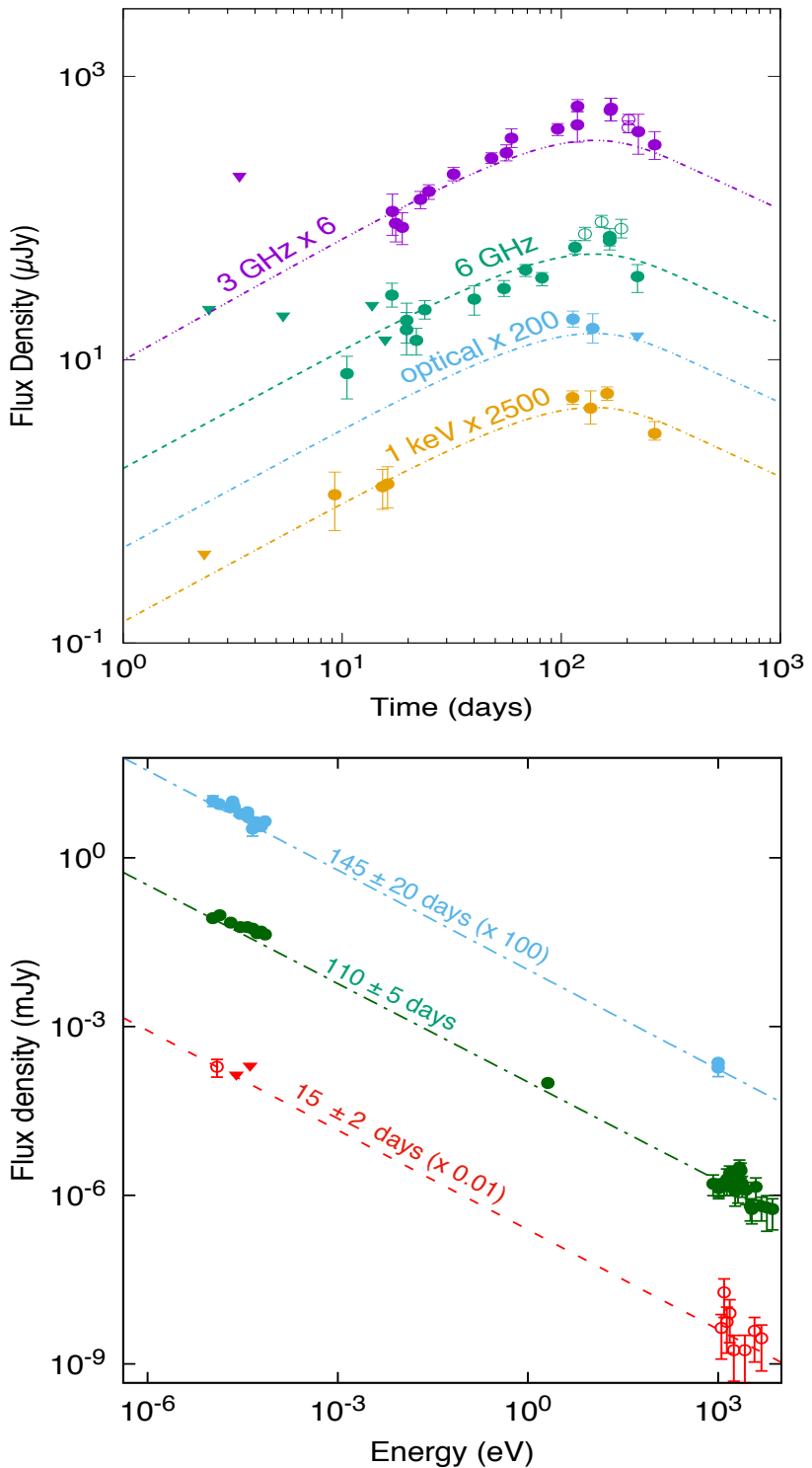


Figura 5 – Acima: SEDs das observações *afterglow* de Raios-X, Óptico e Rádio às  $15 \pm 2$  (vermelho),  $110 \pm 5$  (verde) e  $145 \pm 20$  (azul) dias. Abaixo: Curvas de luz de Raios-X à 1 keV (dourado) (Troja et al., 2017; Margutti et al., 2018; Haggard; Nynka; Ruan, 2018; Margutti et al., 2017), Óptico (azul) (Margutti et al., 2018) e Rádio nas bandas 3 e 6 GHz (magenta) (Troja et al., 2017; Hallinan et al., 2017; Alexander et al., 2018). Os valores que descrevem tanto o SED quanto as curvas de luz são reportados na Tabela 3.

### 3.3 Cadeias de Markov em Monte Carlo (MCMC)

Para nosso trabalho, os nossos modelos são descritos por grupos de parâmetros. No caso da emissão SSC em *reverse shock*, nosso modelo é descrito completamente por um grupo de sete parâmetros,  $\zeta = \{n, \tilde{E}, \Delta\theta, p, \Gamma_r, \varepsilon_{B,r}, \varepsilon_e\}$ , com um parâmetro extra  $\sigma$  que serve como desvio padrão para a distribuição que descreve nossa probabilidade. Nós geramos as amostras das distribuições posteriores para nosso modelo fora do eixo através do *No-U-Turn Sampler* (NUTS) da distribuição PyMC3 ([Salvatier, 2016](#)). Para ajustar os dados nós rodamos o modelo para os fluxos com um total de 14000 amostras e 3000 passos de refinamento, que são descartados após refinamento. As priores são atribuídas independentemente, com uma mistura de distribuições contínuas de probabilidade e desvio padrão diferentes. Para os parâmetros  $p$ ,  $\Gamma_r$  e  $n$  nós utilizamos distribuições normais,  $\varepsilon_{B,r}$ ,  $\varepsilon_e$  e  $\tilde{E}$  são dadas distribuições normais modificadas e  $\Delta\theta$  uma distribuição uniforme. As distribuições posteriores são apresentadas por meio de um *Cornerplot* ([Foreman-Mackey, 2016](#)), em que a diagonal é um gráfico unidimensional da distribuição de probabilidade posterior e os gráficos fora da diagonal são a representação da densidade bidimensional. Os parâmetros cosmológicos utilizados foram  $H_0 = 71 \text{ kms}^{-1}\text{Mpc}^{-1}$ ,  $\Omega_m = 0.27$  e  $\Omega_\lambda = 0.73$ .

Figura 6 mostra o *cornerplot* obtido através da simulação MCMC para cada parâmetro utilizando nosso modelo de SSC *reverse shock*. Os valores de melhor ajuste são representados pela linha sólida. A mediana das distribuições posteriores, juntamente com os *quantiles* simétricos de 35% são reportados na Tabela 4.

Tabela 4 – A mediana e *quantiles* simétricos (0.15, 0.5, 0.85) como encontrados após descrever o pico de Raios  $\gamma$  do GBM com nosso modelo.

Parâmetros	Mediana
$\tilde{E} (10^{51} \text{ erg})$	$0.83^{+1.19}_{-0.54}$
$n (\text{cm}^{-3})$	$1.01^{+0.29}_{-0.29}$
$\Gamma_r$	$24.94^{+4.93}_{-4.84}$
$p$	$2.20^{+0.06}_{-0.06}$
$\Delta\theta (\text{ deg})$	$15.01^{+0.68}_{-0.68}$
$\varepsilon_e (10^{-1})$	$3.17^{+0.83}_{-1.16}$
$\varepsilon_{B,r} (10^{-1})$	$1.80^{+1.15}_{-0.78}$

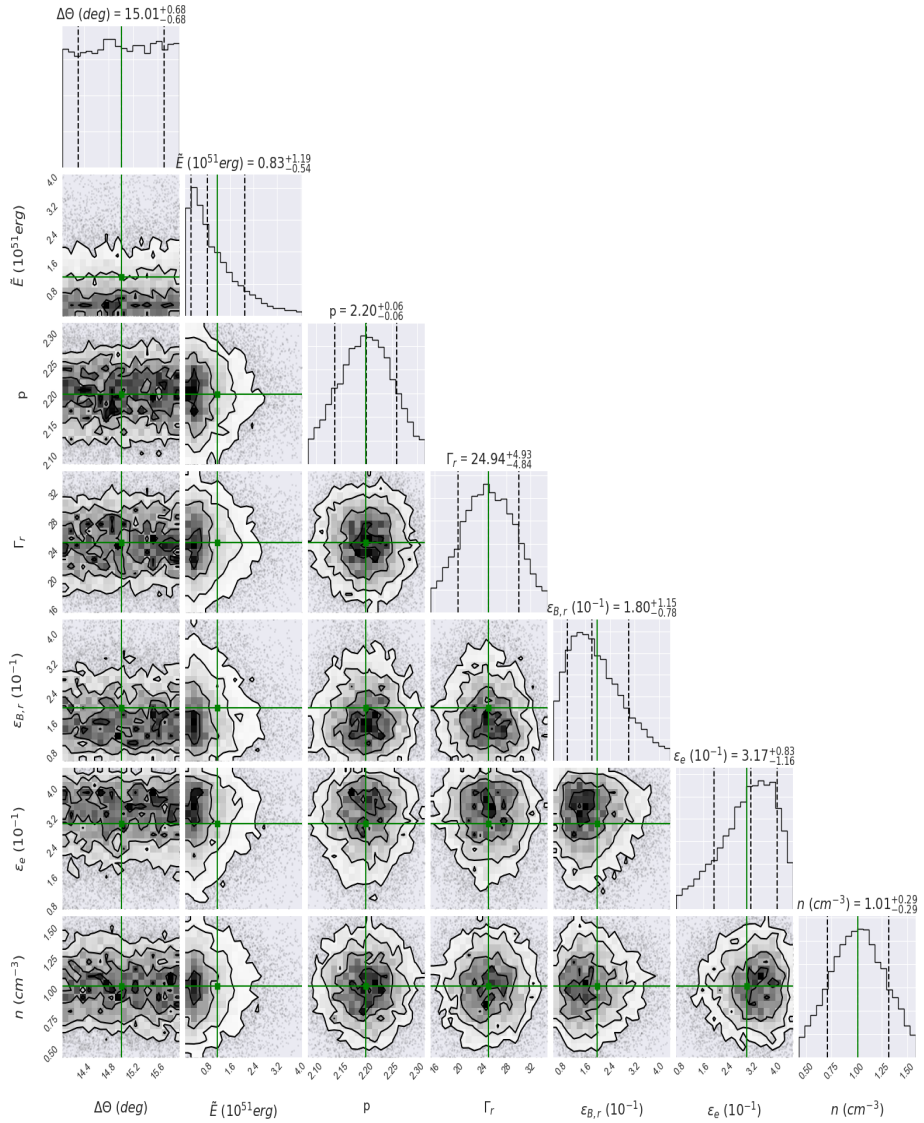


Figura 6 – Cornerplot apresentando os resultados obtidos nas simulações MCMC para cada parâmetro. Resultado do ajuste para os dados de Raios  $\gamma$  do GBM utilizando um modelo de SSC em *reverse shock* para uma densidade homogênea como descrito em 3.1. A legenda acima de cada gráfico indica a mediana, 0.15 e 0.85 *quantiles* de cada parâmetro. O valor de melhor ajuste é mostrado em cor verde.

Similarmente, nosso modelo de síncrotron em *forward shock* é descrito por um grupo de oito parâmetros,  $\zeta = \{n, \tilde{E}, k, \Delta\theta, p, \alpha_s, \varepsilon_{B,f}, \varepsilon_e\}$ , com o parâmetro extra  $\sigma$  representando o desvio padrão da probabilidade no MCMC. Para essa simulação, também utilizamos de 14000 passos, com 7000 passos de refinamento, descartados após refinamento. Aos parâmetros  $\Delta\theta$  e  $p$  foram atribuídos distribuições uniformes enquanto os parâmetros restantes,  $n, \tilde{E}, k, \alpha_s, \varepsilon_{B,f}$  e  $\varepsilon_e$  receberam distribuições normais. As distribuições posteriores são novamente representadas por um *cornerplot* em que a diagonal é um gráfico unidimensional da distribuição de probabilidade posterior e os gráficos fora da diagonal são a representação da densidade bidimensional.

Figuras 7, 8 e 9 mostram os *cornerplots* para rádio (3 GHz e 6 GHz) e Raios-X, respectivamente, obtidos através da simulação de MCMC com nosso modelo (eq 3.20). Os valores de melhor ajuste são representados pela linha sólida na imagem. A mediana das distribuições posteriores, juntamente com os *quantiles* simétricos de 35% são apresentados na Tabela 5.

Tabela 5 – A mediana e *quantiles* simétricos (0.15, 0.5, 0.85), truncados na segunda casa decimal, como encontrados após descrever os Raios-X e Rádio em 3 e 6 GHz com nosso modelo.

Parâmetros	Mediana		
	Rádio (3 GHz)	Rádio (6 GHz)	Raios-X (1 keV)
$\tilde{E}$ ( $10^{51}$ erg)	$0.98^{+0.07}_{-0.08}$	$0.98^{+0.05}_{-0.05}$	$0.97^{+0.05}_{-0.05}$
$n$ ( $10^{-4}$ cm $^{-3}$ )	$0.95^{+0.07}_{-0.07}$	$0.99^{+0.05}_{-0.05}$	$0.96^{+0.05}_{-0.05}$
$p$	$2.20^{+0.00}_{-0.00}$	$2.20^{+0.01}_{-0.01}$	$2.19^{+0.01}_{-0.01}$
$\Delta\theta$ ( deg)	$15.01^{+0.01}_{-0.01}$	$15.04^{+0.04}_{-0.09}$	$15.07^{+0.09}_{-0.15}$
$\varepsilon_e$ ( $10^{-1}$ )	$3.05^{+0.05}_{-0.05}$	$2.96^{+0.05}_{-0.05}$	$2.99^{+0.05}_{-0.05}$
$\varepsilon_{B,f}$ ( $10^{-4}$ )	$2.40^{+0.05}_{-0.05}$	$2.37^{+0.05}_{-0.05}$	$2.39^{+0.05}_{-0.05}$
$k$	$3.04^{+0.05}_{-0.05}$	$3.03^{+0.05}_{-0.05}$	$3.01^{+0.05}_{-0.05}$
$\alpha_s$	$2.42^{+0.02}_{-0.02}$	$2.44^{+0.06}_{-0.06}$	$2.35^{+0.06}_{-0.06}$

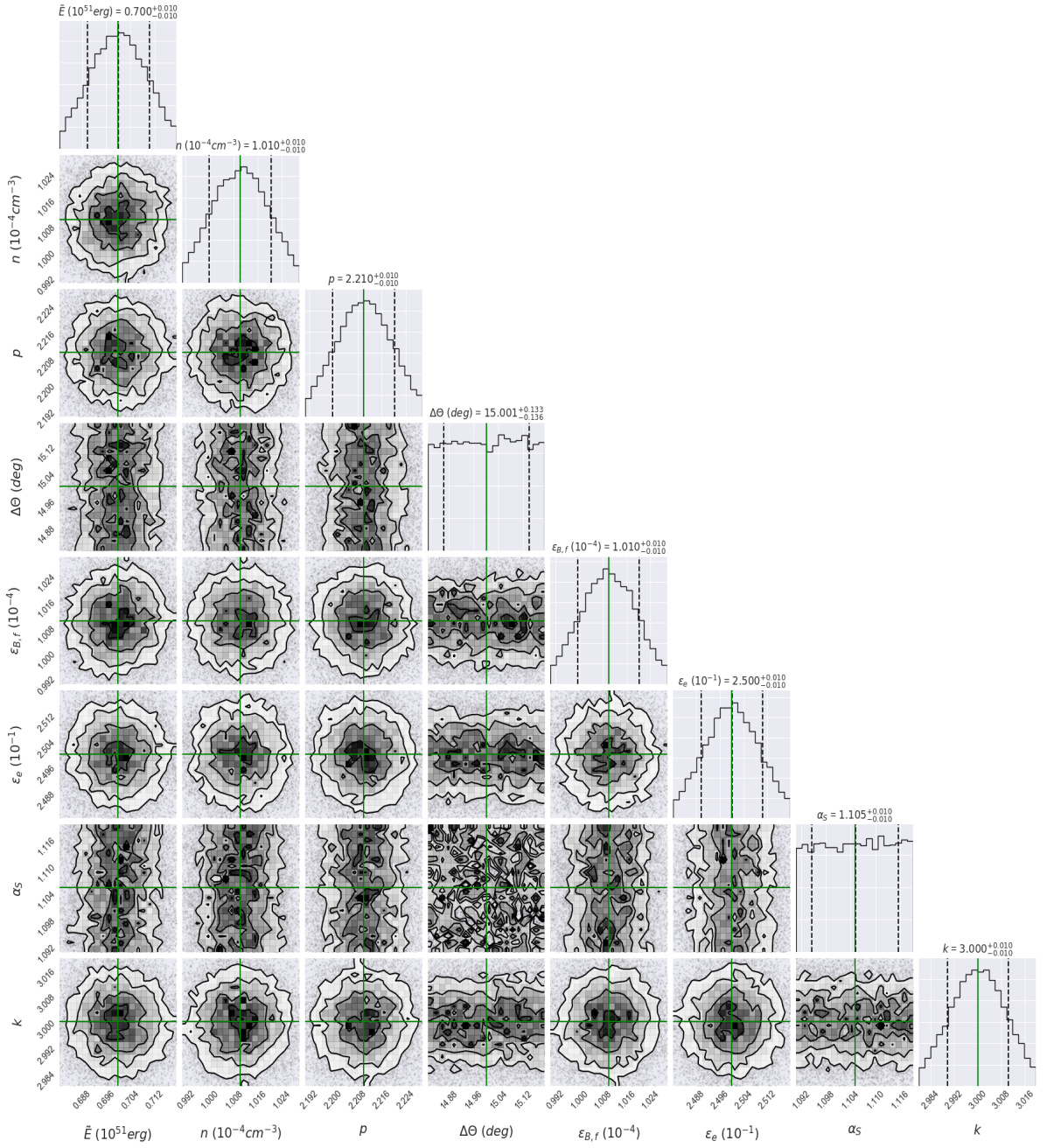


Figura 7 – Idem à Fig. 6, mas usando um modelo de síncrotron em *forward shock* para ajustar os dados de Rádio (3 GHz) quando o jato produzindo a emissão *afterglow* não está alinhado com a linha de visão do observador e a matéria no escoamento é parametrizada através de uma distribuição de velocidades de lei de potências. Modelo descrito em 3.2.

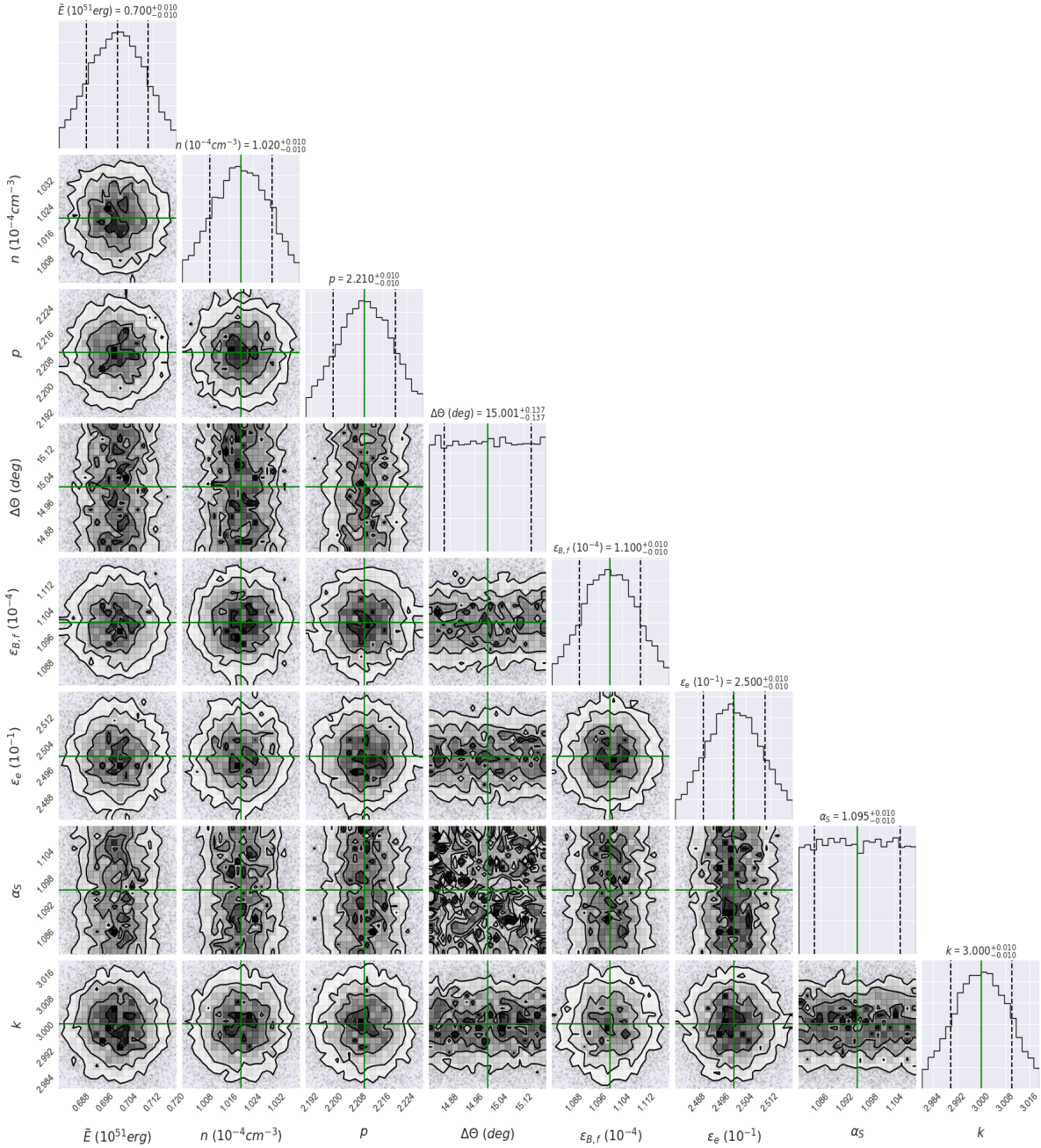


Figura 8 – Idem à Fig. 7, mas usando um modelo de síncrotron em *forward shock* para ajustar os dados de Rádio (6 GHz) quando o jato produzindo a emissão *afterglow* não está alinhado com a linha de visão do observador e a matéria no escoamento é parametrizada através de uma distribuição de velocidades de lei de potências. Modelo descrito em 3.2.

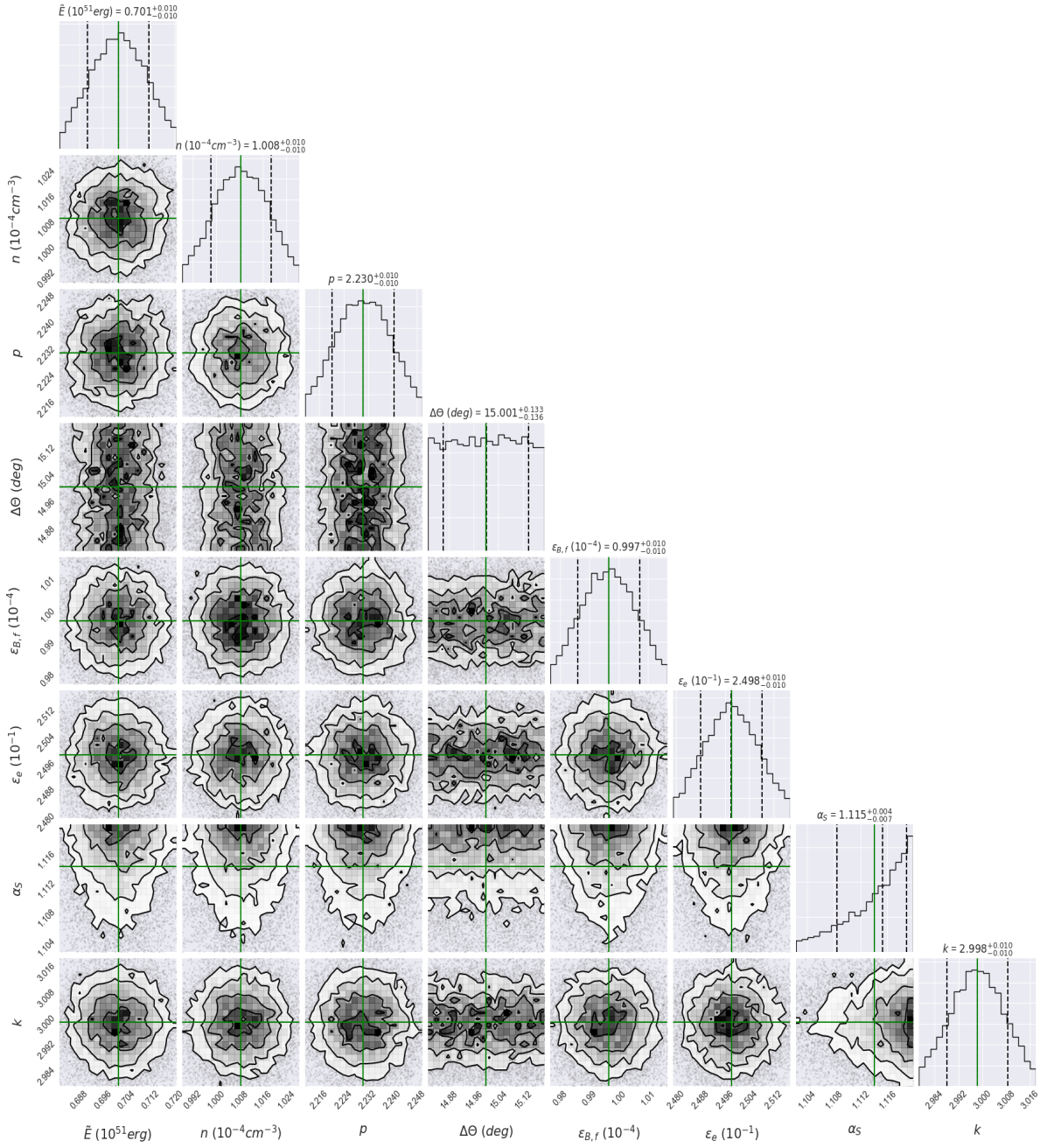


Figura 9 – Idem à Fig. 8, mas usando um modelo de sincrotron em *forward shock* para ajustar os dados de Raios-X quando o jato produzindo a emissão *afterglow* não está alinhado com a linha de visão do observador e a matéria no escoamento é parametrizada através de uma distribuição de velocidades de lei de potências. Modelo descrito em 3.2.

## 3.4 Análise e Implicações

### 3.4.1 Os parâmetros microfísicos magnéticos

(Sari; Mészáros, 2000) derivaram as escalas temporais hidrodinâmicas do *reverse shock* para um jato de GRB não-magnetizado. Eles encontraram que na ausência de magnetização o tempo de cruzamento se torna  $t_{cr} \simeq \frac{T_{90}}{2}$ . As escalas temporais hidrodinâmicas do *reverse shock* causado por um escoamento magnetizado foram investigadas por (Fan; Wei; Zhang, 2004; Zhang; Kobayashi, 2005a) e (Mimica; Giannios; Aloy, 2009; Mimica; Giannios; Aloy, 2010). Os autores reportaram que características gerais no *reverse shock* variam de acordo com o grau de magnetização do jato. Por exemplo, quando o jato estava moderadamente magnetizado, com parâmetro de magnetização na faixa de  $0.1 \lesssim \sigma \lesssim 1$ , então o parâmetro microfísico magnético variaria entre  $0.1 \lesssim \varepsilon_{B,r} \lesssim 0.2$  e o comprimento do pico gerado pelo *reverse shock* se torna mais estreito e proeminente entre  $\frac{T_{90}}{2} \lesssim t_{cr} \lesssim \frac{T_{90}}{2}$ . Esse resultado concorda com o valor do parâmetro microfísico magnético encontrado após descrever os dados do GBM e a duração do pico brilhante ( $\sim 0.4$  s) observado na curva de luz. Se o jato relativístico tivesse alta magnetização ( $\sigma \gg 1$ ) quando ele cruza o *reverse shock*, partículas relativísticas seriam aceleradas de maneira ineficiente e a emissão seria drasticamente reduzida (Sironi; Spitkovsky, 2011; Zhang; Kobayashi, 2005a). Portanto, uma magnetização moderada ( $\sigma \lesssim 1$ ) é necessária para interpretar o pico brilhante, encontrado pelo GBM, em uma estrutura de *reverse shock* (Zhang; Yan, 2011; Kumar; Panaiteescu, 2003; Fan; Wei; Zhang, 2004). Os valores do parâmetro microfísico magnético (Tabelas 4 e 5) indicam que a razão entre campos magnéticos nas regiões de *forward* e *reverse shock* é  $\sim 40$ . Similarmente, os valores encontrados também ilustram que o fluxo de sincrotron é  $\sim 2.5 \times 10^3$  vezes mais forte no *reverse shock* do que no *forward shock*, tal que existem muito mais fôtons disponíveis para ser espalhados via IC no *reverse shock*. Isso sugere que o escoamento carregava um campo magnético significante, tal como o reportado no sGRB 090510 (Fraija et al., 2016).

Levando em consideração o valor inicial típico do raio do modelo de bola de fogo,  $r_i \sim 10^{6.5}$  cm (Lee; Ramirez-Ruiz; Page, 2004; Lee et al., 2005; Nakar, 2007), a energia cinética equivalente e o parâmetro microfísico magnético (Tabela 4), o campo magnético na base do jato é aproximadamente estimado de ser  $B \approx \sqrt{8\varepsilon_{B,i}E_{\gamma,iso}/r_i^3} \approx 10^{15}G$ . Aqui,  $\varepsilon_{B,i} \approx \varepsilon_{B,r}$  é a fração de energia total inicial fornecida ao campo magnético. A magnitude do campo magnético é de três ou quatro ordens de grandeza superior à magnitude usual de uma NS,  $\sim 10^{12}$  G. Isto mostra que o GRB170817A requer um campo magnético mais intenso na base do jato, indicando que o progenitor estava emanharado com fortes campos magnéticos.

(Just et al., 2016) apresentou simulações hidrodinâmicas relativísticas, com simetria axial, de um sistema BH-Toro como remanescente de um sistema NS binário. Eles mostram

que a energia térmica, via aniquilação de neutrinos e anti-neutrinos, abundantemente emitidas pela acreção quente no disco não é longa e forte o suficiente para que escoamentos escapem do vento de neutrinos, concluindo assim que aniquilação de neutrino por si só não é suficiente para gerar um sGRB numa fusão de sistema NS binário. Portanto requisitos energéticos favorecem campos magnéticos como o mecanismo responsável pelo escape do escoamento. Alguns autores apresentaram simulações baseadas na magneto-hidrodinâmica relativística geral com o objetivo de seguir a evolução dos campos magnéticos na fusão de um sistema NS binário (Price; Rosswog, 2006; Zrake; MacFadyen, 2013; Ciolfi et al., 2017). Todos os modelos propostos demonstram uma amplificação do campo magnético de três ordens de magnitude ou mais. O crescimento rápido deste campo é atribuído a instabilidades de Kelvin-Helmholtz, turbulência e rotação diferencial. Portanto, o processo mais natural associado com a magnetização do escoamento é a amplificação do campo magnético durante a fusão do sistema binário.

### 3.4.2 Outros Parâmetros

1. Os valores das densidades do meio externo requerido para modelar os dados de Raios  $\gamma$  do GBM  $\sim 1.7$  s após a fusão (ver Tabela 4) e os dados de Raios-X, Óptico e Rádio (ver Tabela 5) são consideravelmente distintos, indicando que a emissão de Raios  $\gamma$  e o *afterglow* ocorreram em regiões diferentes. Isso sugere que a distribuição de densidade externa pode ser estratificada, como proposto em sGRBs (Parsons; Ramirez-Ruiz; Lee, 2009). Fusões de sistemas binários NS são consideradas possíveis candidatos para ejetar significantes quantidades de massa com velocidades e densidades distintas. As massas ejetadas com densidades maiores do que o meio ISM baixo são ejetadas com velocidades sub-relativísticas. Em princípio, o jato ultra-relativístico vindo do progenitor poderia interagir com este material denso e produzir um *afterglow* (Hotokezaka et al., 2013; Hotokezaka; Piran, 2015a; Kyutoku; Ioka; Shibata, 2014; Tan; Matzner; McKee, 2001; Fraija; Pedreira; Veres, 2018). Ainda mais, ajustes do *afterglow* de múltiplos comprimentos de onda sugerem que o ICM próximo ao progenitor pode ser denso e formado por ambientes gasosos, ao invés do assumido ISM baixo (Berger; Kulkarni; Frail, 2003; Panaiteescu; Kumar, 2001; Nakar; Piran, 2011). O valor baixo do ISM confirmaria que sGRBs de fato explodem em ambientes de baixa densidade.
2. Os valores dos índices espectrais eletrônicos para o fluxo de Raios  $\gamma$  e fluxos de Raios-X, Óptico e Rádio são iguais. Esses índices espectrais correspondem aos valores típicos reportados em choques externos  $2.2 \leq p \leq 2.6$  (Kumar; Panaiteescu, 2000). Isso sugere que o fluxo de Raios  $\gamma$  reportado pelo GBM pode ter originado em choques externos. Resultados similares foram encontrados em múltiplas erupções que exibiram picos iniciais sub-GeV em Raios  $\gamma$  e Óptico juntamente com emissões

temporalmente estendidas em múltiplos comprimentos de onda (Kobayashi et al., 2007; Kobayashi; Piran; Sari, 1997; Fraija et al., 2016; Fraija et al., 2017; Fraija, 2015).

3. Dois cenários são discutidos para explicar o GRB170817A (Murgia-Berthier et al., 2017): um sGRB de baixa luminosidade e um sGRB típico visto fora do eixo. Enquanto um sGRB de baixa luminosidade pode ser produzido por um escoamento levemente relativístico (Rosswog, 2005), um sGRB típico é gerado por um jato relativístico (Ramirez-Ruiz et al., 2005; Murgia-Berthier et al., 2014). Em ambos os casos um jato relativístico é invocado, porém no primeiro caso o jato é suprimido pelo vento expelido pela estrela de nêutrons hiper massiva (*hyper massive neutron star*, HMNS), dando surgimento então ao sGRB de baixa luminosidade com  $E_{\gamma,iso} = 10^{46} - 10^{47}$  erg. Considerando os valores da energia equivalente que nós estimamos para este evento (Tabelas 4 e 5), nós sugerimos que o cenário mais provável para o GRB170817A é o de um jato que escapa com sucesso do vento e é visualizado fora do eixo. Esse resultado concorda com o trabalho recente por (Mooley et al., 2018), onde os autores apresentam observações por Interferometria de Base Muito Longa (*Very Long Baseline Interferometry*, VLBI) mostrando movimento superluminal que suporta o argumento de êxito no escape do jato.
4. A colimação do jato carrega implicações relevantes em GRBs. Por exemplo, a escala energética, o mecanismo de extração de energia e a taxa de eventos. Para sGRBs existem apenas algumas observações de *jet breaks* apesar das diversas tentativas. Baseado nas quebras detectadas na emissão de *afterglow*, (Berger; Kulkarni; Frail, 2003) mostrou uma distribuição de ângulos de abertura do jato para sGRBs com média em torno de  $\theta_j \sim \langle 5^\circ \rangle$ . Recentemente, um valor similar para o ângulo de abertura foi obtido após modelar o *afterglow* do GRB170817A (Troja et al., 2018; Granot; Guetta; Gill, 2017). Levando em conta o valor  $\theta_j = 5^\circ$ , o angulo de visão pro GRB170817A seria  $\theta_{obs} = 20^\circ$  que está na faixa de valores reportada para esta erupção (Margutti et al., 2018; Granot; Guetta; Gill, 2017; Margutti et al., 2017; Troja et al., 2018; Mooley et al., 2018).
5. Considerando os valores reportados juntamente às equações 3.11 e 3.13, o fator de Lorentz de grupo é  $\Gamma \simeq 8.7$  e a energia cinética equivalente é  $E_k \simeq 3.3 \times 10^{47}$  erg. Comparando com a energia isotrópica observada  $E_{\gamma,iso} \simeq 5^{46}$  erg, a eficiência correspondente se torna  $\eta \simeq 15\%$ , o que está nos valores típicos encontrados para *afterglows* (Kumar; Zhang, 2015).

## 4 Conclusões e Perspectivas

Nós analisamos as observações não-térmicas (Raios  $\gamma$ , Raios-X, Óptico e Rádio) do GRB170817A/GW170817. Os dados de Raios-X, Óptico e Rádio se mostraram consistentes com um modelo de sincrotron em *forward shock* quando a matéria ejetada é parametrizada em uma distribuição de velocidades de lei de potência e o jato é visto fora do eixo. A origem do pico de Raios  $\gamma$  foi discutida em termos de choques internos e internos. A análise realizada favorece um modelo de SSC em *reverse shock* em um regime de resfriamento rápido e observado a altas latitudes. O ajuste dos dados de Raios  $\gamma$ , obtidos pelo GBM, com o modelo SSC sugere que:

- O ICM próximo ao progenitor é muito mais denso do que o baixo ISM obtido após modelagem dos dados de Raios-X, Óptico e Rádio. Uma possível explicação sugere que a distribuição de densidade externa seja estratificada, tais como sugeridos para sGRBs (Parsons; Ramirez-Ruiz; Lee, 2009; Hotokezaka et al., 2013; Hotokezaka; Piran, 2015b; Kyutoku; Ioka; Shibata, 2014; Tan; Matzner; McKee, 2001; Fraija; Pedreira; Veres, 2018). Este ICM próximo ao progenitor poderia ser formado por ambientes gasosos e/ou matéria densa ejetada ao invés do meio de baixa densidade da galáxia hospedeira. Isto sugere que o *afterglow* e emissão de Raios  $\gamma$  ocorreram em diferentes regiões.
- O valor dos índices espectrais eletrônicos ilustram que essa componente pode ter sido originada em choques externos. Discussões similares foram previamente realizadas sobre as componentes temporalmente estendidas vistas pelo Fermi-LAT (Kobayashi et al., 2007; Kobayashi; Piran; Sari, 1997; Fraija et al., 2016; Fraija et al., 2017; Fraija, 2015).
- O valor do parâmetro microfísico magnético obtido concorda com as propriedades temporais exibidas pela erupção e também que a magnitude do campo magnético é de três ou quatro ordens de magnitude maior do que o campo magnético típico de uma NS. Comparando os parâmetros microfísicos magnéticos obtidos para o fluxo de Raios  $\gamma$  com as observações de Raios-X, Óptico e Rádio mostra que o campo magnético na região de *reverse shock* aparenta ser aproximadamente 40 vezes maior do que a região de *forward shock*. Isso sugere que o escoamento carregava um campo magnético significante, como reportado para o GRB090510 (Fraija et al., 2016).

O valor da energia cinética equivalente concorda com as simulações realizadas sobre as condições necessárias para a produção de sGRBs na fusão de sistemas binários de NS (Murguia-Berthier et al., 2014). Isso sugere que o cenário de colapso para um

buraco negro com a formação de um sGRB fora do eixo típico favorece o cenário em que o vento expelido por um HMNS dificulta o movimento dianteiro de um jato no eixo. Como GRB170817A foi o sGRB mais próximo com redshift medido, este foi proposto como possível alvo para observação de neutrinos. Entretanto, os observatórios Antares, IceCube e Auger reportaram um resultado nulo com base em uma busca durante as fases imediata e de *afterglow* (Albert et al., 2017). Como mostrado por (Gao; Kashiyama; Mészáros, 2013; Fraija et al., 2017), a falta de neutrinos energéticos ao redor do GRB170817A pode estar relacionado com o grau de magnetização do material ejetado, o que dificulta a aceleração eficiente de partículas (Sironi; Spitkovsky, 2011).

Uma das erupções curtas mais energéticas, GRB090510 localizada em  $z = 0.903$ , foi detectada pelos satélites Fermi e Swift (De Pasquale et al., 2010). Este sGRB visto no eixo exibiu um pico de curta duração ao fim da fase imediata ( $T_{90} = 0.3$  s) e uma componente temporalmente estendida durando centenas de segundos. Adicionalmente o *Ultra Violet and Optical Telescope* (UVOT) abordo do satélite *Swift* começou a coletar dados Ópticos 97 s após a fase inicial (Kuin; Hoversten, 2009). A emissão de *afterglow* Óptico foi descrito em uma lei de potências em partes com os parâmetros de melhor ajuste: uma inclinação de decaimento inicial de  $-0.50^{+0.11}_{-0.13}$ , um tempo de quebra de  $1.58^{+0.46}_{-0.37} \times 10^3$  s, uma inclinação de decaimento tardio de  $1.13^{+0.11}_{-0.13}$  e densidade de fluxo de  $\sim 10^{-13}$  erg cm $^{-2}$  s $^{-1}$  um dia após a fase inicial. (Fraija et al., 2016) usou um modelo inicial-*afterglow* para interpretar as observações e curva de luz de múltiplos comprimentos de onda. Em particular, a emissão SSC do *reverse shock* era consistente com o pico brilhante LAT provendo que o progenitor possuía fortes campos magnéticos, assim associando o progenitor à uma fusão de um sistema binário NS. A curva de luz Óptica foi descrita por uma emissão de sincrotron no *forward shock* em regime de resfriamento lento antes e depois do tempo de quebra. Uma análise similar para uma emissão fora do eixo foi feita neste trabalho para o GRB170817A. O pico brilhante de Raios  $\gamma$  foi consistente com radiação SSC no regime de resfriamento rápido e o *afterglow* em múltiplos comprimentos de onda com emissão síncrotron, no regime de resfriamento lento, em diferentes regiões. Portanto, nós argumentamos que no GRB170817A se apresentou os efeitos dos processos de amplificação relacionados à coalescência do sistema binário. Esta erupção em particular não apresentou fôtons de alta energia ( $> 100 MeV$ ), muito provavelmente, devido ao quantidade de partículas carregadas na região da erupção (Kocevski; Fermi-LAT Collaboration, 2017), a emissão fora do eixo e a baixa energia isotrópica.

Observações de ondas gravitacionais provenientes da fusão do sistema binário associado a esse GRB (von Kienlin; Meegan; Goldstein, 2017; Goldstein et al., 2017) colocam o cenário de objeto compacto pós-fusão em nova luz. Como continuação deste trabalho nós pretendemos utilizar deste modelo, e variações como a apresentada no artigo 2 Anexo A onde introduzimos uma componente de choque de fuga (do inglês *shock breakout*, a camada mais externa das NSs que são ejetadas durante a fusão), para contínua

análise da componente eletromagnética das associações GRB-GW. Analises similares às apresentadas aqui, e nos artigos em anexo, em sGRBs futuros podem iluminar a natureza dos progenitores, evolução do campo magnético e a contraparte Óptica relacionada a associação de sGRBs-GW.



# Referências

- Abbott, B. P. et al. Gravitational Waves and Gamma-Rays from a Binary Neutron Star Merger: GW170817 and GRB 170817A. *ApJ*, v. 848, p. L13, out. 2017. Citado na página [32](#).
- Abbott, B. P. et al. Multi-messenger Observations of a Binary Neutron Star Merger. *ApJ*, v. 848, p. L12, out. 2017. Citado 2 vezes nas páginas [32](#) e [33](#).
- Ackermann, M. et al. The First Fermi-LAT Gamma-Ray Burst Catalog. *ApJS*, v. 209, p. 11, nov. 2013. Citado na página [35](#).
- Albert, A. et al. Search for High-energy Neutrinos from Binary Neutron Star Merger GW170817 with ANTARES, IceCube, and the Pierre Auger Observatory. *ApJ*, v. 850, p. L35, dez. 2017. Citado na página [58](#).
- Alexander, K. D. et al. A Decline in the X-Ray through Radio Emission from GW170817 Continues to Support an Off-axis Structured Jet. *ApJ*, v. 863, p. L18, ago. 2018. Citado 4 vezes nas páginas [15](#), [33](#), [43](#) e [47](#).
- Band, D. et al. BATSE observations of gamma-ray burst spectra. I - Spectral diversity. *ApJ*, v. 413, p. 281–292, ago. 1993. Citado na página [27](#).
- Barniol Duran, R. et al. The afterglow of a relativistic shock breakout and low-luminosity GRBs. *MNRAS*, v. 448, p. 417–428, mar. 2015. Citado na página [45](#).
- Berger, E.; Kulkarni, S.; Frail, D. A Standard Kinetic Energy Reservoir in Gamma-Ray Burst Afterglows. *ApJ*, v. 590, p. 379–385, jun. 2003. Citado 4 vezes nas páginas [27](#), [28](#), [55](#) e [56](#).
- Blandford, R. D.; McKee, C. F. Fluid dynamics of relativistic blast waves. *Physics of Fluids*, v. 19, p. 1130–1138, ago. 1976. Citado 2 vezes nas páginas [41](#) e [45](#).
- Bloom, J. S. et al. The unusual afterglow of the  $\gamma$ -ray burst of 26 March 1998 as evidence for a supernova connection. *Nature*, v. 401, p. 453–456, set. 1999. Citado na página [30](#).
- Bloom, J. S. et al. Detection of a Supernova Signature Associated with GRB 011121. *ApJ*, v. 572, p. L45–L49, jun. 2002. Citado na página [30](#).
- BLOOM, J. S.; SIGURDSSON, S. A cosmic multimessenger gold rush. *Science*, American Association for the Advancement of Science, v. 358, n. 6361, p. 301–302, 2017. ISSN 0036-8075. Disponível em: <<http://science.sciencemag.org/content/358/6361/301>>. Citado na página [33](#).
- Brun, R.; Rademakers, F. ROOT - An object oriented data analysis framework. *Nuclear Instruments and Methods in Physics Research A*, v. 389, p. 81–86, fev. 1997. Citado na página [37](#).
- Burrows, D. N. et al. Bright X-ray Flares in Gamma-Ray Burst Afterglows. *Science*, v. 309, p. 1833–1835, set. 2005. Citado na página [38](#).

Campana, S. et al. The association of GRB 060218 with a supernova and the evolution of the shock wave. *Nature*, v. 442, p. 1008–1010, ago. 2006. Citado na página 30.

Cenko, S. B. et al. The Collimation and Energetics of the Brightest Swift Gamma-ray Bursts. *ApJ*, v. 711, p. 641–654, mar. 2010. Citado 2 vezes nas páginas 27 e 28.

CENTER, N. G. S. F. *Long GRB Structure*. 2015. Disponível em: <<https://news.psu.edu/story/352406/2015/04/13/research/inside-most-powerful-explosions>>. Citado na página 29.

Chevalier, R. A.; Li, Z.-Y. Gamma-Ray Burst Environments and Progenitors. *ApJ*, v. 520, p. L29–L32, jul. 1999. Citado na página 30.

Chevalier, R. A.; Li, Z.-Y. Wind Interaction Models for Gamma-Ray Burst Afterglows: The Case for Two Types of Progenitors. *ApJ*, v. 536, p. 195–212, jun. 2000. Citado na página 31.

Chornock, R. et al. Spectroscopic Discovery of the Broad-Lined Type Ic Supernova 2010bh Associated with the Low-Redshift GRB 100316D. *ArXiv e-prints*, abr. 2010. Citado na página 30.

Ciolfi, R. et al. General relativistic magnetohydrodynamic simulations of binary neutron star mergers forming a long-lived neutron star. *Phys. Rev. D*, v. 95, n. 6, p. 063016, mar. 2017. Citado na página 55.

Coburn, W.; Boggs, S. E. Polarization of the prompt  $\gamma$ -ray emission from the  $\gamma$ -ray burst of 6 December 2002. *Nature*, v. 423, p. 415–417, maio 2003. Citado na página 32.

Costa, E. et al. Discovery of an X-ray afterglow associated with the  $\gamma$ -ray burst of 28 February 1997. *Nature*, v. 387, p. 783–785, jun. 1997. Citado na página 27.

Coulter, D. A. et al. Swope Supernova Survey 2017a (SSS17a), the optical counterpart to a gravitational wave source. *Science*, v. 358, p. 1556–1558, dez. 2017. Citado na página 32.

Curran, P. A.; van der Horst, A. J.; Wijers, R. A. M. J. Are the missing X-ray breaks in gamma-ray burst afterglow light curves merely hidden? *MNRAS*, v. 386, p. 859–863, maio 2008. Citado 2 vezes nas páginas 27 e 28.

Dai, Z. G.; Lu, T.  $\gamma$ -Ray Bursts and Afterglows from Rotating Strange Stars and Neutron Stars. *Physical Review Letters*, v. 81, p. 4301–4304, nov. 1998. Citado na página 30.

De Pasquale, M. et al. Swift and Fermi Observations of the Early Afterglow of the Short Gamma-Ray Burst 090510. *ApJ*, v. 709, p. L146–L151, fev. 2010. Citado na página 58.

Derishev, E. V. Synchrotron emission in the fast cooling regime: which spectra can be explained? *Ap&SS*, v. 309, p. 157–161, jun. 2007. Citado na página 39.

Dermer, C. D.; Chiang, J.; Mitman, K. E. Beaming, Baryon Loading, and the Synchrotron Self-Compton Component in Gamma-Ray Bursts. *ApJ*, v. 537, p. 785–795, jul. 2000. Citado na página 32.

Dobie, D. et al. A Turnover in the Radio Light Curve of GW170817. *ApJ*, v. 858, p. L15, maio 2018. Citado na página 33.

- Eichler, D. et al. Nucleosynthesis, neutrino bursts and gamma-rays from coalescing neutron stars. *Nature*, v. 340, p. 126–128, jul. 1989. Citado na página 31.
- Fan, Y. Z.; Wei, D. M.; Zhang, B.  $\gamma$ -ray burst internal shocks with magnetization. *MNRAS*, v. 354, p. 1031–1039, nov. 2004. Citado na página 54.
- Foreman-Mackey, D. corner.py: Scatterplot matrices in python. *The Journal of Open Source Software*, v. 24, 2016. Disponível em: <<http://dx.doi.org/10.5281/zenodo.45906>>. Citado na página 48.
- Fraija, N. GRB 110731A: Early Afterglow in Stellar Wind Powered By a Magnetized Outflow. *ApJ*, v. 804, p. 105, maio 2015. Citado 4 vezes nas páginas 31, 42, 56 e 57.
- Fraija, N.; González, M. M.; Lee, W. H. Synchrotron Self-Compton Emission as the Origin of the Gamma-Ray Afterglow Observed in GRB 980923. *ApJ*, v. 751, p. 33, maio 2012. Citado na página 31.
- Fraija, N.; González, M. M.; Lee, W. H. Synchrotron Self-Compton Emission as the Origin of the Gamma-Ray Afterglow Observed in GRB 980923. *ApJ*, v. 751, p. 33, maio 2012. Citado na página 43.
- Fraija, N.; Lee, W.; Veres, P. Modeling the Early Multiwavelength Emission in GRB130427A. *ApJ*, v. 818, p. 190, fev. 2016. Citado na página 31.
- Fraija, N. et al. Modeling the High-energy Emission in GRB 110721A and Implications on the Early Multiwavelength and Polarimetric Observations. *ApJ*, v. 848, p. 94, out. 2017. Citado 5 vezes nas páginas 31, 32, 39, 40 e 41.
- Fraija, N. et al. Modeling the Early Afterglow in the Short and Hard GRB 090510. *ApJ*, v. 831, p. 22, nov. 2016. Citado 9 vezes nas páginas 31, 32, 38, 39, 42, 54, 56, 57 e 58.
- Fraija, N.; Pedreira, A. C. C. d. E. S.; Veres, P. Light curves of a merger shock-breakout material ejected from a Binary Neutron Star system. *ArXiv e-prints*, mar. 2018. Citado 3 vezes nas páginas 45, 55 e 57.
- Fraija, N. et al. Theoretical Description of GRB 160625B with Wind-to-ISM Transition and Implications for a Magnetized Outflow. *ApJ*, v. 848, p. 15, out. 2017. Citado 4 vezes nas páginas 31, 56, 57 e 58.
- Frail, D. A. et al. Beaming in Gamma-Ray Bursts: Evidence for a Standard Energy Reservoir. *ApJ*, v. 562, p. L55–L58, nov. 2001. Citado 2 vezes nas páginas 27 e 28.
- Frontera, F. et al. Spectral Properties of the Prompt X-Ray Emission and Afterglow from the Gamma-Ray Burst of 1997 February 28. *ApJ*, v. 493, p. L67–L70, fev. 1998. Citado na página 27.
- Galama, T. J. et al. An unusual supernova in the error box of the  $\gamma$ -ray burst of 25 April 1998. *Nature*, v. 395, p. 670–672, out. 1998. Citado na página 30.
- Gao, S.; Kashiyama, K.; Mészáros, P. On the Neutrino Non-detection of GRB 130427A. *ApJ*, v. 772, p. L4, jul. 2013. Citado na página 58.
- Ghisellini, G.; Celotti, A. Quasi-thermal comptonization and GRBs. *A&AS*, v. 138, p. 527–528, set. 1999. Citado na página 30.

Giacomazzo, B.; Rezzolla, L.; Baiotti, L. Can magnetic fields be detected during the inspiral of binary neutron stars? *MNRAS*, v. 399, p. L164–L168, out. 2009. Citado na página 31.

Giannios, D.; Spruit, H. C. Spectral and timing properties of a dissipative  $\gamma$ -ray burst photosphere. *A&A*, v. 469, p. 1–9, jul. 2007. Citado na página 30.

Goldstein, A. et al. An Ordinary Short Gamma-Ray Burst with Extraordinary Implications: Fermi-GBM Detection of GRB 170817A. *ApJ*, v. 848, p. L14, out. 2017. Citado 2 vezes nas páginas 32 e 58.

Gorbovskoy, E. S. et al. Early polarization observations of the optical emission of gamma-ray bursts: GRB 150301B and GRB 150413A. *MNRAS*, v. 455, p. 3312–3318, jan. 2016. Citado 2 vezes nas páginas 31 e 32.

Granot, J.; Guetta, D.; Gill, R. Lessons from the Short GRB 170817A: The First Gravitational-wave Detection of a Binary Neutron Star Merger. *ApJ*, v. 850, p. L24, dez. 2017. Citado na página 56.

Granot, J. et al. Off-Axis Afterglow Emission from Jetted Gamma-Ray Bursts. *ApJ*, v. 570, p. L61–L64, maio 2002. Citado na página 32.

Guetta, D.; Spada, M.; Waxman, E. Efficiency and Spectrum of Internal Gamma-Ray Burst Shocks. *ApJ*, v. 557, p. 399–407, ago. 2001. Citado na página 40.

Haggard, D.; Nynka, M.; Ruan, J. J. Chandra X-ray observations of GW170817 at 1 year post-merger: increasingly rapid fading. *The Astronomer's Telegram*, v. 11945, ago. 2018. Citado 3 vezes nas páginas 15, 43 e 47.

Hallinan, G. et al. A radio counterpart to a neutron star merger. *Science*, v. 358, p. 1579–1583, dez. 2017. Citado 4 vezes nas páginas 15, 33, 43 e 47.

Hastings, W. K. Monte carlo sampling methods using markov chains and their applications. *Biometrika*, v. 57, n. 1, p. 97–109, 1970. Disponível em: <<http://dx.doi.org/10.1093/biomet/57.1.97>>. Citado na página 36.

Hjorth, J. et al. A very energetic supernova associated with the  $\gamma$ -ray burst of 29 March 2003. *Nature*, v. 423, p. 847–850, jun. 2003. Citado na página 30.

Hotokezaka, K. et al. Progenitor Models of the Electromagnetic Transient Associated with the Short Gamma Ray Burst 130603B. *ApJ*, v. 778, p. L16, nov. 2013. Citado 3 vezes nas páginas 45, 55 e 57.

Hotokezaka, K.; Piran, T. Mass ejection from neutron star mergers: different components and expected radio signals. *MNRAS*, v. 450, p. 1430–1440, jun. 2015. Citado 3 vezes nas páginas 31, 45 e 55.

Hotokezaka, K.; Piran, T. Mass ejection from neutron star mergers: different components and expected radio signals. *MNRAS*, v. 450, p. 1430–1440, jun. 2015. Citado 2 vezes nas páginas 45 e 57.

Ioka, K. et al. Unstable GRB Photospheres and  $e^{+/-}$  Annihilation Lines. *ApJ*, v. 670, p. L77–L80, dez. 2007. Citado 2 vezes nas páginas 30 e 39.

Ioka, K.; Nakamura, T. Can an Off-axis Gamma-Ray Burst Jet in GW170817 Explain All the Electromagnetic Counterparts? 2017. Citado 2 vezes nas páginas [41](#) e [43](#).

Just, O. et al. Neutron-star Merger Ejecta as Obstacles to Neutrino-powered Jets of Gamma-Ray Bursts. *ApJ*, v. 816, p. L30, jan. 2016. Citado na página [54](#).

Kasen, D.; Badnell, N. R.; Barnes, J. Opacities and Spectra of the r-process Ejecta from Neutron Star Mergers. *ApJ*, v. 774, p. 25, set. 2013. Citado na página [31](#).

Kobayashi, S. Light Curves of Gamma-Ray Burst Optical Flashes. *ApJ*, v. 545, p. 807–812, dez. 2000. Citado 2 vezes nas páginas [39](#) e [41](#).

Kobayashi, S.; Piran, T.; Sari, R. Can Internal Shocks Produce the Variability in Gamma-Ray Bursts? *ApJ*, v. 490, p. 92, nov. 1997. Citado 3 vezes nas páginas [38](#), [56](#) e [57](#).

Kobayashi, S.; Zhang, B. Early Optical Afterglows from Wind-Type Gamma-Ray Bursts. *ApJ*, v. 597, p. 455–458, nov. 2003. Citado na página [31](#).

Kobayashi, S. et al. Inverse Compton X-Ray Flare from Gamma-Ray Burst Reverse Shock. *ApJ*, v. 655, p. 391–395, jan. 2007. Citado 6 vezes nas páginas [31](#), [38](#), [39](#), [41](#), [56](#) e [57](#).

Kocevski, D.; Fermi-LAT Collaboration. *GRB Coordinates Network*, v. 21534, 2017. Citado na página [58](#).

Kopač, D. et al. Limits on Optical Polarization during the Prompt Phase of GRB 140430A. *ApJ*, v. 813, p. 1, nov. 2015. Citado 2 vezes nas páginas [31](#) e [32](#).

Kuin, N. P. M.; Hoversten, E. A. GRB 090510: UVOT refined analysis. *GRB Coordinates Network*, v. 9342, 2009. Citado na página [58](#).

Kumar, P.; Barniol Duran, R. On the generation of high-energy photons detected by the Fermi Satellite from gamma-ray bursts. *MNRAS*, v. 400, p. L75–L79, nov. 2009. Citado na página [30](#).

Kumar, P.; Panaiteescu, A. Afterglow Emission from Naked Gamma-Ray Bursts. *ApJ*, v. 541, p. L51–L54, out. 2000. Citado 3 vezes nas páginas [32](#), [39](#) e [55](#).

Kumar, P.; Panaiteescu, A. A unified treatment of the gamma-ray burst 021211 and its afterglow. *MNRAS*, v. 346, p. 905–914, dez. 2003. Citado 3 vezes nas páginas [38](#), [42](#) e [54](#).

Kumar, P.; Zhang, B. The physics of gamma-ray bursts & relativistic jets. *Phys. Rep.*, v. 561, p. 1–109, fev. 2015. Citado 3 vezes nas páginas [27](#), [39](#) e [56](#).

Kyutoku, K.; Ioka, K.; Shibata, M. Ultrarelativistic electromagnetic counterpart to binary neutron star mergers. *MNRAS*, v. 437, p. L6–L10, jan. 2014. Citado 3 vezes nas páginas [45](#), [55](#) e [57](#).

Lattimer, J. M.; Schramm, D. N. Black-hole-neutron-star collisions. *ApJ*, v. 192, p. L145–L147, set. 1974. Citado na página [31](#).

Lattimer, J. M.; Schramm, D. N. The tidal disruption of neutron stars by black holes in close binaries. *ApJ*, v. 210, p. 549–567, dez. 1976. Citado na página [31](#).

Lee, W. H. et al. Dynamical Evolution of Neutrino-cooled Accretion Disks: Detailed Microphysics, Lepton-driven Convection, and Global Energetics. *ApJ*, v. 632, p. 421–437, out. 2005. Citado 2 vezes nas páginas [31](#) e [54](#).

Lee, W. H.; Ramirez-Ruiz, E. The progenitors of short gamma-ray bursts. *New Journal of Physics*, v. 9, p. 17, jan. 2007. Citado na página [31](#).

Lee, W. H.; Ramirez-Ruiz, E.; Page, D. Opaque or Transparent? A Link between Neutrino Optical Depths and the Characteristic Duration of Short Gamma-Ray Bursts. *ApJ*, v. 608, p. L5–L8, jun. 2004. Citado 2 vezes nas páginas [31](#) e [54](#).

Li, L.-X.; Paczynski, B. Transient Events from Neutron Star Mergers. *ApJ*, v. 507, p. L59–L62, nov. 1998. Citado na página [31](#).

Liang, E.-W. et al. A Comprehensive Analysis of Swift XRT Data. III. Jet Break Candidates in X-Ray and Optical Afterglow Light Curves. *ApJ*, v. 675, p. 528–552, mar. 2008. Citado 2 vezes nas páginas [27](#) e [28](#).

Lu, R.-J.; Hou, S.-J.; Liang, E.-W. The  $E_p$ -flux Correlation in the Rising and Decaying Phases of gamma-ray Burst Pulses: Evidence for Viewing Angle Effect? *ApJ*, v. 720, p. 1146–1154, set. 2010. Citado na página [38](#).

Lyman, J. D. et al. The optical afterglow of the short gamma-ray burst associated with GW170817. *Nature Astronomy*, v. 2, p. 751–754, jul. 2018. Citado 2 vezes nas páginas [33](#) e [43](#).

Mao, S.; Paczynski, B. On the cosmological origin of gamma-ray bursts. *ApJ*, v. 388, p. L45–L48, abr. 1992. Citado na página [27](#).

Margutti, R. et al. The Binary Neutron Star Event LIGO/Virgo GW170817 160 Days after Merger: Synchrotron Emission across the Electromagnetic Spectrum. *ApJ*, v. 856, p. L18, mar. 2018. Citado 5 vezes nas páginas [15](#), [33](#), [43](#), [47](#) e [56](#).

Margutti, R. et al. The Electromagnetic Counterpart of the Binary Neutron Star Merger LIGO/Virgo GW170817. V. Rising X-Ray Emission from an Off-axis Jet. *ApJ*, v. 848, p. L20, out. 2017. Citado 5 vezes nas páginas [15](#), [33](#), [43](#), [47](#) e [56](#).

McMahon, E.; Kumar, P.; Panaitescu, A. Prompt  $\gamma$ -ray and early afterglow emission in the external shock model. *MNRAS*, v. 354, p. 915–923, nov. 2004. Citado na página [38](#).

McMahon, E.; Kumar, P.; Piran, T. Reverse shock emission as a probe of gamma-ray burst ejecta. *MNRAS*, v. 366, p. 575–585, fev. 2006. Citado na página [38](#).

Meegan, C. A. et al. Spatial distribution of gamma-ray bursts observed by BATSE. *Nature*, v. 355, p. 143–145, jan. 1992. Citado na página [27](#).

Melandri, A. et al. The optical SN 2012bz associated with the long GRB 120422A. *A&A*, v. 547, p. A82, nov. 2012. Citado na página [30](#).

Metzger, B. D.; Berger, E.; Margalit, B. Millisecond Magnetar Birth Connects FRB 121102 to Superluminous Supernovae and Long-duration Gamma-Ray Bursts. *ApJ*, v. 841, p. 14, maio 2017. Citado na página [31](#).

Metzger, B. D. et al. Electromagnetic counterparts of compact object mergers powered by the radioactive decay of r-process nuclei. *MNRAS*, v. 406, p. 2650–2662, ago. 2010. Citado na página 31.

Mimica, P.; Giannios, D.; Aloy, M. A. Deceleration of arbitrarily magnetized GRB ejecta: the complete evolution. *A&A*, v. 494, p. 879–890, fev. 2009. Citado na página 54.

Mimica, P.; Giannios, D.; Aloy, M. A. Multiwavelength afterglow light curves from magnetized gamma-ray burst flows. *MNRAS*, v. 407, p. 2501–2510, out. 2010. Citado na página 54.

Modjaz, M. et al. Early-Time Photometry and Spectroscopy of the Fast Evolving SN 2006aj Associated with GRB 060218. *ApJ*, v. 645, p. L21–L24, jul. 2006. Citado na página 30.

Mooley, K. P. et al. Superluminal motion of a relativistic jet in the neutron-star merger GW170817. *Nature*, v. 561, p. 355–359, set. 2018. Citado na página 56.

Mundell, C. G. et al. Highly polarized light from stable ordered magnetic fields in GRB 120308A. *Nature*, v. 504, p. 119–121, dez. 2013. Citado 2 vezes nas páginas 31 e 32.

Mundell, C. G. et al. Early Optical Polarization of a Gamma-Ray Burst Afterglow. *Science*, v. 315, p. 1822, mar. 2007. Citado 2 vezes nas páginas 31 e 32.

Murguia-Berthier, A. et al. Necessary Conditions for Short Gamma-Ray Burst Production in Binary Neutron Star Mergers. *ApJ*, v. 788, p. L8, jun. 2014. Citado 2 vezes nas páginas 56 e 57.

Murguia-Berthier, A. et al. A Neutron Star Binary Merger Model for GW170817/GRB 170817A/SSS17a. *ApJ*, v. 848, p. L34, out. 2017. Citado na página 56.

Nakar, E. Short-hard gamma-ray bursts. *Phys. Rep.*, v. 442, p. 166–236, abr. 2007. Citado 2 vezes nas páginas 31 e 54.

Nakar, E.; Piran, T. Early afterglow emission from a reverse shock as a diagnostic tool for gamma-ray burst outflows. *MNRAS*, v. 353, p. 647–653, set. 2004. Citado na página 38.

Nakar, E.; Piran, T. Detectable radio flares following gravitational waves from mergers of binary neutron stars. *Nature*, v. 478, p. 82–84, out. 2011. Citado 2 vezes nas páginas 46 e 55.

Narayan, R.; Paczynski, B.; Piran, T. Gamma-ray bursts as the death throes of massive binary stars. *ApJ*, v. 395, p. L83–L86, ago. 1992. Citado na página 31.

NASA. *Long and Short Gamma-ray Burst Models*. 2006. Disponível em: <[http://hubblesite.org/image/1916/news\\_release/2006-20/](http://hubblesite.org/image/1916/news_release/2006-20/)>. Citado na página 28.

Obergaulinger, M.; Aloy, M. A.; Müller, E. Local simulations of the magnetized Kelvin-Helmholtz instability in neutron-star mergers. *A&A*, v. 515, p. A30, jun. 2010. Citado na página 31.

O’Brien, P. T. et al. The Early X-Ray Emission from GRBs. *ApJ*, v. 647, p. 1213–1237, ago. 2006. Citado na página 39.

Panaiteescu, A. Swift gamma-ray burst afterglows and the forward-shock model. *MNRAS*, v. 379, p. 331–342, jul. 2007. Citado na página [39](#).

Panaiteescu, A.; Kumar, P. Fundamental Physical Parameters of Collimated Gamma-Ray Burst Afterglows. *ApJ*, v. 560, p. L49–L53, out. 2001. Citado 3 vezes nas páginas [27](#), [28](#) e [55](#).

Panaiteescu, A.; Kumar, P. Properties of Relativistic Jets in Gamma-Ray Burst Afterglows. *ApJ*, v. 571, p. 779–789, jun. 2002. Citado 2 vezes nas páginas [28](#) e [30](#).

Parsons, R. K.; Ramirez-Ruiz, E.; Lee, W. H. Short Gamma Ray Bursts and their Afterglow Signatures in Dense Stellar Systems. *ArXiv e-prints*, abr. 2009. Citado 2 vezes nas páginas [55](#) e [57](#).

Pe'er, A. Temporal Evolution of Thermal Emission from Relativistically Expanding Plasma. *ApJ*, v. 682, p. 463–473, jul. 2008. Citado na página [30](#).

Peng, Z. Y. et al. The  $E_p$  Evolutionary Slope Within the Decay Phase of “Fast Rise and Exponential Decay” Gamma-Ray Burst Pulses. *ApJ*, v. 698, p. 417–427, jun. 2009. Citado na página [38](#).

Pian, E. et al. An optical supernova associated with the X-ray flash XRF 060218. *Nature*, v. 442, p. 1011–1013, ago. 2006. Citado na página [30](#).

Piran, T. The implications of the Compton (GRO) observations for cosmological gamma-ray bursts. *ApJ*, v. 389, p. L45–L48, abr. 1992. Citado na página [27](#).

Piran, T. Gamma-ray bursts and the fireball model. *Phys. Rep.*, v. 314, p. 575–667, jun. 1999. Citado 2 vezes nas páginas [39](#) e [40](#).

Piran, T.; Nakar, E.; Rosswog, S. The electromagnetic signals of compact binary mergers. *MNRAS*, v. 430, p. 2121–2136, abr. 2013. Citado na página [31](#).

Price, D. J.; Rosswog, S. Producing Ultrastrong Magnetic Fields in Neutron Star Mergers. *Science*, v. 312, p. 719–722, maio 2006. Citado 2 vezes nas páginas [31](#) e [55](#).

Pruzhinskaya, M. V. et al. Optical polarization observations with the MASTER robotic net. *New A*, v. 29, p. 65–74, maio 2014. Citado 2 vezes nas páginas [31](#) e [32](#).

Racusin, J. L. et al. Jet Breaks and Energetics of Swift Gamma-Ray Burst X-Ray Afterglows. *ApJ*, v. 698, p. 43–74, jun. 2009. Citado 2 vezes nas páginas [27](#) e [28](#).

Ramirez-Ruiz, E. et al. An Off-Axis Model of GRB 031203. *ApJ*, v. 625, p. L91–L94, jun. 2005. Citado na página [56](#).

Rees, M. J. Some comments on triggers, energetics and beaming. *A&AS*, v. 138, p. 491–497, set. 1999. Citado 2 vezes nas páginas [32](#) e [46](#).

Rees, M. J.; Meszaros, P. Relativistic fireballs - Energy conversion and time-scales. *MNRAS*, v. 258, p. 41P–43P, set. 1992. Citado na página [30](#).

Rees, M. J.; Meszaros, P. Unsteady outflow models for cosmological gamma-ray bursts. *ApJ*, v. 430, p. L93–L96, ago. 1994. Citado na página [38](#).

- Rhoads, J. E. Gamma-ray burst beaming constraints from afterglow light curves. *A&AS*, v. 138, p. 539–540, set. 1999. Citado na página [27](#).
- Rosswog, S. Mergers of Neutron Star-Black Hole Binaries with Small Mass Ratios: Nucleosynthesis, Gamma-Ray Bursts, and Electromagnetic Transients. *ApJ*, v. 634, p. 1202–1213, dez. 2005. Citado 2 vezes nas páginas [31](#) e [56](#).
- Salvatier, J. e. a. Probabilistic programming in python using pymc3. *PeerJ Computer Science* 2, v. 55, 2016. Citado na página [48](#).
- Sari, R.; Mészáros, P. Impulsive and Varying Injection in Gamma-Ray Burst Afterglows. *ApJ*, v. 535, p. L33–L37, maio 2000. Citado 2 vezes nas páginas [45](#) e [54](#).
- Sari, R.; Piran, T. Hydrodynamic Timescales and Temporal Structure of Gamma-Ray Bursts. *ApJ*, v. 455, p. L143, dez. 1995. Citado 2 vezes nas páginas [27](#) e [41](#).
- Sari, R.; Piran, T.; Halpern, J. P. Jets in Gamma-Ray Bursts. *ApJ*, v. 519, p. L17–L20, jul. 1999. Citado na página [46](#).
- Sari, R.; Piran, T.; Narayan, R. Spectra and Light Curves of Gamma-Ray Burst Afterglows. *ApJ*, v. 497, p. L17–L20, abr. 1998. Citado 4 vezes nas páginas [39](#), [40](#), [44](#) e [46](#).
- Sironi, L.; Spitkovsky, A. Acceleration of Particles at the Termination Shock of a Relativistic Striped Wind. *ApJ*, v. 741, p. 39, nov. 2011. Citado 2 vezes nas páginas [54](#) e [58](#).
- Sparre, M. et al. Spectroscopic Evidence for SN 2010ma Associated with GRB 101219B. *ApJ*, v. 735, p. L24, jul. 2011. Citado na página [30](#).
- Stanek, K. Z. et al. Spectroscopic Discovery of the Supernova 2003dh Associated with GRB 030329. *ApJ*, v. 591, p. L17–L20, jul. 2003. Citado na página [30](#).
- Starling, R. L. C. et al. Discovery of the nearby long, soft GRB 100316D with an associated supernova. *MNRAS*, v. 411, p. 2792–2803, mar. 2011. Citado na página [30](#).
- Steele, I. A. et al. Ten per cent polarized optical emission from GRB090102. *Nature*, v. 462, p. 767–769, dez. 2009. Citado 2 vezes nas páginas [31](#) e [32](#).
- Tan, J. C.; Matzner, C. D.; McKee, C. F. The trans-relativistic blast wave model for SN 1998bw and GRB 980425. In: Wheeler, J. C.; Martel, H. (Ed.). *20th Texas Symposium on relativistic astrophysics*. [S.l.: s.n.], 2001. (American Institute of Physics Conference Series, v. 586), p. 638–640. Citado 3 vezes nas páginas [45](#), [55](#) e [57](#).
- Thompson, C. A Model of Gamma-Ray Bursts. *MNRAS*, v. 270, p. 480, out. 1994. Citado na página [30](#).
- Troja, E. et al. Significant and variable linear polarization during the prompt optical flash of GRB 160625B. *Nature*, v. 547, p. 425–427, jul. 2017. Citado 6 vezes nas páginas [15](#), [31](#), [32](#), [33](#), [43](#) e [47](#).
- Troja, E. et al. The outflow structure of GW170817 from late-time broad-band observations. *MNRAS*, v. 478, p. L18–L23, jul. 2018. Citado na página [56](#).
- Usov, V. V. Millisecond pulsars with extremely strong magnetic fields as a cosmological source of gamma-ray bursts. *Nature*, v. 357, p. 472–474, jun. 1992. Citado na página [32](#).

Veres, P. et al. Gamma-ray burst models in light of the GRB 170817A - GW170817 connection. *ArXiv e-prints*, fev. 2018. Citado 2 vezes nas páginas [38](#) e [39](#).

Vestrand, W. T. et al. Energy input and response from prompt and early optical afterglow emission in  $\gamma$ -ray bursts. *Nature*, v. 442, p. 172–175, jul. 2006. Citado 2 vezes nas páginas [15](#) e [37](#).

von Kienlin, A.; Meegan, C.; Goldstein, A. GRB 170817A: Fermi GBM detection. *GRB Coordinates Network, Circular Service, No. 21520, #1 (2017)*, v. 21520, 2017. Citado 4 vezes nas páginas [32](#), [35](#), [37](#) e [58](#).

Wang, X. Y.; Dai, Z. G.; Lu, T. Prompt High-Energy Gamma-Ray Emission from the Synchrotron Self-Compton Process in the Reverse Shocks of Gamma-Ray Bursts. *ApJ*, v. 546, p. L33–L37, jan. 2001. Citado na página [31](#).

Wang, X. Y.; Dai, Z. G.; Lu, T. The Inverse Compton Emission Spectra in the Very Early Afterglows of Gamma-Ray Bursts. *ApJ*, v. 556, p. 1010–1016, ago. 2001. Citado na página [31](#).

Wheeler, J. C. et al. Asymmetric Supernovae, Pulsars, Magnetars, and Gamma-Ray Bursts. *ApJ*, v. 537, p. 810–823, jul. 2000. Citado na página [32](#).

Zhang, B. et al. Physical Processes Shaping Gamma-Ray Burst X-Ray Afterglow Light Curves: Theoretical Implications from the Swift X-Ray Telescope Observations. *ApJ*, v. 642, p. 354–370, maio 2006. Citado na página [39](#).

Zhang, B.; Kobayashi, S. Gamma-Ray Burst Early Afterglows: Reverse Shock Emission from an Arbitrarily Magnetized Ejecta. *ApJ*, v. 628, p. 315–334, jul. 2005. Citado 2 vezes nas páginas [31](#) e [54](#).

Zhang, B.; Kobayashi, S. Gamma-Ray Burst Early Afterglows: Reverse Shock Emission from an Arbitrarily Magnetized Ejecta. *ApJ*, v. 628, p. 315–334, jul. 2005. Citado 2 vezes nas páginas [39](#) e [42](#).

Zhang, B.; Kobayashi, S.; Mészáros, P. Gamma-Ray Burst Early Optical Afterglows: Implications for the Initial Lorentz Factor and the Central Engine. *ApJ*, v. 595, p. 950–954, out. 2003. Citado 2 vezes nas páginas [31](#) e [39](#).

Zhang, B.; Mészáros, P. Gamma-Ray Bursts: progress, problems & prospects. *International Journal of Modern Physics A*, v. 19, p. 2385–2472, 2004. Citado 2 vezes nas páginas [27](#) e [31](#).

Zhang, B.; Yan, H. The Internal-collision-induced Magnetic Reconnection and Turbulence (ICMART) Model of Gamma-ray Bursts. *ApJ*, v. 726, p. 90, jan. 2011. Citado 2 vezes nas páginas [30](#) e [54](#).

Zrake, J.; MacFadyen, A. I. Magnetic Energy Production by Turbulence in Binary Neutron Star Mergers. *ApJ*, v. 769, p. L29, jun. 2013. Citado 2 vezes nas páginas [31](#) e [55](#).

## ANEXO A – Artigos aceitos para publicação

DRAFT VERSION DECEMBER 3, 2018  
 Preprint typeset using L<sup>A</sup>T<sub>E</sub>X style emulateapj v. 12/16/11

## THE SHORT GRB 170817A: MODELLING THE OFF-AXIS EMISSION AND IMPLICATIONS ON THE EJECTA MAGNETIZATION

N. FRAJJA<sup>1†</sup>, F. DE COLLE<sup>2</sup>, P. VERES<sup>3</sup>, S. DICHIARA<sup>1,4,5</sup>, R. BARNIOL DURAN<sup>6</sup>, A. GALVAN-GAMEZ<sup>1</sup> AND A.C. CALIGULA DO E. S. PEDREIRA<sup>1,7</sup>

<sup>1</sup> Instituto de Astronomía, Universidad Nacional Autónoma de México, Circuito Exterior, C.U., A. Postal 70-264, 04510 Cd. de México, México

<sup>2</sup> Instituto de Ciencias Nucleares, Universidad Nacional Autónoma de México, Circuito Exterior, C.U., A. Postal 70-264, 04510 Cd. de México, México

<sup>3</sup> Center for Space Plasma and Aeronomy Research (CSPAR), University of Alabama in Huntsville, Huntsville, AL 35899, USA

<sup>4</sup> Department of Astronomy, University of Maryland, College Park, MD 20742-4111, USA

<sup>5</sup> Astrophysics Science Division, NASA Goddard Space Flight Center, 8800 Greenbelt Rd, Greenbelt, MD 20771, USA

<sup>6</sup> Department of Physics and Astronomy, California State University, Sacramento, 6000 J Street, Sacramento, CA 95819-6041, USA

<sup>7</sup> Instituto de Matemática, Estatística e Física, Universidade Federal do Rio Grande, Rio Grande 96203-900, Brasil

*Draft version December 3, 2018*

### ABSTRACT

The short GRB 170817A, detected by the Fermi Gamma-ray Burst Monitor, orbiting satellites and ground-based telescopes, was the electromagnetic counterpart of a gravitational-wave transient (GW170817) from a binary neutron star merger. After this merger the  $\gamma$ -ray light curve exhibited a faint peak at  $\sim 1.7$ s and the X-ray, optical and radio light curves displayed an extended emission which increased in brightness up to  $\sim 160$  days. In this paper, we show that the X-ray, optical and radio fluxes are consistent with the synchrotron forward-shock model viewed off-axis when the matter in the outflow is parametrized through a power law velocity distribution. We discuss the origin of the  $\gamma$ -ray peak in terms of internal and external shocks. We show that the  $\gamma$ -ray flux might be consistent with a synchrotron self-Compton reverse-shock model observed at high latitudes. Comparing the best-fit values obtained after describing the  $\gamma$ -ray, X-ray, optical and radio fluxes with our model, we find that the afterglow and  $\gamma$ -ray emission occurred in different regions and also evidence to propose that the progenitor environment was entrained with magnetic fields and therefore, we argue for the presence of the magnetic field amplification in the binary neutron star merger.

*Subject headings:* gamma-rays bursts: individual (GRB 170817A) — Physical data and processes: acceleration of particles — Physical data and processes: radiation mechanism: nonthermal — ISM: general - magnetic fields

### 1. INTRODUCTION

One of the most fascinating extragalactic events are gamma-ray bursts (GRBs). They are known to exhibit a vast variety of spectral and temporal properties. Based on the standard GRB durations and spectral hardness two kind of progenitor populations have been amply accepted, short ( $T_{90} < 2$  s) and long ( $T_{90} > 2$  s) GRBs (for review, see Zhang & Mészáros 2004; Kumar & Zhang 2015). Although the discoveries and subsequent studies of long GRBs (IGRBs) have been marked by many successes, the study of short GRBs (sGRBs) has proven to be much more challenging. Significant advances in sGRBs were achieved with the discovery of the first host galaxies and the observations of multiwavelength afterglows (for reviews, see Nakar 2007; Berger 2014). Several lines of evidence have associated the sGRB progenitors with the merger of compact object binaries comprised of a neutron star binary (NS-NS) or a neutron star - black hole (NS-BH) (Eichler et al. 1989; Narayan et al. 1992; Lee & Ramirez-Ruiz 2007; Lee et al. 2004, 2005; Nakar 2007). These progenitors are promising candidates to release gravitational waves (GWs) accompanied by an isotropic optical/infrared counterpart, the so-called kilonova or macronova (Li & Paczyński 1998; Rosswog 2005; Metzger et al. 2010; Kasen et al. 2013; Metzger 2017). Because of neutron-rich ejecta from these progenitors, a kilonova/macronova is produced via radioactive decay of unstable heavy nuclei created in the rapid neutron capture

(r-process) nucleosynthesis (Lattimer & Schramm 1974, 1976). In addition, a cocoon emission and a delayed non-thermal radiation in radio wavelengths, originated from the interaction of the merger ejecta with the circumburst medium, are expected from these events (Nakar & Piran 2011; Piran et al. 2013; Hotokezaka & Piran 2015; Lazzati et al. 2017a,b). On the other hand, using two non-spinning magnetized NSs initially separated by 48 km with 1.4 solar masses, Price & Rosswog (2006) presented through simulations the magnetic field evolution in a binary NS merger. The main result is that the corresponding magnetic field, of  $\sim 10^{12}$  G, present in a NS can be dramatically amplified by several orders of magnitude after the merger. The magnetic field strength that can be reached during the first milliseconds through Kevin-Helmholtz instabilities and turbulent amplification is much higher than  $\sim 10^{15}$  G (Price & Rosswog 2006; Zrake & MacFadyen 2013; Giacomazzo et al. 2009; Obergaulinger et al. 2010). Therefore, a degree of magnetization in the ejecta could be expected in the binary NS merger. During the last decade, the observation of optical and gamma-ray polarization (e.g. see Steele et al. 2009; Mundell et al. 2007; Troja et al. 2017; Mundell et al. 2013) and the modelling of  $\gamma$ -ray, X-ray and optical bright peaks which suggests a stronger magnetic field in the reverse-shock region than in the forward-shock region (Zhang et al. 2003; Kobayashi & Zhang 2003; Kobayashi 2000; Kobayashi et al. 2007; Fraija 2015; Fraija et al. 2016b, 2012, 2017a) have provided overwhelming evidence that some IGRB progenitors are endowed of intense magnetic fields (see e.g. Usov 1992, and references therein). In the context of sGRBs,

†nifraja@astro.unam.mx

Fraija et al. (2016b) proposed that the bright peak exhibited at the prompt/early-afterglow phase could be correlated with the degree of magnetization present in the jet. In particular, the bright peak presented in the large area telescope (LAT) light curve and interpreted in the reverse-shock context indicated a compelling evidence that the central engine in GRB 090510 was magnetized, being the magnetic field amplification in the binary NS merger the most promising candidate.

On the other hand, the transition between the prompt emission and the afterglow is one of the most interesting and least understood phases. The prompt decay phase is attributed to emission from regions located at high latitudes, i.e. from regions located at viewing angles ( $\theta_{\text{obs}}$ ) larger by at least a factor  $\theta_j \sim \frac{1}{r}$  with respect to the line of sight (the curvature effect or high-latitude emission). When this effect is present, after the gamma-ray emission from the observer's line of sight has ceased, the off-axis flux at  $\theta_{\text{obs}} > \theta_j$  is dramatically suppressed unless the burst is very luminous or viewed from near its edge. Because of the curvature effect, the onset of the afterglow could be overlapped with the high-latitude emission. Radiation generated at the reverse shock would decay fast due to the angular time delay effect (Kumar & Panaiteescu 2000). Once the quickly decaying high-latitude emission is small enough the afterglow emission can be observed (Dermer et al. 2000; Granot et al. 2002; Rees 1999). GRB 170817A, the electromagnetic counterpart of the gravitational-wave transient associated with a NS-NS coalescence (GW170817; Abbott et al. 2017a,b), was detected by the Gamma-ray Burst Monitor (GBM) onboard Fermi Gamma-ray Space Telescope at 12:41:06 UTC, 2017 August 17 (Goldstein et al. 2017). Promptly, this burst was monitored in several electromagnetic bands by multiple ground-based telescopes and satellites (see e.g. Abbott et al. 2017b, and references therein). By considering the low luminosity observed in GRB 170817A the  $\gamma$ -ray flux has been associated to different emission mechanisms (Gottlieb et al. 2017; Bromberg et al. 2017; Kisaka et al. 2017; Fraija & Veres 2018; Kathirgamaraju et al. 2017, 2018) and the X-ray, optical and radio afterglow with synchrotron forward-shock models when the relativistic jet viewed off-axis and/or cocoon are decelerated in an homogeneous low density medium  $\sim 10^{-5} - 10^{-2} \text{ cm}^{-3}$  (Murguia-Berthier et al. 2017; Ioka & Nakamura 2017; Mooley et al. 2017; Lazzati et al. 2017c; Granot et al. 2017; Alexander et al. 2017; Margutti et al. 2017b; Kasliwal et al. 2017; Piro & Kollmeier 2017; Wang & Huang 2018; Guidorzi et al. 2017; Granot et al. 2017). In this paper, we present a comprehensive analysis and description of the short GRB 170817A, in the context of an off-axis jet, when the matter in the outflow is parametrized through a power law velocity distribution. The paper is arranged as follows: In Section 2, a brief description of the multiwavelength observations and GBM data reduction is presented. In Section 3, we model the non-thermal multiwavelength observations in GRB 170817A and discuss the implications on the ejecta magnetization and conclusions are given in Section 4.

## 2. GRB 170817A

### 2.1. Multiwavelength upper limits and observations

GRB 170817A was detected by the GBM-Fermi Telescope at 12:41:06 UTC, 2017 August 17 (von Kienlin et al. 2017; Goldstein et al. 2017). This detection was consistent with a gravitational-wave transient observed by LIGO and Virgo observatories. This observational transient was associated with a NS-NS coalescence with merger time 12:41:04 UTC  $\sim 2$  s before the GBM trigger (Abbott et al. 2017a,b). Immediately afterwards, an exhaustive multiwavelength campaign was launched in order to look for an isotropic electromagnetic counterpart in the optical and infrared bands (see e.g. Coulter et al. 2017, and references therein). A bright transient in the optical i-band with magnitude  $m_i = 17.057 \pm 0.008$  was observed by the 1-meter Swope telescope at Las Campanas Observatory in Chile at 10.87 hours (August 17 at 23:33 UTC) after the GMB trigger and afterward during the following 12 hours by multiple ground-based and orbiting optical/IR telescopes. In addition, linear polarization in optical bands was reported, revealing the geometry of the emitting region. This transient was located coming from the center of the galaxy NGC 4993 at a distance of 40 Mpc. Distinct X-ray observations were carried out by several orbiting satellites during the following 8 days without any detection but providing constraining limits (i.e. see Margutti et al. 2017b). From the 9th up to 256th day after the merger, X-ray detections have been reported by Chandra and XMM-Newton observatories (Troja et al. 2017; Margutti et al. 2018; Alexander et al. 2018; D'Avanzo et al. 2018). Optical observations and upper limits collected with the Advanced Camera for Surveys Wide Field Camera aboard on the Hubble Satellite Telescope (HST), have been performed since  $\sim 100$  days after the trigger (Lyman et al. 2018; Margutti et al. 2018; Alexander et al. 2018). On the sixteenth day after the post-trigger and for more than seven months, the radio counterpart at 3 and 6 GHz was obtained by Very Large Array (VLA; Abbott et al. 2017b; Mooley et al. 2017; Dobie et al. 2018; Hallinan et al. 2017).

### 2.2. GBM data reduction

Event data files were obtained using the GBM trigger time for GRB 170817A 04:47:43 UT on 2017 August 17 (von Kienlin et al. 2017; Ackermann et al. 2013). Fermi-GBM data in the energy range of 10 - 1000 keV were reduced using the public database at the Fermi Website<sup>1</sup> and the position of this burst is found to be at the coordinates (J2000) RA =  $176^\circ.8$ , DEC =  $-39^\circ.8$ , with an error circle of radius  $11.6^\circ$ . No other sources in the LAT catalog or background emission are considered due to the duration of the event.

Flux values are derived using the spectral analysis package RMfit, version 432<sup>2</sup>. To analyze the signal we use the time-tagged event (TTE) files of the three triggered NaI detectors n<sub>1</sub>, n<sub>2</sub> and n<sub>5</sub>. Different spectral models are used to fit the spectrum over different duration periods. Each time bin is chosen adopting a trade-off between the minimum signal needed to derive a spectrum and the minimum resolution required to preserve the shape of the time evolution. The Comptonized (a power law with exponential cutoff, hereafter referred as CPL) and the simple power-law (PL) functions are

<sup>1</sup> <http://fermi.gsfc.nasa.gov/ssc/data>

<sup>2</sup> <https://fermi.gsfc.nasa.gov/ssc/data/analysis/rmfit/>

used to fit the spectrum up to 0.448 s around the GBM trigger time. The spectral analysis during the time interval [-0.320 s, 0.448 s] after the trigger is reported in Table 1. This table shows the time interval (column one), spectral model (column 2), spectral index (column three), energy peak (column four), temperature of black body (BB) function and the C-Stat/dof test (last column). After the 0.512 s the spectrum fits better using a BB model.

### 3. DESCRIPTION OF THE NON-THERMAL MULTIWAVELENGTH OBSERVATIONS IN GRB 170817A

#### 3.1. Modeling the $\gamma$ -ray flux

##### 3.1.1. Light curve analysis and description

Figure 1 shows the GBM light curve and upper limits in the energy range of 10 - 1000 keV, although no significant flux was observed above 300 keV. The CPL function showed a cutoff energy of 185 keV and the corresponding isotropic energy obtained was  $E_{\gamma,\text{iso}} \simeq 5 \times 10^{46}$  erg, with  $T_{90} = 2$  s (von Kienlin et al. 2017). The GBM light curve exhibited a peak around  $\sim 1.7$  s after the gravitational-wave trigger, followed by a fast decay. The Chi-square ( $\chi^2$ ) minimization method, developed in the ROOT software package (Brun & Rademakers 1997), was used in order to fit the GBM light curve with the function:  $F_\nu(t) \propto \left(\frac{t-t_0}{t_0}\right)^{-\alpha_\gamma} e^{-\frac{\tau}{t-t_0}}$  (Vestrand et al. 2006) where  $t_0$  is the starting time,  $\tau$  is the timescale of the flux rise and  $\alpha_\gamma$  the power index of fast decay. The best-fit values of parameters are reported in Table 2.

We derive the spectral parameters of GBM data for different time intervals, as shown in Table 1. Two different time intervals, starting from -0.320 s, were used to fit with a CPL function. The best-fit value of the spectral index for the interval [-0.320 s, 0.256 s] was  $-0.955 \pm 0.309$ . The remaining time interval was divided in two and analyzed with a PL function. For the interval [0.256 s, 0.320 s] a spectral index of  $-1.749 \pm 0.434$  was obtained and for interval [0.320 s, 0.448 s] the corresponding spectral index was  $-2.150 \pm 0.472$ . The spectral fit parameters associated with the  $\gamma$ -ray peak reveal a hard-to-soft spectral evolution.

Veres et al. (2018) analyzed, in the GBM data, the evolution of the peak energy with a CPL model. Using a simple PL  $E_{\text{peak}} \propto (t - t_{\text{shift}})^{-q}$  to model the decay phase, they obtained the best-fit value of  $q = 0.97 \pm 0.35$  for  $t_{\text{shift}} = -0.15 \pm 0.04$  s.

Based on the best-fit values obtained from the analysis of the GBM data and reported in Tables 1 and 2, we discuss the origin of the  $\gamma$ -ray light curve in terms of internal and external shocks.

*1. The  $\gamma$ -ray peak  $\delta t_{\text{var}}/T_{90} \simeq 1$  does not show strong variability which disfavors the internal shock model.*— The principal motivation for evoking internal shocks is related to the observation of variable  $\gamma$ -ray light curves. In the framework of internal collisions more than one  $\gamma$ -ray peak is expected, with a variability timescale much shorter than the duration of the main activity  $\delta t_{\text{var}}/t \ll 1$  (Kobayashi et al. 1997; Rees & Meszaros 1994; Burrows et al. 2005). The properties of several light curves exhibiting one single peak without variability have been explained in the framework

of forward/reverse shocks and high-latitude emission (i.e. GRB970508, GRB021211, GRB050406 and others; Kumar & Panaiteescu 2003; McMahon et al. 2004, 2006; Nakar & Piran 2004; Kobayashi et al. 2007; Peng et al. 2009; Lu et al. 2010). In the case of the short-lived reverse shock, it can generate a  $\gamma$ -ray, X-ray or optical peak with  $\delta t_{\text{var}}/t \simeq 1$  depending on microphysical parameters and the circumburst density (Kobayashi et al. 2007; Fraija et al. 2016a). Therefore, the emission generated by the reverse shock could in principle describe naturally the variability timescale of the  $\gamma$ -ray light curve.

*2. The value of temporal index  $\alpha_\gamma = 2.85 \pm 0.35$  observed during the peak decay phase is consistent with the high-latitude afterglow emission.*— The most adopted interpretation to account for the peak decay phase in optical, X-ray and  $\gamma$ -ray bands, is attributed to delayed photons arriving from high latitudes (curvature effect). Kumar & Panaiteescu (2000) showed that the evolution of the observed flux, when it is originated at high latitudes, is  $F_{\text{obs}} \propto t^{\beta-2}$ . The values of the spectral index,  $\beta$ , correspond to the low  $-\frac{1}{2}$  ( $-\frac{1-p}{2}$ ) and high-energy  $-\frac{p}{2}$  ( $-\frac{p}{2}$ ) photon indexes of the synchrotron self-Compton (SSC)/synchrotron spectrum in the fast (slow) cooling regime. Taking into consideration the typical values of the spectral power index for external shocks,  $2.2 \leq p \leq 2.6$  (e.g., see; Kumar & Zhang 2015), the high-latitude afterglow flux is expected to evolve as  $F_\nu \propto t^{-\alpha}$  with  $2.5 \leq \alpha \leq 3.2$  which is in accordance with the value obtained of peak decay index  $\alpha_\gamma = 2.85 \pm 0.35$ . Similar results have been found in a large determined group of GRBs when the peak has been modelled through SSC/synchrotron reverse-shock emission at high latitudes (i.e, see O'Brien et al. 2006; Kobayashi et al. 2007; Fraija et al. 2016b; Zhang et al. 2006; Zhang & Kobayashi 2005; Zhang et al. 2003; Kobayashi & Zhang 2003; Fraija et al. 2017b,a). On the other hand, based on observations the typical values of decay index phase associated to internal shocks are  $5 \lesssim \alpha \lesssim 7$  (Zhang et al. 2006; Mészáros 2006; Kumar & Zhang 2015; Fan & Wei 2005) which decays faster than that observed in this burst.

*3. The evolution of peak energy at hundreds of keVs during the decay phase  $q = 0.97 \pm 0.35$  (Veres et al. 2018) is consistent with the SSC energy break of the reverse shock from high latitudes.*— Several authors have studied the spectral evolution of distinct pulses during  $\gamma$ -ray prompt emission. By analyzing the peak decay phase during the prompt emission, some bursts have provided evidence of the synchrotron emission in the fast- and slow-cooling regime from external shocks (Giblin et al. 1999; Zhang et al. 2003; Panaiteescu 2007; Fraija et al. 2017a,b). When SSC/synchrotron spectral breaks are observed coming from high latitudes/off-axis ( $\epsilon^{\text{i},\text{off}}$  for syn or SSC), Ioka & Nakamura (2017) proposed that these spectral breaks must be re-scaled as  $\epsilon^{\text{i},\text{off}} \propto \Gamma^{-2} \epsilon^{\text{i},\text{on}}$  with  $\Gamma$  the bulk Lorentz factor and  $\epsilon^{\text{syn},\text{on}}$  the energy break viewed in an on-axis outflow. Following Kobayashi (2000), Fraija et al. (2016b) and Sari et al. (1998), we re-scale the quantities associated to the internal and external shocks.  
i) Internal shocks: Given the bulk Lorentz factor in the coasting phase  $\Gamma \propto t^0$  and the magnetic field in the freezing regime  $B \propto t^0$ , the synchrotron emission evolves as  $\epsilon_{\text{pk}}^{\text{syn},\text{off}} \propto \Gamma^{-2} (\Gamma \gamma_e^2 B) \propto B^{-3} \Gamma^{-3} t^{-2} \propto t^{-2}$  (Derishev 2007). We consider a “typical” electron Lorentz factor as one

that has the average of the electron distribution  $\langle \gamma_e \rangle = \frac{U_e}{m_e N_e}$  (Piran 1999). These quantities can be calculated using two different ways: 1. The energy density given to accelerate electrons is  $U_e = \epsilon_e U = \epsilon_e \gamma_{sh} N_p m_p$  and the electron number density can be estimated as  $N_e \simeq N_p$  (Piran 1999). In this case, the average electron Lorentz factor becomes  $\langle \gamma_e \rangle = \frac{m_p}{m_e} \epsilon_e \gamma_{sh}$ . 2. The energy density given to accelerate electrons is  $U_e = \frac{m_e A_e}{(p-2)} \gamma_{e,mi}^{-p+2}$  and the electron number density can be estimated as  $N_e = \frac{m_e A_e}{(p-1)} \gamma_{e,mi}^{-p+1}$  for  $p > 2$  and  $\gamma_{e,mi} \ll \gamma_{e,max}$ . Therefore, in this case  $\langle \gamma_e \rangle = \frac{p-1}{p-2} \gamma_{e,mi}$ . Here,  $\gamma_{mi}$  and  $\gamma_{ma}$  are the minimum and maximum electron Lorentz factors, respectively, and  $\gamma_{sh}$  is the relative Lorentz factor across the internal shock (Piran 1999). Considering both cases and the magnetic field given by  $B \simeq \sqrt{\gamma_{sh}} \epsilon_B^{1/2} \Gamma^{-3} L_j^{1/2} t_\nu^{-1}$ , the electrons accelerated and cooled down in internal shocks via synchrotron radiation reach a peak energy at (e.g. see Frajia et al. 2017a)

$$\epsilon_{pk}^{\text{syn, on}} \simeq \begin{cases} 0.4 \text{ MeV } \varepsilon_{e,-0.3}^2 \gamma_{sh}^2 \\ 0.6 \text{ MeV } \gamma_{mi,3}^2 \end{cases} \times \left( \frac{1.01}{1+z} \right) \sqrt{\gamma_{sh}} \epsilon_B^{1/2} \delta t_{\text{var},0}^{-1} \Gamma_3^{-2} L_{j,49}^{1/2}. \quad (1)$$

The microphysical parameters  $\varepsilon_e$  and  $\varepsilon_B$  are the fractions of energy given to accelerate electrons and generate/amplify the magnetic field, respectively, and  $L_j$  is the jet luminosity. Hereafter, the convention  $Q_x = Q/10^x$  in c.g.s. units is adopted. Including pair formation, an upper limit for the peak energy can be estimated as (Guetta et al. 2001)

$$\epsilon_{pk}^{\text{syn, on}} \lesssim 3.3 \text{ MeV} \left( \frac{1+z}{1.01} \right)^{-1} L_{j,49}^{-1/5} \Gamma_3^{\frac{3}{5}} t_{\nu,0}^{\frac{1}{6}} \varepsilon_{B,-1}^{\frac{1}{2}} \varepsilon_{e,-0.3}^{\frac{4}{3}}. \quad (2)$$

The peak energy observed from high latitudes/off-axis jet has to be rescaled by  $\epsilon_{pk}^{\text{off}} \simeq b^{-1} \epsilon_{pk}^{\text{syn, on}}$  with  $b = 1 + \Gamma^2 \Delta \theta^2$  and  $\Delta \theta = \theta_{\text{obs}} - \theta_j$ . In this case, the observed energy  $\epsilon_{pk}^{\text{syn, off}} \simeq 10 \text{ eV} \Gamma_3^{-2} \Delta \theta_{15^\circ}^{-2}$  indicates that it can hardly reach values as high as hundreds of keVs. Therefore, the standard internal shocks cannot straightforwardly explain the evolution with time of peak energy at hundreds of keVs.

ii) Forward shock: Given the evolution of the magnetic field  $B \propto t^{-3/8}$ , the bulk Lorentz factor  $\Gamma \propto t^{-3/8}$ , the minimum and cooling electron Lorentz factors  $\gamma_{m,f} \propto t^{-3/8}$  and  $\gamma_{c,f} \propto t^{1/8}$  (Sari et al. 1998), respectively, the synchrotron spectral breaks evolve as  $\epsilon_{m,f}^{\text{syn, off}} \propto B \Gamma^{-3} \gamma_{em,f} \propto t^{-3/4}$  and  $\epsilon_{c,f}^{\text{syn, off}} \propto B^{-5} \Gamma^{-3} t^{-2} \propto t^{1/4}$ . The SSC spectral breaks evolve as  $\epsilon_{m,f}^{\text{ssc, off}} \propto \gamma_{m,f}^2 \epsilon_{m,f}^{\text{syn, off}} \propto t^{-3/2}$  and  $\epsilon_{c,f}^{\text{ssc, off}} \propto \gamma_{c,f}^2 \epsilon_{c,f}^{\text{syn, off}} \propto t^{1/2}$ . The subindex “f” indicates the forward shock.

The synchrotron spectral break  $\epsilon_{m,f}^{\text{syn, off}} \propto t^{-3/4}$  is the only spectral break that agrees with the peak energy evolution. The synchrotron spectral break is given by

$$\epsilon_{m,f}^{\text{syn, off}} \simeq 0.3 \text{ keV} \left( \frac{1+z}{1.01} \right)^{\frac{1}{2}} \varepsilon_{e,-0.3}^2 \varepsilon_{B,f,-1}^{\frac{1}{2}} E_{51}^{\frac{1}{2}} \Gamma_{2.5}^{-2} \Delta \theta_{10^\circ}^{-2} \times t_0^{-\frac{3}{2}},$$

where  $E = E_{\gamma,\text{iso}}/\eta$  is the isotropic equivalent kinetic energy with  $\eta$  the kinetic efficiency. It shows that although

synchrotron spectral break ( $\epsilon_{m,f}^{\text{syn, off}}$ ) agrees with the peak energy evolution, it cannot reach the values of energies at hundreds of keVs.

iii) Reverse shock in the thick- (thin-) shell case: Given the evolution of the magnetic field  $B \propto t^{-1/4}(t^0)$ , the bulk Lorentz factor  $\Gamma \propto t^{-1/4}(t^0)$ , the minimum and cooling electron Lorentz factors  $\gamma_{m,r} \propto t^{1/4}(t^3)$  and  $\gamma_{c,r} \propto t^{-1/4}(t^{-1})$  (Kobayashi 2000), respectively, before the crossing time, the synchrotron spectral breaks evolve as  $\epsilon_{m,r}^{\text{syn, off}} \propto t^{1/2}(t^6)$  and  $\epsilon_{c,r}^{\text{syn, off}} \propto t^{-1/2}(t^{-2})$ . The SSC spectral breaks evolve as  $\epsilon_{m,r}^{\text{ssc, off}} \propto t(t^{12})$  and  $\epsilon_{c,r}^{\text{ssc, off}} \propto t^{-1}(t^{-4})$ . Taking into account that the quantities after the crossing time vary as  $B \propto t^{-13/24}(t^{-4/7})$ ,  $\Gamma \propto t^{-7/16}(t^{-2/5})$ ,  $\gamma_{m,r} \propto t^{-13/48}(t^{-2/7})$  and  $\gamma_{c,r} \propto t^{25/48}(t^{19/35})$ , the synchrotron spectral breaks evolve as  $\epsilon_{m,r}^{\text{syn, off}} \propto t^{-0.65}(t^{-0.74})$  and  $\epsilon_{m,r}^{\text{syn, off}} \propto t^{0.94}(t^{0.91})$ . The SSC spectral breaks evolve as  $\epsilon_{m,r}^{\text{ssc, off}} \propto t^{-1.18}(t^{-1.31})$  and  $\epsilon_{c,r}^{\text{ssc, off}} \propto t^{1.98}(t^{1.99})$ . The subindex “r” indicates the reverse shock.

The SSC and synchrotron spectral breaks that agree with the peak energy evolution are  $\epsilon_{m,r}^{\text{syn, off}} \propto t^{-0.65}(t^{-0.74})$  and  $\epsilon_{m,r}^{\text{ssc, off}} \propto t^{-1.18}(t^{-1.31})$ , respectively. The SSC and synchrotron spectral breaks are given by (Kobayashi 2000; Frajia et al. 2016b)

$$\begin{aligned} \epsilon_{m,r}^{\text{syn, on}} &\simeq 16.2 \text{ eV} \left( \frac{1+z}{1.01} \right)^{-1} \varepsilon_{e,-0.3}^2 \varepsilon_{B,r,-1}^{\frac{1}{2}} \Gamma_{2.8}^2 n_0^{\frac{1}{2}}, \\ \epsilon_{m,r}^{\text{ssc, on}} &\simeq 13.4 \text{ MeV} \left( \frac{1+z}{1.01} \right)^{-\frac{7}{4}} \varepsilon_{e,-0.3}^4 \varepsilon_{B,r,-1}^{\frac{1}{2}} \Gamma_{2.8}^4 n_0^{\frac{3}{2}} E_{51}^{-\frac{1}{4}} \\ &\quad \times r_{cr,0}^{\frac{3}{4}}, \end{aligned}$$

which have to be rescaled again by  $(1 + \Gamma^2 \Delta \theta^2)^{-1}$  (Ioka & Nakamura 2017). The term  $r_{cr}$  is the shock crossing time. The parameter  $n$  corresponds to the circumburst density. For this analysis, the bulk Lorentz factor corresponds to that one associated with the reverse shock. This value can be estimated taking into consideration the four-region structure during the shock: (1) the unshocked ISM with density  $n_1$ , (2) the shocked ISM, (3) the shocked shell material and (4) the unshocked shell material with density  $n_4$  and the equations governing the shocks with the jump conditions  $\frac{n_4}{n_1} \simeq \frac{(\gamma_3 - 1)(4\gamma_3 + 3)}{(\gamma_{34} - 1)(4\gamma_{34} + 3)}$  and  $\gamma_{34} \simeq \frac{1}{2} \left( \frac{\gamma_4}{\gamma_3} + \frac{\gamma_3}{\gamma_4} \right)$  (Blandford & McKee 1976; Sari & Piran 1995), with  $\gamma_{34}$  the relative Lorentz factor between the upstream and downstream region,  $\gamma_3 \equiv \Gamma_r$  and  $\gamma_4 \equiv \Gamma$  the reverse and initial Lorentz factors, respectively (Kobayashi 2000). For the relativistic case, i.e.,  $\gamma_{34} \gg 1$ , the bulk Lorentz factor of the reverse shock is

$$\Gamma_r \simeq \sqrt{\frac{\Gamma}{2}} \left( \frac{n_4}{n_1} \right)^{1/4}. \quad (3)$$

For typical values of the initial bulk Lorentz factor  $300 \leq \Gamma \leq 600$  and densities of unshocked ISM and shell  $n_4 \simeq n_1$ , the bulk Lorentz factor becomes  $12.3 \leq \Gamma_r \leq 17.3$ . For the case of  $\Gamma_r = 15$ , SSC and synchrotron spectral breaks have to be rescaled by  $\approx 7 \times 10^{-2} \Gamma_{r,1.2}^{-2} \Delta \theta_{15^\circ}^{-2}$ . Therefore, the characteristic break of SSC reverse-shock emission agrees with the evolution of peak energy at hundreds of keVs during the decay phase.

4. *The hard-to-soft spectral-index evolution (from  $-1.749 \pm 0.434$  to  $-2.150 \pm 0.472$ ) seems to be consistent with SSC/synchrotron spectrum originated in external shocks.*— Ultra-relativistic electrons confined in a magnetic field are cooled down by synchrotron and SSC radiation. The high and low spectral indexes in the fast(slow)-cooling regime are  $-\frac{1}{2}(-\frac{p-1}{2})$  and  $-\frac{p}{2}(-\frac{p}{2})$ , respectively. Given the typical values of the spectral power index for external shocks,  $2.2 \leq p \leq 2.6$  (e.g., see; Kumar & Zhang 2015), the SSC/synchrotron spectrum  $\nu F_\nu \propto \nu^{-(\beta+1)}$  with  $1.5(1.6) \leq \beta + 1 \leq 2.3(2.3)$  agrees with the spectral-index evolution for fast(slow)-cooling regime.

The previous analysis, performed on the temporal and spectral features of the  $\gamma$ -ray light curve (see Figure 1 and Tables 1 and 2), illustrates that: i) The characteristic break of SSC reverse shock agrees with the evolution of peak energy at hundreds of keVs during the decay phase, while synchrotron emission from internal and forward shocks cannot explain this evolution, ii) The reverse-shock emission can reproduce, in a more natural way, the observed variability timescale than internal-shock emission and iii) The temporal and spectral indexes of synchrotron/SSC emission, originated from external shocks, are consistent with the spectral-index evolution and the high-latitude afterglow model. Therefore, we argue that the SSC reverse-shock emission in the fast-cooling regime reproduce the temporal and spectral features of the  $\gamma$ -ray light curve. In the following subsection the SSC spectrum in the fast cooling regime is used to describe the the  $\gamma$ -ray flux.

### 3.1.2. Theoretical model

The SSC spectral breaks and fluxes are determined by the spectral break evolution between forward and reverse shocks (Zhang & Kobayashi 2005; Fraija 2015; Fraija et al. 2016a). The SSC spectrum in the fast cooling regime is given by (Ioka & Nakamura 2017)

$$F_{\nu,r}^{\text{ssc, on}} = F_{\max,r}^{\text{ssc, on}} \left( \frac{\epsilon_\gamma}{\epsilon_{c,r}^{\text{ssc, on}}} \right)^{-\frac{1}{2}} \quad \text{for } \epsilon_{c,r}^{\text{ssc, on}} < \epsilon_\gamma < \epsilon_{m,r}^{\text{ssc, on}}, \quad (4)$$

and once the characteristic break energy passes through the  $\gamma$ -ray band  $\epsilon_\gamma \approx 100$  keV at  $\sim t_{\text{cr}}^{\text{ssc, on}} / \epsilon_\gamma$ , the SSC flux begins evolving in the following power-law segment of the light curve  $F_{\max,r}^{\text{ssc, on}} \left( \frac{\epsilon_{m,r}^{\text{syn, on}}}{\epsilon_{c,r}^{\text{syn, on}}} \right)^{-\frac{1}{2}} \left( \frac{\epsilon_\gamma}{\epsilon_{m,r}^{\text{syn, on}}} \right)^{-\frac{p}{2}}$  for  $\epsilon_{c,r}^{\text{syn, on}} < \epsilon_{m,r}^{\text{syn, on}} < \epsilon_\gamma$ . The SSC energy breaks and the maximum fluxes when reverse shock evolves in the thick shell are given explicitly in Fraija et al. (2012). These quantities viewed off-axis must be corrected by

$$\epsilon_{m,c,r}^{\text{ssc, off}} = b^{-1} \epsilon_{m,c,r}^{\text{ssc, on}}, \quad \text{and} \quad F_{\max,r}^{\text{ssc, off}} = b^{-3} F_{\max,r}^{\text{ssc, on}}. \quad (5)$$

To find the best-fit values that reproduce the data with our off-axis model, we perform the Bayesian statistical method of Markov-Chain Monte Carlo (MCMC) simulations. Our model is fully described by a set of seven parameters,  $\Xi_{\text{rev}} = \{n, \bar{E}, \Delta\theta, p, \Gamma_r, \varepsilon_{B,r}, \varepsilon_e\}$ , with an extra parameter of  $\sigma$  for the likelihood of the MCMC. We generate samples of the posterior for our off-axis model using the No-U-Turn Sampler (NUTS) from the PyMC3 python distribution (Salvatier J.

2016). In order to fit data, we run the model for fluxes with a total of 14000 samples and 3000 tuning steps, which are to be discarded after tuning. The priors are assigned independently, with a mixture of different continuous probability distributions functions and standard deviations. The parameters  $p$ ,  $\Gamma_r$  and  $n$  are given normal distributions,  $\Delta\theta$  a uniform distribution and  $\varepsilon_{B,r}$ ,  $\varepsilon_e$  and  $\bar{E}$  are given modified normal distributions. Output is given by means of a Corner Plot (Foreman-Mackey 2016) on which the diagonal is a one-dimensional kernel plot of the posterior probability distribution function and the off-diagonal are the bi-dimensional kernel plots. Hereafter, the values of cosmological parameters  $H_0 = 71 \text{ km s}^{-1} \text{ Mpc}^{-1}$ ,  $\Omega_m = 0.27$ ,  $\Omega_\lambda = 0.73$  are adopted (Spergel et al. 2003).

Figure 2 shows the corner plots obtained from the MCMC simulation for each parameter using SSC reverse shock model. The best-fit values in this figure are shown in green color. The median of the posterior distributions, alongside with the symmetrical 35% quantiles, are reported in Table 3.

### 3.2. Modeling the non-thermal X-ray, optical and radio data

#### 3.2.1. Light curve analysis and description

Several X-ray observations were carried out during the following 8 days after the merger providing constraining limits (i.e. see Margutti et al. 2017b). On the ninth day, the Chandra X-ray observatory reported a faint X-ray flux from the direction of the binary NS merger (Troja et al. 2017). From the 108th to 256th day post GW trigger, Chandra and XMM-Newton observatories reported detections (Margutti et al. 2017a; Haggard et al. 2018). The Hubble Space Telescope (HST) observed optical non-thermal fluxes with magnitudes  $26.44 \pm 0.14$  mag (Lyman et al. 2018) and  $26.90 \pm 0.25$  mag (Margutti et al. 2018) at  $\sim 110$  and  $137$  days, respectively, after the merger. On 2018 March 23, HST provides an upper limit of  $> 0.070 \mu\text{Jy}$  (Alexander et al. 2018). Since the sixteenth day post-trigger and for more than seven months, Very Large Array (VLA) has reported a faint radio flux at 3 and 6 GHz (Troja et al. 2017; Hallinan et al. 2017; Mooley et al. 2017; Alexander et al. 2017).

In order to describe, firstly, the X-ray, optical and radio light curves during the increasing phase, we consider these light curves up to  $145 \pm 20$  days and the broadband SED in three separate periods: at  $15 \pm 2$ ,  $110 \pm 5$  and  $145 \pm 20$  days. The X-ray and radio (6 and 3 GHz) light curves up to  $145 \pm 20$  days were adjusted to simple power laws  $F_\nu \propto t^{-\alpha_i}$  (for  $i=\text{X, 6GHz and 3GHz}$ ) and the broadband SED at  $15 \pm 2$ ,  $110 \pm 5$  and  $145 \pm 20$  days were fitted with  $F_\nu \propto \nu^{-\beta_i}$ . The best-fit values of temporal and spectral indexes obtained with the  $\chi^2$  test implemented in the ROOT software package are reported in Table 4. Given the best-fit values obtained up to  $145 \pm 20$  days, the multiwavelength fluxes can be described as  $\propto t^{0.76 \pm 0.18} \nu^{-0.58 \pm 0.15}$  for X-ray, optical and radio data.

Afterglow emission is generated when the relativistic jet encounters the homogeneous medium and sweeps up enough circumburst material. The synchrotron forward-shock model are the most favorable one to describe the late time multiwavelength observations. Taking into account the closure relations of the standard synchrotron forward-shock model, the X-ray, optical and radio (6 and 3 GHz) fluxes are evolving in the slow-cooling regime corresponding to the

power-law segment (Sari et al. 1998)

$$F_{\nu,f}^{\text{syn,on}} = F_{\max,f}^{\text{syn,on}} \left( \frac{\epsilon_\gamma}{\epsilon_{\text{m},f}^{\text{syn,on}}} \right)^{-\frac{p-1}{2}} \quad \text{for } \epsilon_{\text{m},r}^{\text{syn}} < \epsilon_\gamma < \epsilon_{\text{c},r}^{\text{syn,on}}, \quad (6)$$

with  $p = 2\beta + 1 \approx 2.2$  and

$$\epsilon_{\text{m},f}^{\text{syn,on}} \propto t^0 \Gamma^4, \quad \epsilon_{\text{c},f}^{\text{syn,on}} \propto t^{-2} \Gamma^{-4} \quad \text{and} \quad F_{\max,f}^{\text{syn,on}} \propto E t^0 \Gamma^0. \quad (7)$$

Considering the evolution of the bulk Lorentz factor,  $\Gamma \propto t^{-\frac{3}{8}}$ , the flux varies as  $F_{\nu,f}^{\text{syn,on}} \propto t^{-\frac{3(p-1)}{4}}$ . Given the observed temporal index reported in Table 4, the value of electron distribution would be  $p \approx -0.07$  which is inconsistent with the value obtained from the broadband SED ( $p \approx 2.2$ ). While the evolution of the synchrotron flux as function of the energy is well-described, the evolution of it with time fails. This inconsistency is due to the evolution of the bulk Lorentz factor.

Given that the standard synchrotron afterglow model cannot account for the X-ray, optical and radio light curves of GRB 170817A, we consider the synchrotron forward-shock model to be off-axis when the matter in the outflow is parametrized through a power law velocity distribution.

### 3.2.2. Theoretical model

We consider that the jet concentrated within an opening angle  $\theta_j$  “top-hat jet” producing the afterglow emission is not aligned with the observer’s line of sight and the ejecta has an equivalent kinetic energy parametrized by a power law distribution as  $\tilde{E} (\beta\Gamma)^{-\alpha_s}$  where  $\tilde{E}$  is the fiducial energy,  $\alpha_s = 1.1$  for  $\beta\Gamma \gg 1$  and  $\alpha_s = 5.2$  for  $\beta\Gamma \ll 1$  for the adiabatic case (Tan et al. 2001; Sari & Mészáros 2000; Barniol Duran et al. 2015; Hotokezaka & Piran 2015; Hotokezaka et al. 2013; Kyutoku et al. 2014; Fraija & Veres 2018). Taking into account the relativistic regime ( $\beta\Gamma \gg 1$ ), we propose that the corresponding equivalent kinetic energy for  $\theta_{\text{obs}} \gtrsim 2\theta_j$  is given by

$$E_k = b^{-3} \tilde{E} \Gamma^{-\alpha_s} \simeq \Delta\theta^{-6} \Gamma^{-\delta} \tilde{E}, \quad (8)$$

for  $\Gamma^2 \Delta\theta^2 \gg 1$  with  $\Delta\theta = \theta_{\text{obs}} - \theta_j$  and  $\delta = \alpha_s + 6$ .

Considering the adiabatic evolution of the forward shock (Blandford & McKee 1976; Sari 1997), the fiducial energy is given by  $\tilde{E} = 16/17\pi \Delta\theta^6 \Gamma^{\delta+2} R^3 n m_p$  (Blandford & McKee 1976; Sari 1997) with  $m_p$  the proton mass and  $R$  the deceleration radius. In this case, the bulk Lorentz factor evolves as

$$\Gamma = 7.8 \left( \frac{1+z}{1.01} \right)^{\frac{3}{\delta+8}} n_{-4}^{-\frac{1}{\delta+8}} \tilde{E}_{51}^{\frac{1}{\delta+8}} \Delta\theta_{20^\circ}^{-\frac{6}{\delta+8}} t_{1\text{d}}^{-\frac{3}{\delta+8}}. \quad (9)$$

Replacing eqs. (9) and (8) in (7), the synchrotron spectral breaks and the maximum flux are

$$\begin{aligned} \epsilon_{\text{m},f}^{\text{syn}} &\simeq 7.7 \times 10^{-4} \text{ GHz} \left( \frac{1+z}{1.01} \right)^{\frac{4-\delta}{\delta+8}} \epsilon_{e,-1}^2 \epsilon_{B,-4}^{\frac{1}{2}} n_{-4}^{\frac{6}{2(\delta+8)}} \\ &\quad \times \tilde{E}_{51}^{\frac{4}{\delta+8}} \Delta\theta_{20^\circ}^{-\frac{24}{\delta+8}} t_{1\text{d}}^{-\frac{12}{\delta+8}} \\ \epsilon_{\text{c},f}^{\text{syn}} &\simeq 5.2 \text{ keV} \left( \frac{1+z}{1.01} \right)^{\frac{6-4}{\delta+8}} (1+x)^{-2} \epsilon_{B,-4}^{-\frac{3}{2}} n_{-4}^{-\frac{3\alpha_s+10}{2(\alpha_s+6)}} \\ &\quad \times \tilde{E}_{51}^{-\frac{4}{\delta+8}} \Delta\theta_{20^\circ}^{\frac{24}{\delta+8}} t_{100\text{ d}}^{-\frac{2\alpha_s}{\delta+8}} \end{aligned}$$

$$\begin{aligned} F_{\max,f}^{\text{syn}} &\simeq 1.4 \text{ mJy} \left( \frac{1+z}{1.01} \right)^{\frac{8-2\delta}{\delta+8}} \epsilon_{B,-4}^{\frac{1}{2}} n_{-4}^{\frac{3\delta+8}{2(\delta+8)}} D_{26.1}^{-2} \tilde{E}_{51}^{\frac{8}{\delta+8}} \\ &\quad \times \Delta\theta_{20^\circ}^{-\frac{48}{\delta+8}} t_{100\text{ d}}^{\frac{3\delta}{\delta+8}}. \end{aligned} \quad (10)$$

Given the new evolution of the synchrotron emission, from eqs. (13) and (6), the power-law segment of the synchrotron spectrum in the slow-cooling regime becomes

$$F_{\nu,\text{inc}} \simeq F_{\nu,i} t_{100\text{ d}}^{\frac{3\delta-6(p-1)}{\delta+8}} \epsilon_\gamma^{-\frac{p-1}{2}} A_{\nu,\text{inc}}, \quad (11)$$

where

$$\begin{aligned} A_{\nu,\text{inc}} &= \left( \frac{1+z}{1.01} \right)^{-\frac{7\delta+12+p\delta+4p}{2(\delta+8)}} \epsilon_{e,-1}^{p-1} \epsilon_{B,-4}^{\frac{p+1}{4}} n_{-4}^{\frac{16+6(p+5)}{4(\delta+8)}} D_{26.1}^{-2} \\ &\quad \times \tilde{E}_{51}^{\frac{6+2p}{\delta+8}} \Delta\theta_{20^\circ}^{-\frac{12(p+3)}{\delta+8}}, \end{aligned} \quad (12)$$

and  $F_{\nu,i} = \{9.8 \times 10^{-3}, 6.5 \times 10^{-3}, 1.1 \times 10^{-5}, 1.8 \times 10^{-7}\}$  mJy for  $\epsilon_\gamma = \{3 \text{ GHz}, 6 \text{ GHz}, 1 \text{ eV}, 1 \text{ keV}\}$ , respectively. For this case, the flux varies as  $F_\nu \propto t^{\frac{3\delta-6(p-1)}{\delta+8}} \nu^{-\frac{p-1}{2}}$ , which for  $\alpha_s \approx 1.1$  and  $p \approx 2.2$  it evolves as found after fitting the SED at  $15 \pm 2$ ,  $110 \pm 5$  and  $145 \pm 20$  days and reported in Table 4. It is worth noting that for  $\delta = 0$ , the flux  $F_{\nu,\text{dec}} \propto t^{-\frac{3(p-1)}{4}}$  derived in Sari et al. (1998) is recovered.

Since the radiation beaming cone broadens increasingly, it reaches our line of sight later ( $\Gamma \sim \Delta\theta^{-1}$ ; Dermer et al. 2000; Granot et al. 2002; Rees 1999; Granot et al. 2017; Sari et al. 1999). Once the flux reaches our field of view the synchrotron spectral breaks and the maximum flux become

$$\begin{aligned} \epsilon_{\text{m},f}^{\text{syn}} &\simeq 2.9 \times 10^{-4} \text{ GHz} \left( \frac{1+z}{1.01} \right)^{\frac{6-\alpha_s}{\alpha_s+6}} \epsilon_{e,-1}^2 \epsilon_{B,-4}^{\frac{1}{2}} n_{-4}^{\frac{\alpha_s-2}{2(\alpha_s+6)}} \\ &\quad \times \tilde{E}_{51}^{\frac{4}{\alpha_s+6}} t_{200\text{ d}}^{-\frac{12}{\alpha_s+6}} \\ \epsilon_{\text{c},f}^{\text{syn}} &\simeq 3.4 \text{ keV} \left( \frac{1+z}{1.01} \right)^{\frac{\alpha_s-6}{\alpha_s+6}} (1+x)^{-2} \epsilon_{B,-4}^{-\frac{3}{2}} n_{-4}^{-\frac{3\alpha_s+10}{2(\alpha_s+6)}} \\ &\quad \times \tilde{E}_{51}^{-\frac{4}{\alpha_s+6}} t_{200\text{ d}}^{-\frac{2\alpha_s}{\alpha_s+6}} \\ F_{\max,f}^{\text{syn}} &\simeq 1.1 \text{ mJy} \left( \frac{1+z}{1.01} \right)^{-\frac{4\alpha_s}{\alpha_s+6}} \epsilon_{B,-4}^{\frac{1}{2}} n_{-4}^{\frac{3\alpha_s+2}{2(\alpha_s+6)}} D_{26.1}^{-2} \tilde{E}_{51}^{\frac{8}{\alpha_s+6}} \\ &\quad \times t_{200\text{ d}}^{-\frac{3(2-\alpha_s)}{\alpha_s+6}}. \end{aligned} \quad (13)$$

Since  $\epsilon_{\text{m},f}^{\text{syn}} \leq \epsilon_\gamma \leq \epsilon_{\text{c},f}^{\text{syn}}$ , the flux lies in the same power-law segment. It begins decreasing as

$$F_{\nu,\text{dec}} \simeq F_{\nu,\text{dec}} t_{200\text{ d}}^{-\frac{3(\alpha_s-2p)}{\alpha_s+6}} \epsilon_\gamma^{-\frac{p-1}{2}} A_{\nu,\text{dec}}, \quad (14)$$

where

$$\begin{aligned} A_{\nu,\text{dec}} &= \left( \frac{1+z}{1.01} \right)^{\frac{6p-7\alpha_s-p\alpha_s-6}{2(\delta+8)}} \epsilon_{e,-1}^{p-1} \epsilon_{B,-4}^{\frac{p+1}{4}} n_{-4}^{\frac{5\alpha_s+6+\alpha_s p-2p}{4(\alpha_s+6)}} D_{26.1}^{-2} \\ &\quad \times \tilde{E}_{51}^{\frac{2(2-p)}{\alpha_s+6}} \end{aligned} \quad (15)$$

and  $F_{\nu,\text{dec}} = \{6.1 \times 10^{-3}, 4.0 \times 10^{-3}, 6.9 \times 10^{-6}, 1.1 \times 10^{-7}\}$  mJy for  $\epsilon_\gamma = \{3 \text{ GHz}, 6 \text{ GHz}, 1 \text{ eV}, 1 \text{ keV}\}$ , respectively. It is worth noting that for  $\alpha_s = 0$ , the flux  $F_{\nu,\text{dec}} \propto t^{-p}$  derived in Sari et al. (1999) is recovered.

Therefore, the flux to be used to model the X-ray, optical and radio data can be summarized as

$$F_\nu = \begin{cases} F_{\nu,\text{inc}}, & \text{if } t < t_{\text{peak}}, \\ F_{\nu,\text{dec}}, & \text{if } t > t_{\text{peak}}, \end{cases} \quad (16)$$

where

$$t_{\text{peak}} \simeq 86.6 \text{ day} k \left( \frac{1+z}{0.01} \right) n_0^{-1/3} E_{51}^{1/3} \Delta\theta_{20^\circ}^{-\frac{\alpha_s+6}{3}}, \quad (17)$$

where the parameter  $k$  differs from one model to another, and is introduced to correlate the times of peak flux and the jet break through the viewing and the opening angles (Nakar et al. 2002; Granot et al. 2002).

To find these values, we again perform the Bayesian statistical method of Markov-Chain Monte Carlo (MCMC) simulations. In this case, our model is fully described by a set of eight parameters,  $\Xi_{\text{fow}} = \{n, \tilde{E}, k, \Delta\theta, p, \alpha_s, \varepsilon_{B,f}, \varepsilon_e\}$ , with an extra parameter of  $\sigma$  for the likelihood of the MCMC. For this MCMC run, we utilised 14000 steps with 7000 tuning steps, which were discarded after tuning. The parameters  $\Delta\theta$  and  $p$  are given uniform distributions, while the remaining parameters  $n, \varepsilon_{B,f}, \varepsilon_e, k, \alpha_s$  and  $\tilde{E}$  are given normal distributions. Output is again given by means of a Corner Plot (Foreman-Mackey 2016) on which the diagonal is a one-dimensional projection of the posterior probability distribution function and the off-diagonal plots are the bi-dimensional projections. Figures 3, 4 and 5 show the corner plots for radio wavelengths (3 GHz and 6 GHz) and X-rays, respectively, obtained from the MCMC simulation for each parameter using our model (eqs. 16). The best-fit values in these figures are shown in green color. The median of the posterior distributions, alongside with the symmetrical 35% quantiles, are reported in Table 5.

### 3.3. Analysis and implications

#### 3.3.1. The magnetic microphysical parameters

Sari & Piran (1995) derived the hydrodynamic timescales of the reverse shock for a non-magnetized GRB jet. They found that in absence of magnetization, the crossing time becomes  $t_{\text{cr}} \simeq \frac{T_{90}}{2}$ . The hydrodynamic timescales of the reverse shock powered by a magnetized outflow were investigated by Fan et al. (2004), Zhang & Kobayashi (2005) and Mimica et al. (2009, 2010). Authors reported that general characteristics in the reverse shock vary according to the degree of magnetization in the jet. For instance, when the jet was moderately magnetized with a magnetization parameter in the range of  $0.1 \lesssim \sigma \lesssim 1$ , then the magnetic microphysical parameter would vary between  $0.1 \lesssim \varepsilon_{B,r} \lesssim 0.2$  and the width of the peak generated by the reverse shock becomes narrower and more prominent, between  $\frac{T_{90}}{2} \lesssim t_{\text{cr}} \lesssim \frac{T_{90}}{5}$ . This result agrees with the value of the magnetic microphysical parameter found after describing the GBM data and the duration of the bright peak ( $\sim 0.4$  s) observed in the GBM light curve. If the relativistic jet would have had high magnetization ( $\sigma \gg 1$ ) when it crosses the reverse shock, relativistic particles would be poorly accelerated and the emission drastically decreased (Sironi & Spitkovsky 2011; Zhang & Kobayashi 2005). Therefore, a moderate magnetization ( $\sigma \lesssim 1$ ) is required in order to interpret the GBM bright peak in the reverse shock framework (Zhang et al. 2003; Kumar & Panaiteescu 2003; Fan et al. 2004). The values of the magnetic microphysical parameters (see Tables 3 and 5) indicate that the magnetic field ratio in the forward- and reverse-shock region is  $\sim 40$ . Similarly, the values found also illustrate that synchrotron flux is  $\sim 2.5 \times 10^3$  times stronger in the reverse than the forward shock, so there are much more photons available to be scattered via inverse Compton in the reverse shock. It suggests that the outflow

carried a significant magnetic field as reported in sGRB 090510 (Frajia et al. 2016b).

Taking into consideration the typical initial value of the fireball radius ( $r_i \sim 10^{6.5}$  cm; Lee et al. (2004, 2005); Nakar (2007)), the kinetic equivalent energy and the magnetic microphysical parameter (see Table 3), the magnetic field at the base of the jet is roughly estimated as  $B \approx \sqrt{8\varepsilon_{B,i} E_{\gamma,iso}/r_i^3} \approx 10^{15}$  G. The strength of the magnetic field is three-four orders of magnitude higher than usual strength in a NS  $\sim 10^{12}$  G. Here,  $\varepsilon_{B,i} \approx \varepsilon_{B,r}$  is the initial fraction of total energy given to magnetic field. It shows that GRB 170817A demands more magnetic fields at the base of the jet, thus indicating that the progenitor is entrained with strong magnetic fields.

Just et al. (2016) laid out relativistic and axisymmetric hydrodynamic simulations of black hole-torus system as remnants of a binary NS merger. They showed that thermal energy via annihilation of neutrinos and antineutrinos abundantly emitted by the hot accretion disk is not long and strong enough for the outflows to break out from the neutrino wind, thus concluding that the neutrino annihilation alone could not power sGRBs from binary NS mergers. Therefore, the energy requirements favor magnetic fields as the responsible mechanism so that the outflow breaks out. Some authors have presented simulations based on general relativistic magnetohydrodynamics to follow the evolution of the magnetic fields in the binary NS merger (Price & Rosswog 2006; Zrake & MacFadyen 2013; Ciolfi et al. 2017). All models proposed show an amplification of magnetic field up to three orders of magnitude or more. The rapid growth of this field is attributed to the Kelvin-Helmholtz instabilities and turbulent and/or differential rotation. Therefore, the most natural process associated with the magnetization of outflow is the magnetic field amplification during the binary NS merger which is entrained by outflow.

#### 3.3.2. Other parameters

1. The values of the external medium densities required to model the  $\gamma$ -ray GBM data  $\sim 1.7$  s after the merger (see Table 3) and the X-ray, optical and radio data (see Table 5) are quite different, indicating that the  $\gamma$ -ray emission and the afterglow occurred in different regions. It suggests that the external density distribution could be stratified as proposed in sGRBs (Parsons et al. 2009). Binary NS mergers are thought to be potential candidates to eject significant masses with distinct velocities and densities. The ejected masses with densities larger than low ISM are ejected at sub-relativistic velocities. In principle, the ultra-relativistic jet coming out from the progenitor could interact with these dense material producing an afterglow (Hotokezaka & Piran 2015; Hotokezaka et al. 2013; Kyutoku et al. 2014; Tan et al. 2001; Frajia & Veres 2018). Moreover, fits to the multiwavelength afterglow have been suggested that the circumburst medium close to the progenitor could be dense and be formed by gaseous environments rather than the low ISM (Berger 2007; Nyswander et al. 2009; Panaiteescu 2006; Nakar 2007; Parsons et al. 2009). The low value of the ISM would confirm that sGRBs explode in lower-density environments.
2. The values of the electron spectral indexes for the  $\gamma$ -ray flux and the X-ray, optical and radio fluxes are equal. These spectral indexes correspond to the typi-

cal values reported in external shocks  $2.2 \leq p \leq 2.6$  (e.g., see; Kumar & Zhang 2015). It suggests that the GBM  $\gamma$ -ray flux could have been originated in external shocks. Similar results have been found in several bursts that have exhibited early sub-GeV  $\gamma$ -ray and optical peaks together with temporarily extended multiwavelength emissions (Kobayashi & Zhang 2007; Kobayashi et al. 2007; Frajia 2015; Frajia et al. 2016a, 2017b).

3. Two scenarios are discussed in order to explain GRB 170817A (e.g., Murguia-Berthier et al. 2017): a low-luminosity sGRB and a typical sGRB viewed off-axis. Whereas a low-luminosity sGRB could be produced by a mildly relativistic outflow (Rosswog & Ramirez-Ruiz 2003, 2002; Nagakura et al. 2014), a typical sGRB is generated by a relativistic jet (Ramirez-Ruiz et al. 2005; Murguia-Berthier et al. 2014). In both cases a relativistic jet is invoked, however in the first case the jet is choked by the wind expelled from the hyper massive neutron star (HMNS), thus giving rise to a low-luminosity sGRB with  $E_{\gamma,\text{iso}} \simeq 10^{46} - 10^{47}$  erg. Considering the values of the equivalent energy we estimate for this event (see Tables 3 and 5), we suggest that the most likely scenario for GRB 170817A is that of a jet that successfully breaks out from the wind and it is viewed off-axis. This result agrees with the recent work by Mooley et al. (2018), where authors present Very Long Baseline Interferometry (VLBI) observations that show superluminal motion and support the successful breakout of the jet.
4. The collimation of ejecta has relevant implications in GRBs. For instance, the energy scale, the energy extraction mechanism and the event rate. For sGRBs, there are only a few observations of jet breaks despite serious effort. Based on the breaks detected in the afterglow emission, Berger (2014) showed a distribution of jet opening angles for sGRBs with a mean around  $\theta_j \sim (5^\circ)$ . Recently, a similar value of opening angle was obtained after modeling the afterglow in GRB 170817A (i.e. see; Troja et al. 2018; Granot et al. 2017). Taking into account the value of  $\theta_j = 5^\circ$ , the viewing angle for GRB 170817A would be  $\theta_{\text{obs}} = 20^\circ$ , which is in the range reported for this burst (Margutti et al. 2017b; Granot et al. 2017; Margutti et al. 2018; Troja et al. 2018; Mooley et al. 2018).
5. Considering the values reported together with eqs. (8) and (9), the bulk Lorentz factor is  $\Gamma \simeq 8.7$  and the equivalent kinetic energy is  $E_k \simeq 3.3 \times 10^{47}$  erg. Comparing with the observed isotropic energy  $E_{\gamma,\text{iso}} \simeq 5 \times 10^{46}$  erg, the corresponding efficiency becomes  $\eta \simeq 15\%$ , which lies in the typical range reported for afterglows (e.g. see; Kumar & Zhang 2015).

#### 4. CONCLUSIONS

We have analyzed the non-thermal ( $\gamma$ -ray, X-ray, optical and radio) observations of GRB 170817A/GW170817. The X-ray, optical and radio data were consistent with the synchrotron forward-shock model when the jet is viewed off-axis and the matter in the outflow is parametrized through a power law velocity distribution. The origin of the  $\gamma$ -ray peak was discussed in terms of internal and external shocks. The analysis performed favors to a SSC reverse-shock model in the

fast-cooling regime observed at high latitudes. The fit of the  $\gamma$ -ray GBM data with SSC model suggests that:

- The circumburst medium close to the progenitor is much denser than the low ISM obtained after modeling the X-ray, optical and radio data. One possible explanation suggests that the external density distribution could be stratified as proposed in sGRBs (Parsons et al. 2009; Hotokezaka & Piran 2015; Hotokezaka et al. 2013; Kyutoku et al. 2014; Tan et al. 2001; Frajia & Veres 2018); the circumburst medium close to the progenitor could be formed by gaseous environments and/or dense ejected masses rather than a very low density medium of the host galaxy. It suggests that the afterglow and  $\gamma$ -ray emission occurred in different regions.
- The value of the electron spectral index illustrates that this component could have been originated at the external shocks. Similar discussions have been previously reported around the temporarily extended Fermi-LAT components (Kobayashi & Zhang 2007; Kobayashi et al. 2007; Frajia 2015; Frajia et al. 2016a, 2017b).
- The value of the magnetic microphysical parameter obtained agrees with the temporal properties exhibited by this burst and also indicates that the strength of the magnetic field is three-four orders of magnitude higher than usual strength in a NS  $\sim 10^{12}$  G. By comparing the magnetic microphysical parameters obtained for  $\gamma$ -ray flux with the X-ray, optical and radio observations is shown that the magnetic field in the reverse-shock region would be  $\sim 40$  times higher than the forward shock. It suggests that the outflow carried a significant magnetic field as reported in sGRB 090510 (Frajia et al. 2016b).

The value of the equivalent kinetic energy agrees with simulations performed around the necessary conditions for sGRB production in binary NS mergers (Murguia-Berthier et al. 2014). It suggests the scenario of the collapse to a black hole with the formation of a typical off-axis sGRB favours on that where the wind expelled from HMNS hampers the forward movement of the on-axis jet. Since GRB 170817A was the closest sGRB with measured redshift, it was proposed as potential target for neutrino observation. However, the Antares, IceCube and Auger observatories reported a null result based on a search during the prompt phase and afterglow (ANTARES et al. 2017; Bartos & IceCube Collaboration 2017). As showed in previous works (see i.e., Gao et al. 2013; Frajia et al. 2017b), the lack of energetic neutrinos around GRB 170817A could be related with the degree of the ejecta magnetization which hinders efficiently particle acceleration (Sironi & Spitkovsky 2011).

One of the most energetic short bursts, GRB 090510 located at  $z=0.903$ , was detected by Fermi and Swift satellites (De Pasquale & et al. 2010). This sGRB seen on-axis exhibited a short-lasting peak at the end of the prompt phase ( $T_{90} = 0.3$  s) and a temporally extended component lasting hundreds of seconds. In addition, Ultra Violet and Optical Telescope (UVOT) on board of the Swift satellite started collecting optical data at 97 s after the initial trigger (Kuin & Hoversten 2009). The optical afterglow emission was described by a broken power law with the best-fit parameters: an early decay slope of  $-0.50^{+0.11}_{-0.13}$ , a break time of  $1.58^{+0.46}_{-0.37} \times 10^3$

s, a late decay slope of  $1.13^{+0.11}_{-0.13}$  and density flux of  $\sim 10^{-13} \text{ erg cm}^{-2} \text{ s}^{-1}$  at one day after the trigger. [Fraija et al. \(2016b\)](#) used an early-afterglow model to interpret the multiwavelength light curve observations. In particular, SSC emission from the reverse shock was consistent with the bright LAT peak provided that the progenitor was endowed with strong magnetic fields, thus associating this progenitor with a binary NS merger. The optical light curve was described by synchrotron forward-shock emission in the slow cooling regime before and after the break time. A similar analysis for an off-axis emission was done in this paper for GRB 170817A. The bright  $\gamma$ -ray peak was consistent with SSC radiation in the fast-cooling regime and the multiwavelength afterglow with synchrotron emission in the slow-cooling regime at different regions. Therefore, we argue that an amplification process related to the binary NS merger in GRB 170817A was present. This burst did not display high-energy photons ( $> 100 \text{ MeV}$ ) probably due to the high charged particle background in the burst region ([Kocevski & Fermi-LAT Collaboration 2017](#)), the off-axis emission and low isotropic energy. Gravitational wave observations from a binary NS merger associated with this GRB event ([von Kienlin et al. 2017; Goldstein et al. 2017](#)) cast the compact merger scenario

in new light. Similar analysis to the one presented here on future short GRBs can shed light on the nature of the progenitors, evolution of magnetic field and optical counterpart addressing the short GRB-gravitational wave association.

#### ACKNOWLEDGEMENTS

We thank the referee for a critical reading and significant suggestions that helped improve this manuscript. We also thank E. Ramirez-Ruiz for useful discussions. NF acknowledges financial support from UNAM-DGAPA-PAPIIT through grants IA102917 and IA102019. FDC thanks the UNAM-PAPIIT grants IN117917 and support from the Miztli-UNAM supercomputer (project LANCAD-UNAM-DGTIC-281). PV thanks Fermi grants NNM11AA01A and 80NSSC17K0750, and partial support from OTKA NN 111016 grant. RBD acknowledges support from the National Science Foundation under Grant 1816694. ACCDESCP acknowledges that this study was financed in part by the Coordenação de Aperfeiçoamento de Pessoal de Nível Superior - Brasil (CAPES) - Finance Code 001 and also thanks the Professor Dr. C. G. Bernal for tutoring and useful discussions.

#### REFERENCES

- Abbott, B. P., Abbott, R., Abbott, T. D., & et al. 2017a, Phys. Rev. Lett., 119, 161101
- . 2017b, The Astrophysical Journal Letters, 848, L12
- Ackermann, M., Ajello, M., Asano, K., et al. 2013, ApJS, 209, 11
- Alexander, K. D., Berger, E., Fong, W., et al. 2017, ApJ, 848, L21
- Alexander, K. D., Margutti, R., Blanchard, P. K., et al. 2018, ArXiv e-prints, arXiv:1805.02870
- ANTARES, IceCube, Auger, P., et al. 2017, ArXiv e-prints, arXiv:1710.05839
- Barniol Duran, R., Nakar, E., Piran, T., & Sari, R. 2015, MNRAS, 448, 417
- Bartos, I., & IceCube Collaboration. 2017, GRB Coordinates Network, Circular Service, No. 21568, #1 (2017), 21568
- Berger, E. 2007, ApJ, 670, 1254
- . 2014, ARA&A, 52, 43
- Blandford, R. D., & McKee, C. F. 1976, Physics of Fluids, 19, 1130
- Bromberg, O., Tchekhovskoy, A., Gottlieb, O., Nakar, E., & Piran, T. 2017, ArXiv e-prints, arXiv:1710.05897
- Brun, R., & Rademakers, F. 1997, Nuclear Instruments and Methods in Physics Research A, 389, 81
- Burrows, D. N., Romano, P., Falcone, A., et al. 2005, Science, 309, 1833
- Ciolfi, R., Kastaun, W., Giacomazzo, B., et al. 2017, Phys. Rev. D, 95, 063016
- Coulter, D. A., Foley, R. J., Kilpatrick, C. D., et al. 2017, ArXiv e-prints, arXiv:1710.05452
- D'Avanzo, P., Campana, S., Salafia, O. S., et al. 2018, ArXiv e-prints, arXiv:1801.06164
- De Pasquale, M., & et al. 2010, ApJ, 709, L146
- Derishev, E. V. 2007, Ap&SS, 309, 157
- Dermer, C. D., Chiang, J., & Mitman, K. E. 2000, ApJ, 537, 785
- Dobie, D., Kaplan, D. L., Murphy, T., et al. 2018, ApJ, 858, L15
- Eichler, D., Livio, M., Piran, T., & Schramm, D. N. 1989, Nature, 340, 126
- Fan, Y. Z., & Wei, D. M. 2005, MNRAS, 364, L42
- Fan, Y. Z., Wei, D. M., & Wang, C. F. 2004, A&A, 424, 477
- Foreman-Mackey, D. 2016, The Journal of Open Source Software, 1, doi:10.21105/joss.00024
- Fraija, N. 2015, ApJ, 804, 105
- Fraija, N., González, M. M., & Lee, W. H. 2012, ApJ, 751, 33
- Fraija, N., Lee, W., & Veres, P. 2016a, ApJ, 818, 190
- Fraija, N., Lee, W. H., Araya, M., et al. 2017a, ApJ, 848, 94
- Fraija, N., Lee, W. H., Veres, P., & Barniol Duran, R. 2016b, ApJ, 831, 22
- Fraija, N., & Veres, P. 2018, ArXiv e-prints, arXiv:1803.02978
- Fraija, N., Veres, P., Zhang, B. B., et al. 2017b, ApJ, 848, 15
- Gao, S., Kashiyama, K., & Mészáros, P. 2013, ApJ, 772, L4
- Giacomazzo, B., Rezzolla, L., & Baiotti, L. 2009, MNRAS, 399, L164
- Giblin, T. W., van Paradijs, J., Kouveliotou, C., et al. 1999, ApJ, 524, L47
- Goldstein, A., Veres, P., Burns, E., et al. 2017, ArXiv e-prints, arXiv:1710.05446
- Gottlieb, O., Nakar, E., Piran, T., & Hotokezaka, K. 2017, ArXiv e-prints, arXiv:1710.05896
- Granot, J., Gill, R., Guetta, D., & De Colle, F. 2017, ArXiv e-prints, arXiv:1710.06421
- Granot, J., Panaitescu, A., Kumar, P., & Woosley, S. E. 2002, ApJ, 570, L61
- Guetta, D., Spada, M., & Waxman, E. 2001, ApJ, 557, 399
- Guidorzi, C., Margutti, R., Brut, D., et al. 2017, ArXiv e-prints, arXiv:1710.06426
- Haggard, D., Nynka, M., Ruan, J. J., Evans, P., & Kalogera, V. 2018, The Astronomer's Telegram, 11242
- Hallinan, G., Corsi, A., Mooley, K. P., et al. 2017, ArXiv e-prints, arXiv:1710.05453
- Hotokezaka, K., Kyutoku, K., Tanaka, M., et al. 2013, ApJ, 778, L16
- Hotokezaka, K., & Piran, T. 2015, MNRAS, 450, 1430
- Ioka, K., & Nakamura, T. 2017, ArXiv e-prints, arXiv:1710.05905
- Just, O., Obergaulinger, M., Janka, H.-T., Bauswein, A., & Schwarz, N. 2016, ApJ, 816, L30
- Kasen, D., Badnell, N. R., & Barnes, J. 2013, ApJ, 774, 25
- Kasliwal, M. M., Nakar, E., Singer, L. P., et al. 2017, Science, 358, 1559
- Kathirgamaraju, A., Barniol Duran, R., & Giannios, D. 2017, ArXiv e-prints, arXiv:1708.07488
- Kathirgamaraju, A., Tchekhovskoy, A., Giannios, D., & Barniol Duran, R. 2018, ArXiv e-prints, arXiv:1809.05099
- Kisaka, S., Ioka, K., Kashiyama, K., & Nakamura, T. 2017, ArXiv e-prints, arXiv:1711.00243
- Kobayashi, S. 2000, ApJ, 545, 807
- Kobayashi, S., Piran, T., & Sari, R. 1997, ApJ, 490, 92
- Kobayashi, S., & Zhang, B. 2003, ApJ, 597, 455
- . 2007, ApJ, 655, 973
- Kobayashi, S., Zhang, B., Mészáros, P., & Burrows, D. 2007, ApJ, 655, 391
- Kocevski, D., & Fermi-LAT Collaboration. 2017, GRB Coordinates Network, Circular Service, No. 21534, #1 (2017), 21534
- Kuin, N. P. M., & Hoversten, E. A. 2009, GRB Coordinates Network, 9342, 1
- Kumar, P., & Panaitescu, A. 2000, ApJ, 541, L51
- . 2003, MNRAS, 346, 905
- Kumar, P., & Zhang, B. 2015, Phys. Rep., 561, 1
- Kyutoku, K., Ioka, K., & Shibata, M. 2014, MNRAS, 437, L6
- Lattimer, J. M., & Schramm, D. N. 1974, ApJ, 192, L145
- . 1976, ApJ, 210, 549

- Lazzati, D., Deich, A., Morsony, B. J., & Workman, J. C. 2017a, MNRAS, 471, 1652
- Lazzati, D., López-Cámarra, D., Cantiello, M., et al. 2017b, ApJ, 848, L6
- Lazzati, D., Perna, R., Morsony, B. J., et al. 2017c, ArXiv e-prints, arXiv:1712.03237
- Lee, W. H., & Ramirez-Ruiz, E. 2007, New Journal of Physics, 9, 17
- Lee, W. H., Ramirez-Ruiz, E., & Page, D. 2004, ApJ, 608, L5
- . 2005, ApJ, 632, 421
- Li, L.-X., & Paczyński, B. 1998, ApJ, 507, L59
- Lu, R.-J., Hou, S.-J., & Liang, E.-W. 2010, ApJ, 720, 1146
- Lyman, J. D., Lamb, G. P., Levan, A. J., et al. 2018, ArXiv e-prints, arXiv:1801.02669
- Margutti, R., Fong, W., Eftekhar, T., et al. 2017a, The Astronomer's Telegram, 11037
- Margutti, R., Berger, E., Fong, W., et al. 2017b, ApJ, 848, L20
- Margutti, R., Alexander, K. D., Xie, X., et al. 2018, ArXiv e-prints, arXiv:1801.03531
- McMahon, E., Kumar, P., & Panaiteescu, A. 2004, MNRAS, 354, 915
- McMahon, E., Kumar, P., & Piran, T. 2006, MNRAS, 366, 575
- Mészáros, P. 2006, Reports on Progress in Physics, 69, 2259
- Metzger, B. D. 2017, Living Reviews in Relativity, 20, 3
- Metzger, B. D., Martínez-Pinedo, G., Darbha, S., et al. 2010, MNRAS, 406, 2650
- Mimica, P., Giannios, D., & Aloy, M. A. 2009, A&A, 494, 879
- . 2010, MNRAS, 407, 2501
- Mooley, K. P., Nakar, E., Hotokezaka, K., et al. 2017, ArXiv e-prints, arXiv:1711.11573
- Mooley, K. P., Deller, A. T., Gottlieb, O., et al. 2018, ArXiv e-prints, arXiv:1806.09693
- Mundell, C. G., Steele, I. A., Smith, R. J., et al. 2007, Science, 315, 1822
- Mundell, C. G., Kopac, D., Arnold, D. M., et al. 2013, Nature, 504, 119
- Murguia-Berthier, A., Montes, G., Ramirez-Ruiz, E., De Colle, F., & Lee, W. H. 2014, ApJ, 788, L8
- Murguia-Berthier, A., Ramirez-Ruiz, E., Kilpatrick, C. D., et al. 2017, ApJ, 848, L34
- Nagakura, H., Hotokezaka, K., Sekiguchi, Y., Shibata, M., & Ioka, K. 2014, ApJ, 784, L28
- Nakar, E. 2007, Phys. Rep., 442, 166
- Nakar, E., & Piran, T. 2004, MNRAS, 353, 647
- . 2011, Nature, 478, 82
- Nakar, E., Piran, T., & Granot, J. 2002, ApJ, 579, 699
- Narayan, R., Paczynski, B., & Piran, T. 1992, ApJ, 395, L83
- Nysewander, M., Fruchter, A. S., & Pe'er, A. 2009, ApJ, 701, 824
- Obergaulinger, M., Aloy, M. A., & Müller, E. 2010, A&A, 515, A30
- O'Brien, P. T., Willingale, R., Osborne, J., et al. 2006, ApJ, 647, 1213
- Panaiteescu, A. 2006, MNRAS, 367, L42
- . 2007, MNRAS, 379, 331
- Parsons, R. K., Ramirez-Ruiz, E., & Lee, W. H. 2009, ArXiv e-prints, arXiv:0904.1768
- Peng, Z. Y., Ma, L., Zhao, X. H., et al. 2009, ApJ, 698, 417
- Piran, T. 1999, Phys. Rep., 314, 575
- Piran, T., Nakar, E., & Rosswog, S. 2013, MNRAS, 430, 2121
- Piro, A. L., & Kollmeier, J. A. 2017, ArXiv e-prints, arXiv:1710.05822
- Price, D. J., & Rosswog, S. 2006, Science, 312, 719
- Ramirez-Ruiz, E., Granot, J., Kouveliotou, C., et al. 2005, ApJ, 625, L91
- Rees, M. J. 1999, A&AS, 138, 491
- Rees, M. J., & Meszaros, P. 1994, ApJ, 430, L93
- Rosswog, S. 2005, ApJ, 634, 1202
- Rosswog, S., & Ramirez-Ruiz, E. 2002, MNRAS, 336, L7
- . 2003, MNRAS, 343, L36
- Salvatier J., Wiecki T.V., F. C. . 2016, PeerJ Computer Science
- Sari, R. 1997, ApJ, 489, L37
- Sari, R., & Mészáros, P. 2000, ApJ, 535, L33
- Sari, R., & Piran, T. 1995, ApJ, 455, L143
- Sari, R., Piran, T., & Halpern, J. P. 1999, ApJ, 519, L17
- Sari, R., Piran, T., & Narayan, R. 1998, ApJ, 497, L17
- Sironi, L., & Spitkovsky, A. 2011, ApJ, 726, 75
- Spergel, D. N., Verde, L., Peiris, H. V., et al. 2003, ApJS, 148, 175
- Steele, I. A., Mundell, C. G., Smith, R. J., Kobayashi, S., & Guidorzi, C. 2009, Nature, 462, 767
- Tan, J. C., Matzner, C. D., & McKee, C. F. 2001, ApJ, 551, 946
- Troja, E., Lipunov, V. M., Mundell, C. G., & et al. 2017, Nature, 547, 425
- Troja, E., Piro, L., van Eerten, H., & et al. 2017, Nature, 000, 1
- Troja, E., Piro, L., Ryan, G., et al. 2018, ArXiv e-prints, arXiv:1801.06516
- Usov, V. V. 1992, Nature, 357, 472
- Veres, P., Mészáros, P., Goldstein, A., et al. 2018, ArXiv e-prints, arXiv:1802.07328
- Vestrand, W. T., Wren, J. A., Wozniak, P. R., et al. 2006, Nature, 442, 172
- von Kienlin, A., Meegan, C., & Goldstein, A. 2017, GRB Coordinates Network, Circular Halpern, No. 21520, #1 (2017), 21520
- Wang, X.-Y., & Huang, Z.-Q. 2018, ApJ, 853, L13
- Zhang, B., Fan, Y. Z., Dyks, J., et al. 2006, ApJ, 642, 354
- Zhang, B., & Kobayashi, S. 2005, ApJ, 628, 315
- Zhang, B., Kobayashi, S., & Mészáros, P. 2003, ApJ, 595, 950
- Zhang, B., & Mészáros, P. 2004, International Journal of Modern Physics A, 19, 2385
- Zrake, J., & MacFadyen, A. I. 2013, ApJ, 769, L29

TABLE 1  
SPECTRAL ANALYSIS WITH GBM DATA

Time Interval (s) <sup>a</sup>	Model <sup>b</sup>	$\beta$	$E_{\text{pk}}$ (keV)	kT (keV)	C-Stat/dof
[-0.320 , 0.320]	CPL	-1.016±0.293	338.3±229	-	406.64/361
[0.320 , 0.256]	CPL	-0.955±0.309	331.6±212	-	414.34/361
[0.256 , 0.320]	PL	-1.749±0.434	-	-	296.47/362
[0.320 , 0.448]	PL	-2.150±0.472	-	-	341.51/362
[0.512 , 1.024]	BB	-	-	13.84 ± 4.67	446.40/362
[1.024 , 1.536]	BB	-	-	11.78 ± 2.41	399.07/362
[1.536 , 2.048]	BB	-	-	9.480 ± 1.61	416.05/362

<sup>a</sup> Time interval is given to GBM trigger.

<sup>b</sup> CPL = Comptonized function. PL = Simple power law function. BB= Black-body function

TABLE 2  
FITTED VALUES OF THE  $\gamma$ -RAY DATA.  
THE CHI-SQUARE MINIMIZATIONS ( $\chi^2 / \text{N.D.F.}$ ) ARE REPORTED IN PARENTHESIS

$\gamma$ -ray flux		
Decay slope	$\alpha_\gamma$	$2.85 \pm 0.35$ (4.27/4)
Starting time (s)	$t_0$	$2.0 \pm 0.1$ (4.27/4)
Flux rise timescale (s)	$\tau$	$0.4 \pm 0.1$ (4.27/4)

TABLE 3  
THE MEDIAN AND SYMMETRICAL QUANTILES (0.15, 0.5, 0.85) ARE REPORTED AFTER DESCRIBING THE  $\gamma$ -RAY GBM PEAK WITH OUR MODEL.

Parameters Median	
$\tilde{E} (10^{51} \text{ erg})$	$0.83^{+1.19}_{-0.54}$
n ( $\text{cm}^{-3}$ )	$1.01^{+0.29}_{-0.29}$
$\Gamma_r$	$24.94^{+4.93}_{-4.84}$
p	$2.20^{+0.06}_{-0.06}$
$\Delta\theta (\text{deg})$	$15.01^{+0.68}_{-0.68}$
$\varepsilon_e (10^{-1})$	$3.17^{+0.83}_{-1.16}$
$\varepsilon_{B,r} (10^{-1})$	$1.80^{+1.15}_{-0.78}$

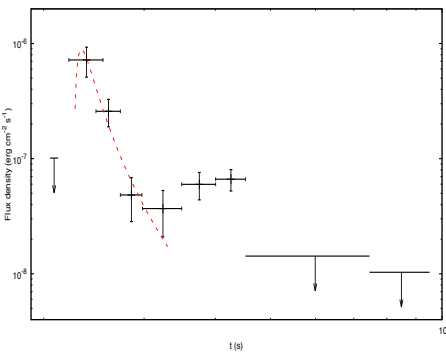


FIG. 1.— GBM light curve and upper limits in the energy range of 10 - 1000 keV of GRB 170817A. The red line corresponds to the best-fit curve using a function  $F(t) \propto \left(\frac{t-t_0}{t_0}\right)^{-\alpha} e^{-\frac{\tau}{t-t_0}}$  (Vestrand et al. 2006).

TABLE 4  
FITTED VALUES OF THE X-RAY, OPTICAL AND RADIO DATA.  
THE CHI-SQUARE MINIMIZATIONS ( $\chi^2 / \text{N.D.F.}$ ) ARE REPORTED IN PARENTHESIS

<b>Light Curve</b>		
<b>X-ray flux</b>		
Rising slope	$\alpha_X$	$0.76 \pm 0.18 (0.45/4)$
<b>Optical flux</b>		
Rising slope	$\alpha_{\text{opt}}$	—
<b>Radio flux</b>		
<b>3 GHz</b>		
Rising slope	$\alpha_{3\text{GHz}}$	$0.85 \pm 0.12 (1.67 / 3)$
<b>6 GHz</b>		
Rising slope	$\alpha_{6\text{GHz}}$	$0.75 \pm 0.19 (11.16 / 6)$
<b>Spectral Energy Distribution</b>		
Spectral slope (16 ± 2 d)	$\beta_{16d}$	$-0.59 \pm 0.11 (3.796 / 7)$
Spectral slope (110 ± 5 d)	$\beta_{110d}$	$-0.58 \pm 0.15 (19.19 / 20)$
Spectral slope (145 ± 20 d)	$\beta_{145d}$	$-0.59 \pm 0.15 (19.19 / 20)$

TABLE 5  
THE MEDIAN AND SYMMETRICAL QUANTILES (0.15, 0.5, 0.85), TRUNCATED AT THE SECOND DECIMAL, ARE REPORTED AFTER DESCRIBING THE X-RAYS AND RADIO WAVELENGTHS AT 3 AND 6 GHz WITH OUR MODEL.

Parameters	Median		
	Radio (3 GHz)	Radio (6 GHz)	X-ray (1 keV)
$\tilde{E} (10^{51} \text{ erg})$	$0.700^{+0.010}_{-0.010}$	$0.700^{+0.010}_{-0.010}$	$0.701^{+0.010}_{-0.010}$
$n (10^{-4} \text{ cm}^{-3})$	$1.010^{+0.010}_{-0.010}$	$1.020^{+0.010}_{-0.010}$	$1.008^{+0.010}_{-0.010}$
p	$2.210^{+0.010}_{-0.010}$	$2.210^{+0.010}_{-0.010}$	$2.230^{+0.010}_{-0.010}$
$\Delta\theta (\text{deg})$	$15.001^{+0.133}_{-0.136}$	$15.001^{+0.137}_{-0.137}$	$15.001^{+0.133}_{-0.136}$
$\varepsilon_e (10^{-1})$	$2.500^{+0.010}_{-0.010}$	$2.500^{+0.010}_{-0.010}$	$2.498^{+0.010}_{-0.010}$
$\varepsilon_{B,f} (10^{-4})$	$1.010^{+0.010}_{-0.010}$	$1.100^{+0.010}_{-0.010}$	$0.997^{+0.010}_{-0.010}$
k	$3.000^{+0.010}_{-0.010}$	$3.000^{+0.010}_{-0.010}$	$2.998^{+0.010}_{-0.010}$
$\alpha_s$	$1.105^{+0.010}_{-0.010}$	$1.095^{+0.010}_{-0.010}$	$1.115^{+0.004}_{-0.007}$

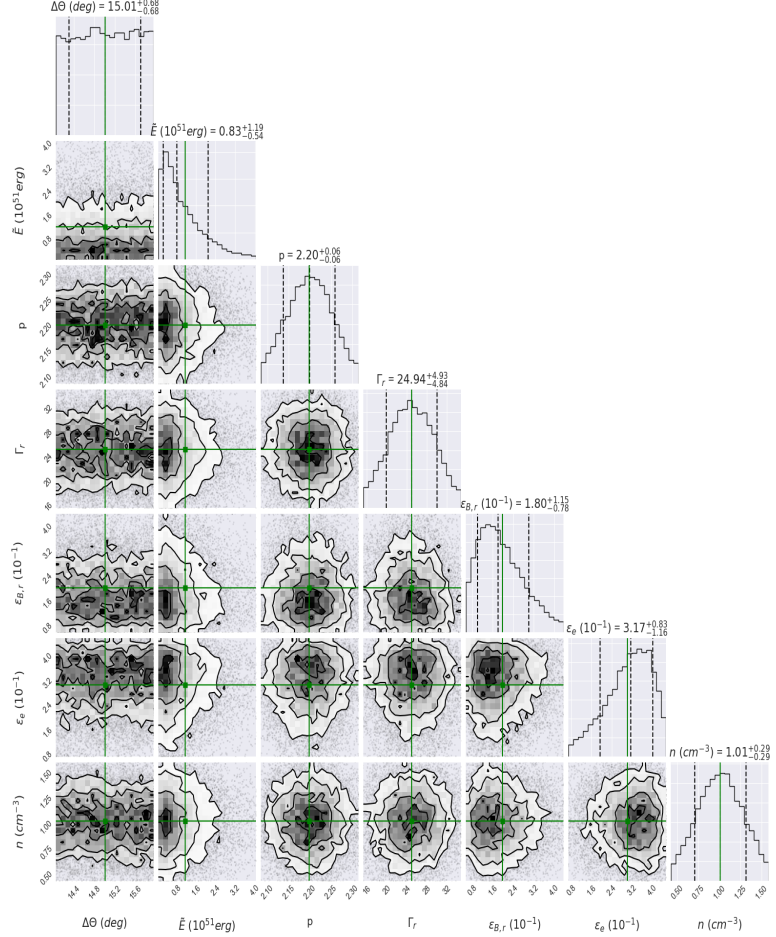


FIG. 2.— Corner plot compares the results obtained from the MCMC simulation for each parameter. Fit result for GBM  $\gamma$ -ray data using a SSC reverse shock model in a homogeneous density as described in section 2.1. Labels above the 1-D kernel plots indicate the median, 0.15 and 0.85 quantiles of each parameter. The best-fit value is shown in green color.

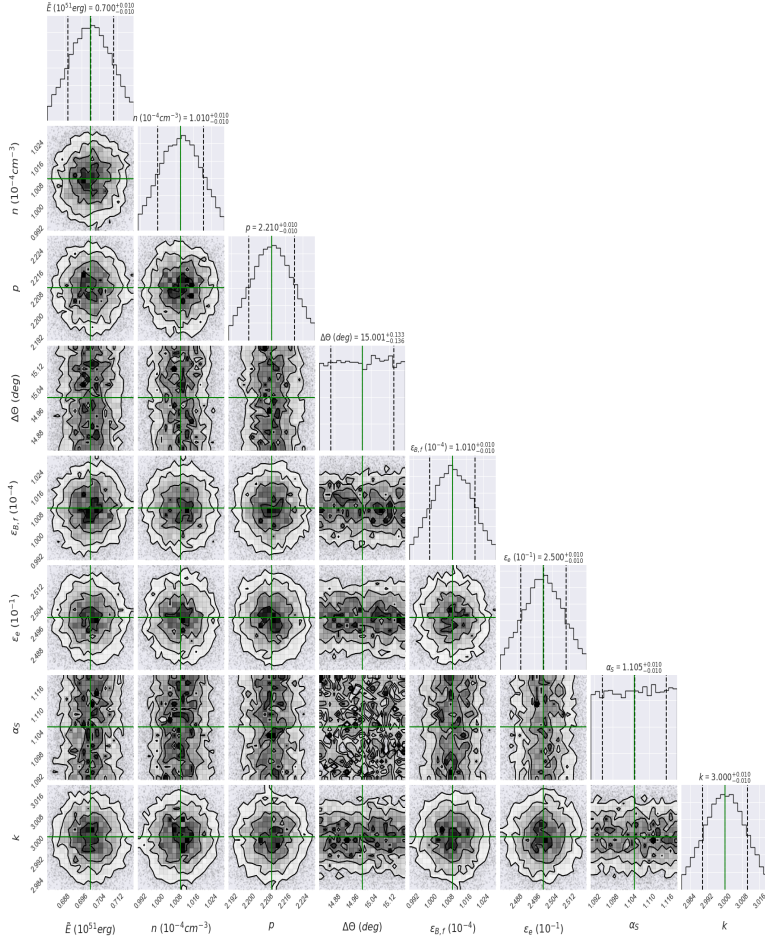


FIG. 3.— Same as Fig. 2, but using a synchrotron forward-shock model to fit the radio (3 GHz) data when the jet producing the afterglow emission is not aligned with the observer’s line of sight and the matter in the outflow is parametrized through a power law velocity distribution (model described in section 2.2).

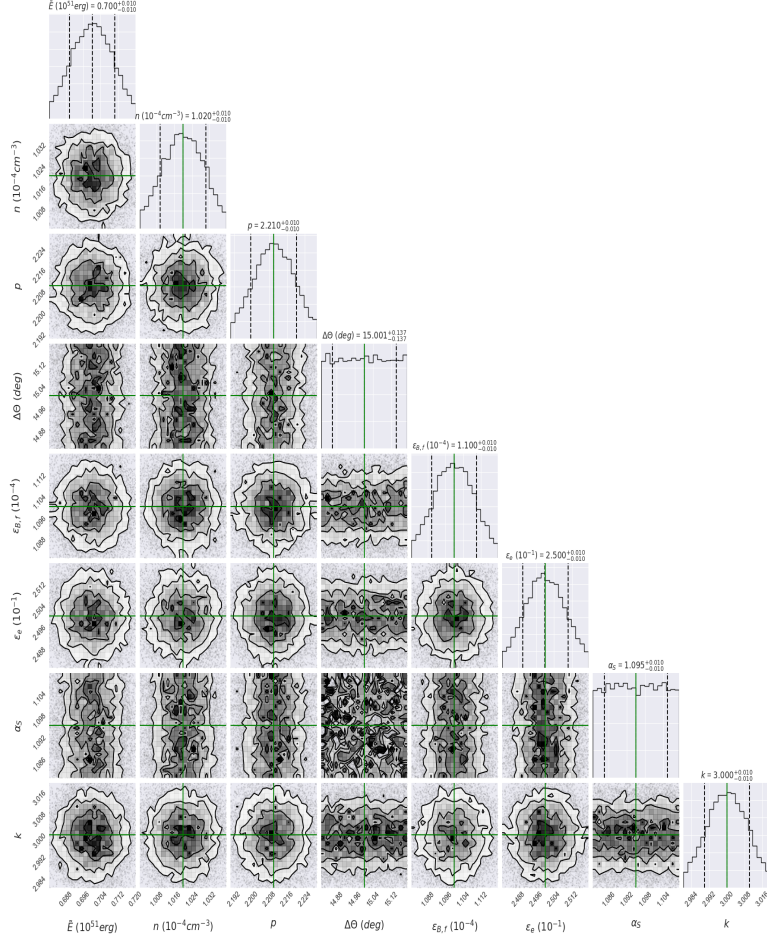


FIG. 4.— Same as Fig. 2, but using a synchrotron forward-shock model to fit the radio (6 GHz) data when the jet producing the afterglow emission is not aligned with the observer’s line of sight and the matter in the outflow is parametrized through a power law velocity distribution (model described in section 2.2).

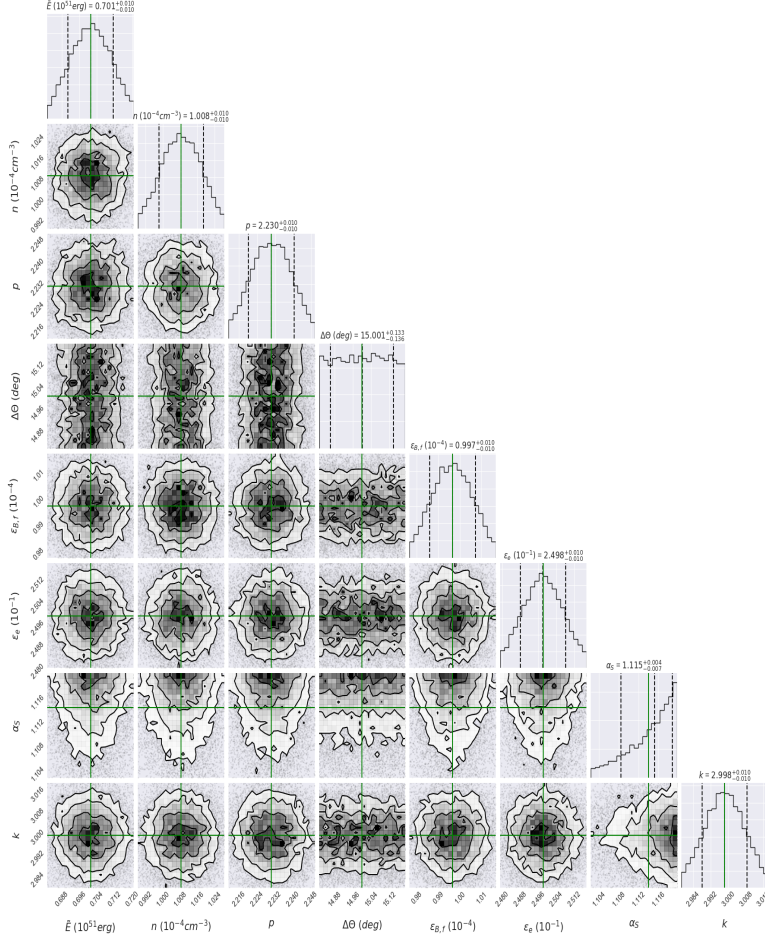


FIG. 5.— Same as Fig. 2, but using a synchrotron forward-shock model to fit the X-ray data when the jet producing the afterglow emission is not aligned with the observer's line of sight and the matter in the outflow is parametrized through a power law velocity distribution (model described in section 2.2).

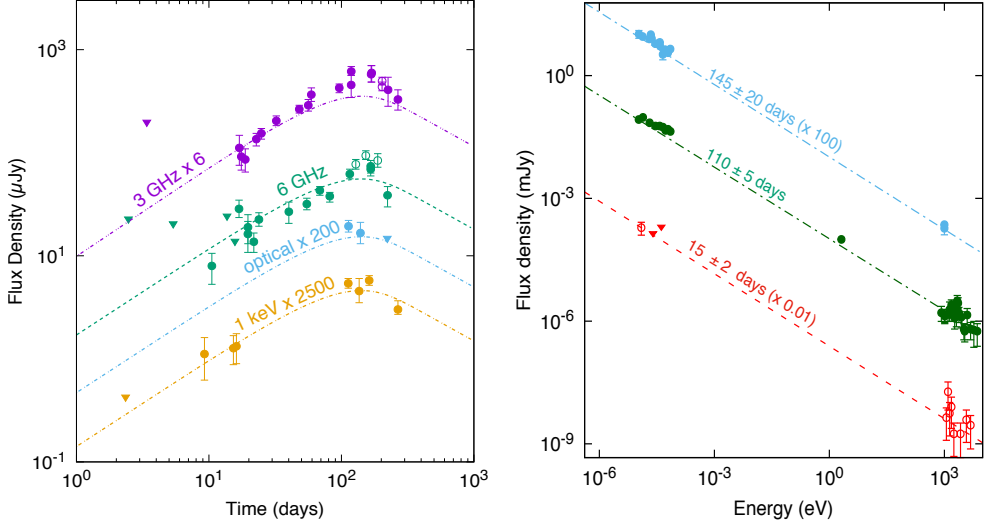


FIG. 6.— Right: SEDs of the X-ray, optical and radio afterglow observations at  $15 \pm 2$  (red),  $110 \pm 5$  (green) and  $145 \pm 20$  (blue) days. Left: Light curves of X-ray at 1 keV (gold; Troja et al. 2017; Margutti et al. 2017b; Haggard et al. 2018; Troja et al. 2017; Troja et al. 2018; Margutti et al. 2018), optical (blue; Margutti et al. 2018), and radio at 3 and 6 GHz (magenta and green; Troja et al. 2017; Hallinan et al. 2017; Mooley et al. 2017; Alexander et al. 2017) bands. The values that describe both the SED and the light curves are reported in Table 5.

DRAFT VERSION DECEMBER 12, 2018  
 Preprint typeset using L<sup>A</sup>T<sub>E</sub>X style emulateapj v. 12/16/11

## LIGHT CURVES OF A SHOCK-BREAKOUT MATERIAL AND A RELATIVISTIC OFF-AXIS JET FROM A BINARY NEUTRON STAR SYSTEM

N. FRAIJA<sup>1†</sup>, A.C. CALIGULA DO E. S. PEDREIRA<sup>1,2</sup> AND P. VERES<sup>3</sup>

<sup>1</sup> Instituto de Astronomía, Universidad Nacional Autónoma de México, Circuito Exterior, C.U., A. Postal 70-264, 04510 Cd. de México, México.

<sup>2</sup> Instituto de Matemática, Estatística e Física, Universidade Federal do Rio Grande, Rio Grande 96203-900, Brasil

<sup>3</sup> Center for Space Plasma and Aeronomy Research (CSPAR), University of Alabama in Huntsville, Huntsville, AL 35899, USA

(Dated: December 12, 2018)  
*Draft version December 12, 2018*

### ABSTRACT

Binary neutron star mergers are believed to eject significant masses with a diverse range of velocities. Once these ejected materials begin to be decelerated by a homogeneous medium, relativistic electrons are mainly cooled down by synchrotron radiation, generating a multiwavelength long-lived afterglow. Analytic and numerical methods illustrate that the outermost matter, the merger shock-breakout material, can be parametrized by power-law velocity distributions  $\propto (\beta_c \Gamma)^{-\alpha_s}$ . Considering that the shock-breakout material is moving on-axis towards the observer and the relativistic jet off-axis, we compute the light curves during the relativistic and the lateral expansion phase. As a particular case, we successfully describe the X-ray, optical and radio light curves alongside the spectral energy distribution from the recently discovered gravitational-wave transient GW170817, when the merger shock-breakout material moves with mildly relativistic velocities near-Newtonian phase and the jet with relativistic velocities. Future electromagnetic counterpart observations of this binary system could be able to evaluate different properties of these light curves.

*Subject headings:* Gamma-rays bursts: individual (GRB 170817A) — Stars: neutron — Gravitational waves — Physical data and processes: acceleration of particles — Physical data and processes: radiation mechanism: nonthermal — ISM: general - magnetic fields

### 1. INTRODUCTION

Binary neutron star (NS) mergers are thought to be natural candidates for gravitational waves (GWs), short gamma-ray bursts (sGRBs), mass ejections producing delayed radio emissions and isotropic quasi-thermal optical/infrared counterparts, so-called kilonova/macronova (for reviews, see Nakar 2007; Berger 2014; Metzger 2017). Kilonova/macronova is related to a neutron-rich mass ejection ( $\sim 10^{-4} - 10^{-2} M_{\odot}$ ) which presents a rapid neutron capture process (r-process) nucleosynthesis (Lattimer & Schramm 1974, 1976). This process synthesizes heavy and unstable nuclei - such as gold and platinum - and consequently heats rapidly the merger ejecta by the radioactive decay energy (Li & Paczyński 1998; Rosswog 2005; Metzger et al. 2010; Kasen et al. 2013; Metzger 2017). SGRBs, with duration less than 2 s, originate from internal collisions or magnetic dissipation within the beamed and relativistic outflow. Delayed radio emission is expected from the interactions of the ejected materials with the circumburst medium (Nakar & Piran 2011; Piran et al. 2013; Hotokezaka & Piran 2015). Kyutoku et al. (2014) proposed the possibility of detecting X-ray, optical and radio fluxes from an ejected ultrarelativistic material decelerated early (from seconds to days) by the interstellar medium (ISM).

The gravitational-wave transient GW170817, associated with a binary NS system with a merger time of 12:41:04 UTC, 2017 August 17, was detected by LIGO and Virgo experiments (Abbott et al. 2017a,b). Immediately, GRB 170817A triggered the Gamma-ray Burst Monitor (GBM) onboard Fermi Gamma-ray Space Telescope at 12:41:06

UTC (Goldstein et al. 2017). The INTErnational Gamma-Ray Astrophysics Laboratory (INTEGRAL) detected an attenuated  $\gamma$ -ray flux with  $\sim 3\sigma$  (Savchenko et al. 2017). GRB 170817A was followed up by multiple ground-based telescopes in different bands. A bright optical i-band flux with magnitude  $17.057 \pm 0.0018$  mag was detected by the 1-meter Swope telescope at Las Campanas Observatory in Chile after 10.87 hours, followed by multiple optical and infrared ground-based telescopes. The X-ray and radio experiments followed-up this burst during the subsequent days after the merger without detecting any signal. Finally, GRB 170817A began to be detected in X-rays on the ninth day by Chandra (Troja et al. 2017; Margutti et al. 2017a; Haggard et al. 2018), in the radio (3 and 6 GHz) bands on day nineteenth by Very Large Array and Atacama Large Millimeter/submillimeter Array (VLA and ALMA, respectively; Alexander et al. 2017) and in the optical band after  $\sim 110$  days (see; Margutti et al. 2018). It is worth highlighting that although optical afterglow was detected from the month of December, quasi-thermal optical emission associated to the kilonova was detected early; around 11 hours after the GBM trigger. The host galaxy associated with this event, NGC 4993, was located at a distance of ( $z \simeq 0.01$ ) 40 Mpc (Coulter et al. 2017; Margutti et al. 2017b).

Whereas several authors have associated the early  $\gamma$ -ray photons to different emission mechanisms (Gottlieb et al. 2017; Bromberg et al. 2017; Kisaka et al. 2017), the X-ray, optical and radio afterglow have been related to the synchrotron forward-shock radiation, when the relativistic off-axis jet and/or cocoon are decelerated in an homogeneous low density medium in the range  $10^{-4} - 10^{-2} \text{ cm}^{-3}$  (Frajia et al. 2017a; Murguia-Berthier et al. 2017; Ioka & Nakamura 2017; Mooley et al. 2017; Lazzati et al. 2017c; Granot et al. 2017a; Alexander et al. 2017; Margutti et al. 2017b; Kasliwal

<sup>†</sup>nifraija@astro.unam.mx

et al. 2017; Piro & Kollmeier 2017; Wang & Huang 2018; Troja et al. 2018).

In this paper, we derive the forward shock dynamics and the synchrotron light curves from the outermost shock-breakout material and the relativistic off-axis jet from a binary NS system. As a particular case, we explain the electromagnetic counterpart detected in the GW170817 transient. Our proposed model uses general arguments of the synchrotron afterglow theory introduced in Sari et al. (1998) and the results obtained numerically in Tan et al. (2001) about the ejected masses from GRB progenitors. This paper is arranged as follows: In Section 2 and 3 we derive the synchrotron forward-shock model generated by the deceleration of the shock-breakout material and the relativistic off-axis jet which were launched from a binary NS merger. In Section 4, we present the data used in this work and describe the electromagnetic counterpart of GW170817 with our synchrotron forward-shock model. In section 5, we discuss the results and present our conclusions.

The convention  $Q_x = Q/10^x$  in c.g.s. units and  $\hbar=c=1$  in natural units will be used. The values of cosmological parameters  $H_0 = 71 \text{ km s}^{-1} \text{ Mpc}^{-1}$ ,  $\Omega_m = 0.27$ ,  $\Omega_\lambda = 0.73$  are adopted (Spergel et al. 2003).

## 2. THE MERGER SHOCK-BREAKOUT MATERIAL

### 2.1. Properties and Considerations

The breakout burst signal properties depend on the mass ( $M_m$ ), radius ( $R_m$ ) and velocity ( $\beta_m$ ) of the merger remnant. Right after the binary NS merger takes place, a shock formed at the interface between the NSs is initially launched from the core towards the crust at sub-relativistic velocities ( $\beta_{b,\text{ini}} \sim 0.25$ ; Kyotoku et al. 2014; Metzger et al. 2015). At this early phase, the shocked material cannot escape from the merged remnant because the initial velocity is less than the escape velocity  $\beta_{b,\text{esc}} \simeq 0.83 \left( \frac{M_m}{3 M_\odot} \right)^{\frac{1}{2}} \left( \frac{15 \text{ km}}{R_m} \right)^{\frac{1}{2}}$ .

Although the shock velocity increases as the crust density decreases ( $\rho \propto r^{-s}$  with  $s \simeq 0.187$  for a polytropic index  $n_p = 3$ ), it will eventually reach the escape velocity. Once the shock has reached half of the escape velocity, it can leave the binary NS merger by converting thermal energy into kinetic energy. At this moment, the shock velocity has increased by a factor of  $0.5\beta_{b,\text{esc}}/\beta_{b,\text{ini}} \simeq \frac{3}{2}$  and the crust density has decreased by  $\simeq (\frac{3}{2})^{-1/s}$ . The ejected mass can be estimated as

$$M_b \simeq 5 \times 10^{-5} M_\odot \left( \frac{M_c}{10^{-2} M_\odot} \right) \left( \frac{R_b}{1 \text{ km}} \right) \left( \frac{15 \text{ km}}{R_b} \right) \left( \frac{\beta_{b,\text{ini}}}{0.25} \right)^{\frac{5}{7}} \times \left( \frac{\beta_{b,\text{esc}}}{0.83} \right)^{-\frac{5}{7}}, \quad (1)$$

where  $M_c$  is the crust mass. Once the merger material has moved for long enough to achieve the near-Newtonian phase, the decelerated material propagates adiabatically with the same effective polytropic index (Meliani & Keppens 2010; van Eerten et al. 2010).

Tan et al. (2001) investigated the acceleration of the shock waves to relativistic and sub-relativistic velocities in the outer matter of an explosion. They found that when the energy of the explosion was concentrated in the outermost ejecta, the blast wave could generate a strong electromagnetic emission. Furthermore, the equivalent kinetic energy of the outermost matter can be expressed as a power-law velocity distribution

given by

$$E_{k,c}(\gtrsim \beta_c \Gamma_c) = \tilde{E} \begin{cases} (\beta_c \Gamma_c)^{-(1.58\gamma_p - 1)} & \text{for } (\beta_c \Gamma_c) \gg 1, \\ (\beta_c \Gamma_c)^{-(5.35\gamma_p - 2)} & \text{for } (\beta_c \Gamma_c) \ll 1, \end{cases} \quad (2)$$

where  $\tilde{E}$  is the fiducial energy and  $\gamma_p = 1 + 1/n_p$  with  $n_p$  the polytropic index. For  $n_p = 3$ , the kinetic equivalent energy is given by

$$E_{k,c}(\gtrsim \beta_c \Gamma_c) \simeq \tilde{E} (\beta_c \Gamma_c)^{-\alpha_s}, \quad (3)$$

with  $\alpha_s = 1.1$  for  $\beta_c \Gamma_c \gg 1$  and  $\alpha_s = 5.2$  for  $\beta_c \Gamma_c \ll 1$ . Once the relativistic shock-breakout material sweeps up enough ISM, the electron population is cooled down emitting synchrotron radiation in the observer's line-of-sight. Assuming that all the energy is confined within an opening angle  $\theta_c \sim 1/\Gamma_c$  (Tan et al. 2001), the equivalent kinetic energy associated to the observed region becomes  $\simeq \frac{E_{k,c}(\gtrsim \Gamma_c)}{2\Gamma_c^2}$  (Nakar & Piran 2018), and therefore from eq. (3) the observed kinetic energy,  $E_{k,c}$ , can be written as

$$E_{k,c}(\gtrsim \beta_c \Gamma_c) \simeq \tilde{E} (\beta_c \Gamma_c)^{-\delta}, \quad (4)$$

with  $\delta = \alpha_s + 2$ . The factor of 2 has been absorbed in the fiducial energy  $\tilde{E}$ . On the other hand, the electromagnetic energy released in the observer's direction can be estimated through the efficiency  $\eta$  and the equivalent kinetic energy  $E_{\text{obs},\gamma} \approx \eta E_{k,c}(\gtrsim \beta_c \Gamma_c) = \eta \tilde{E} (\beta_c \Gamma_c)^{-\delta}$ . Therefore, the efficiency of kinetic to  $\gamma$ -ray energy conversion can be estimated as

$$\eta \simeq \frac{E_{\text{iso},\gamma} (\beta_c \Gamma_c)^\delta}{\tilde{E}}, \quad (5)$$

where  $\tilde{E}$  is a function of total kinetic energy.

### 2.2. Analytical model: Synchrotron forward-shock emission

#### 2.2.1. Relativistic Phase ( $\Gamma_c > 1/\theta_c$ and $\beta_c = 1$ )

The forward shock dynamics when the outflow with a constant equivalent kinetic energy is decelerated by the ISM has been exhaustively explored (see, e.g. Sari et al. 1998). Here, we derive the dynamics of the forward shock when kinetic energy can be described as a power-law velocity distribution parametrized in accordance with eq. (3). Taking into consideration the adiabatic evolution of the shock, the fiducial energy is given by  $\tilde{E} = 4/3\pi\Gamma_c^{2+\delta} R^3 n m_p$  (Blandford & McKee 1976; Sari 1997) where  $n$  is the homogeneous ISM density,  $m_p$  is the proton mass and  $R = \frac{\Gamma_c^2 t}{1+z}$  is the deceleration radius. The deceleration timescale and bulk Lorentz factor are given by

$$t_{\text{dec}} \simeq 4.2 \text{ d} \left( \frac{1+z}{1.02} \right) n_{-4}^{-\frac{1}{\delta+8}} \tilde{E}_{49}^{\frac{1}{\delta+8}} \Gamma_{c,0.5}^{-\frac{\delta+8}{2}}, \quad (6)$$

and

$$\Gamma_c = 3.1 \left( \frac{1+z}{1.02} \right)^{\frac{3}{\delta+8}} n_{-4}^{-\frac{1}{\delta+8}} \tilde{E}_{49}^{\frac{1}{\delta+8}} t_{15d}^{-\frac{3}{\delta+8}}, \quad (7)$$

respectively. Hereafter through this section the value of  $\alpha_s = 3.0$  (Hotokezaka & Piran 2015) is considered.

In the synchrotron forward-shock framework, the accelerated electron population is described by  $\gamma_e \geq \gamma_m : N(\gamma_e) d\gamma_e \propto \gamma_e^{-p} d\gamma_e$ , where  $p = 2.2$  is the electron power index and  $\gamma_m$  is the minimum Lorentz factor given by

$$\gamma_m = 68.4 \epsilon_{e,-1} \left( \frac{1+z}{1.02} \right)^{\frac{3}{\delta+8}} n_{-4}^{-\frac{1}{\delta+8}} \tilde{E}_{49}^{\frac{1}{\delta+8}} t_{15d}^{-\frac{3}{\delta+8}}, \quad (8)$$

with  $\epsilon_e$  being the microphysical parameter associated to the energy fraction given to accelerate electrons. Similarly, it is possible to define the microphysical parameter  $\epsilon_B = \dot{U}_B/U$  (with  $U_B = B'^2/8\pi$ ) associated to the fraction of the energy given to generate and/or amplify the comoving magnetic field, which is given by

$$B' = 0.4 \text{ mG} \left( \frac{1+z}{1.02} \right)^{\frac{3}{\delta+8}} \epsilon_{B,-3}^{\frac{1}{2}} n_{-4}^{\frac{\delta+6}{2(\delta+8)}} \tilde{E}_{49}^{\frac{1}{\delta+8}} t_{15 \text{ d}}^{-\frac{3}{\delta+8}}. \quad (9)$$

Requiring the equality of the deceleration (eq. 6) and synchrotron timescales, the cooling electron Lorentz factor becomes

$$\gamma_c = 2.7 \times 10^8 \left( \frac{1+z}{1.02} \right)^{\frac{\delta-1}{\delta+8}} \epsilon_{B,-3}^{-1} n_{-4}^{-\frac{\delta+5}{\delta+8}} \tilde{E}_{49}^{-\frac{3}{\delta+8}} t_{15 \text{ d}}^{\frac{1-\delta}{\delta+8}}. \quad (10)$$

Comparing the acceleration and synchrotron timescales, the maximum Lorentz factor is

$$\gamma_{\max} = 8.4 \times 10^8 \phi_{-1}^{1/2} \left( \frac{1+z}{1.02} \right)^{\frac{3}{2(\delta+8)}} n_{-4}^{\frac{1}{4}} \tilde{E}_{49}^{\frac{1}{2(\delta+8)}} t_{15 \text{ d}}^{-\frac{3}{2(\delta+8)}}, \quad (11)$$

with  $\phi$  the efficiency parameter (e.g, see Fraija 2015). Given the synchrotron process with eqs. (6 - 10), the synchrotron spectral breaks can be written as

$$\begin{aligned} \epsilon_m &\simeq 1.5 \times 10^{-3} \text{ GHz} \left( \frac{1+z}{1.02} \right)^{\frac{4-\delta}{\delta+8}} \epsilon_{e,-1}^2 \epsilon_{B,-3}^{\frac{1}{2}} n_{-4}^{\frac{\delta}{2(\delta+8)}} \tilde{E}_{49}^{\frac{4}{\delta+8}} \\ &\quad \times t_{15 \text{ d}}^{-\frac{12}{\delta+8}} \\ \epsilon_c &\simeq 28.9 \text{ keV} \left( \frac{1+z}{1.02} \right)^{\frac{\delta-4}{\delta+8}} (1+Y)^{-2} \epsilon_{B,-3}^{-\frac{3}{2}} n_{-4}^{-\frac{16+3\delta}{2(\delta+8)}} \tilde{E}_{49}^{-\frac{4}{\delta+8}} \\ &\quad \times t_{15 \text{ d}}^{-\frac{2\delta+4}{\delta+8}}, \end{aligned} \quad (12)$$

where  $Y$  is the Compton parameter (i.e. see, Fraija et al. 2016). For some purposes, the spectral breaks can be described through the luminosity, which is defined as  $\bar{L} = \tilde{E}/t$ . The maximum flux estimated through the peak spectral power is given by

$$F_{\max} \simeq 3 \times 10^{-3} \text{ mJy} \left( \frac{1+z}{1.02} \right)^{\frac{8-2\delta}{\delta+8}} \epsilon_{B,-3}^{\frac{1}{2}} n_{-4}^{\frac{3\delta+8}{2(\delta+8)}} D_{26.5}^{-2} \tilde{E}_{49}^{\frac{8}{\delta+8}} \\ \times t_{15 \text{ d}}^{\frac{3\delta}{\delta+8}}, \quad (13)$$

where  $D = 100$  Mpc is the luminosity distance to the source. Using the observed synchrotron spectrum in the fast- and slow-cooling regimes with eqs. (6 - 11), the synchrotron light curves in the fast-cooling regime can be written as

$$F_{\nu,f} = \begin{cases} A_{\text{fl}} t_{15 \text{ d}}^{\frac{11\delta+4}{3(\delta+8)}} \left( \frac{\epsilon_\gamma}{6 \text{ GHz}} \right)^{\frac{1}{3}}, & \epsilon_\gamma < \epsilon_c, \\ A_{\text{fm}} t_{15 \text{ d}}^{\frac{\alpha_s-2}{\delta+8}} \left( \frac{\epsilon_\gamma}{1 \text{ eV}} \right)^{-\frac{1}{2}}, & \epsilon_c < \epsilon_\gamma < \epsilon_m, \\ A_{\text{fb}} t_{15 \text{ d}}^{\frac{2\delta+4-6p}{\delta+8}} \left( \frac{\epsilon_\gamma}{1 \text{ keV}} \right)^{-\frac{p}{2}}, & \epsilon_m < \epsilon_\gamma < \epsilon_{\max}, \end{cases} \quad (14)$$

with coefficients given by

$$\begin{aligned} A_{\text{fl}} &= 2.4 \times 10^{-6} \text{ mJy} \left( \frac{1+z}{1.02} \right)^{\frac{28-7\delta}{3(\delta+8)}} (1+Y)^{\frac{2}{3}} \epsilon_{B,-3} n_{-4}^{\frac{20+6\delta}{4(\delta+8)}} \\ &\quad \times D_{26.5}^{-2} \tilde{E}_{49}^{\frac{28}{3(\delta+8)}} \\ A_{\text{fm}} &= 0.6 \text{ mJy} \left( \frac{1+z}{1.02} \right)^{\frac{12-3\delta}{2(\delta+8)}} (1+Y)^{-1} \epsilon_{B,-3}^{-\frac{1}{2}} n_{-4}^{\frac{3\delta}{4(\delta+8)}} \\ &\quad \times D_{26.5}^{-2} \tilde{E}_{49}^{\frac{6}{\delta+8}} \end{aligned}$$

$$A_{\text{fb}} = 3.3 \times 10^{-9} \text{ mJy} \left( \frac{1+z}{1.02} \right)^{\frac{(4-\delta)(p+2)}{2(\delta+8)}} (1+Y)^{-1} \epsilon_{e,-1}^{p-1} \epsilon_{B,-3}^{\frac{p-2}{4}} \\ \times n_{-4}^{\frac{\delta(p+2)}{4(\delta+8)}} D_{26.5}^{-2} \tilde{E}_{49}^{\frac{4+2p}{\delta+8}}. \quad (15)$$

The light curve when synchrotron emission lies in the slow-cooling regime is

$$F_{\nu,s} = \begin{cases} A_{\text{sl}} t_{15 \text{ d}}^{\frac{3\delta+4}{\delta+8}} \left( \frac{\epsilon_\gamma}{6 \text{ GHz}} \right)^{\frac{1}{3}}, & \epsilon_\gamma < \epsilon_m, \\ A_{\text{sm}} t_{15 \text{ d}}^{\frac{3\delta-6(p-1)}{\delta+8}} \left( \frac{\epsilon_\gamma}{1 \text{ eV}} \right)^{-\frac{p-1}{2}}, & \epsilon_m < \epsilon_\gamma < \epsilon_c, \\ A_{\text{sh}} t_{15 \text{ d}}^{\frac{2\delta+4-6p}{\delta+8}} \left( \frac{\epsilon_\gamma}{1 \text{ keV}} \right)^{-\frac{p}{2}}, & \epsilon_c < \epsilon_\gamma, \end{cases} \quad (16)$$

with the coefficients given by

$$\begin{aligned} A_{\text{sl}} &= 3.9 \times 10^{-2} \text{ mJy} \left( \frac{1+z}{1.02} \right)^{\frac{20-5\delta}{3(\delta+8)}} \epsilon_{e,-1}^{-\frac{2}{3}} \epsilon_{B,-3}^{\frac{1}{3}} n_{-4}^{\frac{4\delta+12}{2(\delta+8)}} D_{26.5}^{-2} \\ &\quad \times \tilde{E}_{49}^{\frac{20}{3(\delta+8)}} \\ A_{\text{sm}} &= 3.9 \times 10^{-8} \text{ mJy} \left( \frac{1+z}{1.02} \right)^{\frac{(4-\delta)(p+3)}{2(\delta+8)}} \epsilon_{e,-1}^{p-1} \epsilon_{B,-3}^{\frac{p+1}{4}} n_{-4}^{\frac{16+\delta(p+5)}{4(\delta+8)}} \\ &\quad \times D_{26.5}^{-2} \tilde{E}_{49}^{\frac{6+2p}{\delta+8}} \\ A_{\text{sh}} &= 3.3 \times 10^{-9} \text{ mJy} \left( \frac{1+z}{1.02} \right)^{\frac{(4-\delta)(p+2)}{2(\delta+8)}} (1+Y)^{-1} \epsilon_{e,-1}^{p-1} \epsilon_{B,-3}^{\frac{p-2}{4}} \\ &\quad \times n_{-4}^{\frac{\delta(p+2)}{4(\delta+8)}} D_{26.5}^{-2} \tilde{E}_{49}^{\frac{4+2p}{\delta+8}}. \end{aligned} \quad (17)$$

It is worth noting that when  $\delta = 0$ , the observable quantities derived in Sari et al. (1998) and the light curves of the synchrotron forward-shock emission are recovered (e.g, see Fraija et al. 2016).

### 2.2.2. Lateral Expansion ( $\Gamma_c \sim 1/\theta_c$ and $\beta_c \lesssim 1$ )

In a realistic case, when  $\Gamma_c$  drops below  $\theta_c$  material begins to slow down and expands laterally. The beaming cone of the radiation emitted broaden increasingly up to this cone reaches our field of view ( $\Gamma_c \sim \theta_c^{-1}$ ; Dermer et al. 2000; Granot et al. 2002; Rees 1999; Granot et al. 2017a; Sari et al. 1999). In the lateral expansion phase, the break should occur at

$$t_{\text{br}} = 22.8 \text{ d k} \left( \frac{1+z}{1.02} \right) n_{-4}^{-\frac{1}{3}} \tilde{E}_{49}^{\frac{1}{3}} \beta_c^{-\frac{\alpha_s}{3}} \theta_{c,15^\circ}^{\frac{\alpha_s+6}{3}}, \quad (18)$$

with  $\beta_c \simeq \sqrt{1 - \theta_c^2}$  and  $k$  a parameter that is added to link the maximum value of the observed flux with the jet break by means of the opening and viewing angles (Nakar et al. 2002; Granot et al. 2002). Hereafter through this paper the value of  $k = 1$  will be assumed (Nakar et al. 2002; Granot et al. 2017a).

Once the synchrotron flux reaches our field of view, the synchrotron spectral breaks and the maximum flux become

$$\begin{aligned} \epsilon_m &\simeq 9.7 \times 10^{-3} \text{ GHz} \left( \frac{1+z}{1.02} \right)^{\frac{6-\alpha_s}{\alpha_s+6}} \epsilon_{e,-1}^2 \epsilon_{B,-3}^{\frac{1}{2}} n_{-4}^{\frac{\alpha_s-2}{2(\alpha_s+6)}} \beta_c^{-\frac{4\alpha_s}{\alpha_s+6}} \\ &\quad \times \tilde{E}_{49}^{\frac{4}{\alpha_s+6}} t_{15 \text{ d}}^{-\frac{12}{\alpha_s+6}} \\ \epsilon_c &\simeq 16.6 \text{ keV} \left( \frac{1+z}{1.02} \right)^{\frac{\alpha_s-6}{\alpha_s+6}} (1+Y)^{-2} \epsilon_{B,-3}^{-\frac{3}{2}} n_{-4}^{-\frac{(3\alpha_s+10)}{2(\alpha_s+6)}} \beta_c^{\frac{4\alpha_s}{\alpha_s+6}} \\ &\quad \times \tilde{E}_{49}^{-\frac{4}{\alpha_s+6}} t_{15 \text{ d}}^{-\frac{2\alpha_s}{\alpha_s+6}}, \end{aligned} \quad (19)$$

and

$$F_{\max} \simeq 0.1 \text{ mJy} \left( \frac{1+z}{1.02} \right)^{\frac{12-2\alpha_s}{\alpha_s+6}} \epsilon_{B,-3}^{\frac{1}{2}} n_{-4}^{\frac{2-\alpha_s}{2(\alpha_s+6)}} D_{26.5}^{-2} \beta_c^{-\frac{8\alpha_s}{\alpha_s+6}}$$

$$\times \tilde{E}_{49}^{\frac{8}{\alpha_s+6}} t_{15d}^{-\frac{3(2-\alpha_s)}{\alpha_s+6}}, \quad (20)$$

respectively. Regarding the synchrotron spectrum, synchrotron spectral breaks and maximum flux, the synchrotron light curve in the slow-cooling regime becomes

$$F_\nu = \begin{cases} A_{sl} t_{15d}^{\frac{3\alpha_s-2}{\alpha_s+6}} \left(\frac{\epsilon_\gamma}{6 \text{ GHz}}\right)^{\frac{1}{3}}, & \epsilon_\gamma < \epsilon_m, \\ A_{sm} t_{15d}^{\frac{3(1-\alpha_s-2p)}{\alpha_s+6}} \left(\frac{\epsilon_\gamma}{1 \text{ eV}}\right)^{-\frac{p-1}{2}}, & \epsilon_m < \epsilon_\gamma < \epsilon_c, \\ A_{sh} t_{15d}^{\frac{2(1-\alpha_s-3p)}{\alpha_s+6}} \left(\frac{\epsilon_\gamma}{1 \text{ keV}}\right)^{-\frac{p}{2}}, & \epsilon_c < \epsilon_\gamma, \end{cases} \quad (21)$$

with the coefficients given by

$$\begin{aligned} A_{sl} &= 0.8 \text{ mJy} \left(\frac{1+z}{1.02}\right)^{\frac{30-5\alpha_s}{3(\alpha_s+6)}} \epsilon_{e,-1}^{\frac{2}{3}} \epsilon_{B,-3}^{\frac{1}{3}} n_{-4}^{\frac{4-2\alpha_s}{3(\alpha_s+6)}} D_{26.5}^{-2} \\ &\quad \times \beta_c^{-\frac{20\alpha_s}{3(\alpha_s+6)}} \tilde{E}_{49}^{\frac{20}{3(\alpha_s+6)}} \\ A_{sm} &= 4.5 \times 10^{-6} \text{ mJy} \left(\frac{1+z}{1.02}\right)^{\frac{(6-\alpha_s)(p+3)}{2(\alpha_s+6)}} \epsilon_{e,-1}^{p-1} \epsilon_{B,-3}^{\frac{p+1}{4}} \\ &\quad \times n_{-4}^{\frac{(\alpha_s-2)(p-3)}{4(\alpha_s+6)}} D_{26.5}^{-2} \beta_c^{-\frac{\alpha_s(6+2p)}{\alpha_s+6}} \tilde{E}_{49}^{\frac{6+2p}{\alpha_s+6}} \\ A_{sh} &= 2.9 \times 10^{-7} \text{ mJy} \left(\frac{1+z}{1.02}\right)^{\frac{(6-\alpha_s)(p+2)}{2(\alpha_s+6)}} (1+Y)^{-1} \epsilon_{e,-1}^{p-1} \\ &\quad \times \epsilon_{B,-3}^{\frac{p-2}{4}} n_{-4}^{\frac{p(\alpha_s-2)-2(3\alpha_s+2)}{4(\alpha_s+6)}} D_{26.5}^{-2} \beta_c^{-\frac{\alpha_s(4+2p)}{\alpha_s+6}} \tilde{E}_{49}^{\frac{4+2p}{\alpha_s+6}}. \end{aligned} \quad (22)$$

For  $\alpha_s = 0$ , the observable quantities derived (eqs. 19 and 20) and the synchrotron light curve in the lateral expansion regime are recovered (i.e., see Dermer et al. 2000; Granot et al. 2002; Rees 1999; Granot et al. 2017a; Sari et al. 1999).

### 2.2.3. Non-relativistic Phase ( $\beta_c \ll 1$ )

Once the decelerated material has swept enough ambient medium, it will go into a non-relativistic phase. This transition affects the evolution of the material and in turn the synchrotron light curve. During this phase, the kinetic equivalent energy is  $E_k \propto \beta_c^2 R^3$  with the radius  $R = \beta_c t$ , the magnetic field is  $B' \propto \beta_c$  and the minimum Lorentz factor is  $\gamma_m \propto \beta_c^2$ . Taking into account that the kinetic energy is given as a power law distribution  $E_k \propto \beta_c^{-\alpha_s}$  (eq. 2), then the velocity evolves as  $\beta_c \propto t^{-\frac{3}{5+\alpha_s}}$ . The synchrotron spectral breaks and maximum flux evolve as

$$\begin{aligned} \epsilon_m &\propto \gamma_m^2 B' \propto \beta_c^5 \propto t^{-\frac{15}{\alpha_s+5}}, \\ \epsilon_c &\propto B'^{-3} t^{-2} \propto \beta_c^{-3} t^{-2} \propto t^{-\frac{2\alpha_s+1}{\alpha_s+5}}, \\ F_{\max} &\propto N_e P'_{\max} \propto R^3 B' \propto \beta_c^4 t^3 \propto t^{\frac{3(\alpha_s+1)}{\alpha_s+5}}. \end{aligned} \quad (23)$$

The synchrotron light curve in the slow-cooling regime when the decelerated material lies in the non-relativistic phase becomes

$$F_\nu \propto \begin{cases} t^{\frac{3\alpha_s+8}{\alpha_s+5}} \epsilon_\gamma^{\frac{1}{3}}, & \epsilon_\gamma < \epsilon_m, \\ t^{\frac{6\alpha_s-15p+21}{2(\alpha_s+5)}} \epsilon_\gamma^{-\frac{p-1}{2}}, & \epsilon_m < \epsilon_\gamma < \epsilon_c, \\ t^{\frac{4\alpha_s-15p+20}{2(\alpha_s+5)}} \epsilon_\gamma^{-\frac{p}{2}}, & \epsilon_c < \epsilon_\gamma. \end{cases} \quad (24)$$

It is worth noting that when  $\alpha_s = 0$ , the observable quantities derived and the synchrotron light curve in the non-relativistic regime are recovered (i.e., see Dai & Lu 1999; Huang & Cheng 2003; Livio & Waxman 2000; Huang et al. 1999; Wijers et al. 1997).

## 2.3. Description of the observable quantities

### 2.3.1. X-ray, optical and radio light curves

Figures 1 and 2 display the resulting X-ray, optical and radio light curves of the synchrotron forward-shock emission generated by a decelerated shock-breakout material for several parameter values. The light curves are presented for three electromagnetic bands: X-ray at 1 keV (upper panel), optical at 1 eV (medium panel) and radio (lower panel) at 6 GHz, with the parameter values in the ranges of  $10^{-6} \leq n \leq 1 \text{ cm}^{-3}$ ,  $10^{-4} \leq \epsilon_B \leq 10^{-1}$ ,  $2.2 \leq p \leq 3.6$  and  $2.0 \leq \alpha_s \leq 3.5$ , for the opening angle  $\theta_c = 15^\circ$ , the fiducial kinetic energy of  $\tilde{E} = 10^{50} \text{ erg}$ , the microphysical parameter given to accelerate electrons  $\epsilon_e = 0.1$  and a source located at  $D = 100 \text{ Mpc}$ . The left- and right-hand panels in Figure 1 display the light curves considering the magnetic microphysical parameter  $\epsilon_B = 10^{-2}$  and density  $n = 10^{-2} \text{ cm}^{-3}$ , respectively, for  $p = 2.2$ ,  $\alpha_s = 3.0$ ,  $D = 100 \text{ Mpc}$ ,  $\theta_c = 15^\circ$ ,  $\tilde{E} = 10^{50} \text{ erg}$  and  $\epsilon_e = 0.1$ . Figure 2 shows the light curves considering the power indexes  $\alpha_s = 3.0$  (left-hand panels) and  $p = 2.2$  (right-hand panels), respectively, for  $\epsilon_B = 10^{-2}$ ,  $n = 10^{-2} \text{ cm}^{-3}$ ,  $D = 100 \text{ Mpc}$ ,  $\theta_c = 15^\circ$ ,  $\tilde{E} = 10^{50} \text{ erg}$  and  $\epsilon_e = 0.1$ . Figure 1 shows that X-ray, optical and radio light curves have similar behaviors depending on which power-law segment of the spectrum are evolving. The left-hand panels show that for  $n = 1 \text{ cm}^{-3}$ , light curves do not present peaks, and as density decreases, the peak in the light curves are more notable. The right-hand panels display that radio flux is evolving in the same power law for  $10^{-4} \leq \epsilon_B \leq 10^{-1} \text{ cm}^{-3}$  whereas X-ray and optical fluxes evolve in different power-law segments of the synchrotron spectrum. For instance, the optical flux for  $\epsilon_B = 0.1$  changes the power-law segment during the jet break. After the jet break, it evolves in the second power law while for other values of  $\epsilon_B$  it keeps evolving in the first one. Figure 2 shows that the fluxes are strongly dependent on the values of  $p$  and  $\alpha_s$ . The right-hand panels show that at early times fluxes, in general, are dominated by those generated with small values of  $\alpha_s$  whereas at later times are dominated by those with larger values. The left-hand panels show that as the electron power-law index increases, fluxes, in general, decrease, with the exception of the radio flux at  $\epsilon_\gamma = 6 \text{ GHz}$  for  $p=2.2$ . This is due to the fact that when  $\epsilon_m$  scales as  $(\frac{p-1}{p-2})^2$ , then radio flux for  $p=2.6, 3.2$  and  $3.5$  is in the regime  $\epsilon_\gamma < \epsilon_m$  which in turn does not depend on  $p$  (as shown in these panels for early times) while for  $p=2.2$  is in the regime  $\epsilon_m < \epsilon_\gamma$ . With the passage of time,  $\epsilon_m$  becomes less than 6 GHz and then the radio flux changes to the regime  $\epsilon_m > \epsilon_\gamma$ , firstly for  $p=2.6$ , then for  $p=3.2$  and finally for  $p=3.6$ , as shown in these panels for later times. While radio and optical fluxes peak during the first hundred days, X-ray flux peaks depending the value of  $\alpha_s$ . Furthermore, the right-hand panels show that as  $\alpha_s$  increases, X-ray fluxes peak earlier.

### 2.3.2. Evolution of the spectral breaks

In the previous subsection the X-ray, optical and radio light curves were illustrated for deceleration timescales ranging from hours to one thousand days. In this subsection we

illustrate the evolution of the synchrotron spectral breaks during the first seconds. In this case, the deceleration time is around a few seconds and the bulk Lorentz factor close to one hundred. The ranges of values for the microphysical parameters and ISM used in this analysis are those that allow the cooling spectral breaks to be observed in the energy range covered by Fermi-GBM, Swift-BAT and INTEGRAL. Figure 3 shows the evolution of synchrotron cooling and characteristic energies during the first 10 s for typical values of the magnetic microphysical parameter ( $10^{-2} < \epsilon_B < 10^{-1}$ ; upper panel), the ISM ( $10^{-2} < n < 1 \text{ cm}^{-3}$ ; medium panel) and the fiducial energy ( $10^{49} < \tilde{E} < 10^{51} \text{ erg}$ ; lower panel). The left-hand panels display that  $\epsilon_c$  evolves in the  $\gamma$ -ray band as  $t^{-1.09}$  ( $\alpha_s = 3.0$ ) or  $t^{-1.14}$  ( $\alpha_s = 4.0$ ) and the right-hand panel shows that  $\epsilon_m$  evolves in the IR - optical band as  $t^{-0.92}$  ( $\alpha_s = 3.0$ ) or  $t^{-0.85}$  ( $\alpha_s = 4.0$ ). While the evolution of the cooling spectral break can be potentially detected by instruments such as Fermi-GBM and Swift-BAT, the characteristic spectral break could be detected by Swift-UVOT, 1-meter Swope telescope and other optical telescopes. It is worth noting that our results are different to the evolution of synchrotron cooling  $t^{-0.5}$  and characteristic  $t^{-1.5}$  energies derived when the relativistic jet is decelerated by the ISM (e.g. see, Sari et al. 1998).

### 3. RELATIVISTIC OFF-AXIS JET

We consider that a relativistic jet producing the long-lived afterglow emission is launched from a binary NS system. Additionally, we assume the relativistic jet is not aligned with the observer's line of sight (Murguia-Berthier et al. 2017; Ioka & Nakamura 2017; Lazzati et al. 2017c; Fraija et al. 2017a; Granot et al. 2017a). In order to obtain the quantities for the off-axis emission, the quantities derived in Sari et al. (1998) have to be modified using different boosts. For the off-axis case, given the evolution of the minimum electron Lorentz factor  $\gamma_{m,\text{off}} \propto \Gamma_j$ , the magnetic field  $B' \propto \Gamma_j$ , the cooling electron Lorentz factor  $\gamma_{c,\text{off}} \propto \delta_D^{-1} \Gamma_j^{-2} t^{-1}$ , the number of radiating electrons  $N_{e,\text{off}} \propto R_{\text{off}}^3 \propto (\delta_D \Gamma_j)^3$  (Salmonson 2003), the solid angle  $\Omega_{\text{off}} \propto \delta_D^{-2}$  (Rybicki & Lightman 1986), the maximum power  $P_{\nu,\text{m,off}} \propto \delta_D B'$ , the synchrotron energy breaks and the maximum synchrotron flux evolve as

$$\begin{aligned} \epsilon_{m,\text{off}} &\propto \delta_D B' \gamma_{m,\text{off}}^2 \propto \delta_D \Gamma_j^3, \\ \epsilon_{c,\text{off}} &\propto \delta_D B' \gamma_{c,\text{off}}^2 \propto \Gamma_j^{-3} \delta_D^{-1} t^{-2}, \\ F_{\nu,\text{max,off}} &\propto \frac{N_{e,\text{off}} P_{\nu,\text{m,off}}}{\Omega_{\text{off}}} \propto \delta_D^3 N_{e,\text{off}} B' \propto \delta_D^6 \Gamma_j^4 t^3, \end{aligned} \quad (25)$$

respectively. Therefore, the flux density at a given energy evolves as  $F_{\nu,\text{off}} \propto \delta_D^{\frac{17}{2}} \Gamma_j^3 t^3$  for  $\epsilon_\gamma \leq \epsilon_m$ ,  $\propto \delta_D^{\frac{p+11}{2}} \Gamma_j^{\frac{3p+5}{2}} t^3$  for  $\epsilon_m \leq \epsilon_\gamma \leq \epsilon_c$  and  $\propto \delta_D^{\frac{p+10}{2}} \Gamma_j^{\frac{3p+2}{2}} t^2$  for  $\epsilon_c \leq \epsilon_\gamma$ , where the Doppler factor is  $\delta_D = \delta_D(\Delta\theta) \equiv \frac{1}{\Gamma_j(1-\beta_j \Delta\theta)} \approx \frac{2\Gamma_j}{1+\Gamma_j^2 \Delta\theta^2}$  for  $\Gamma_j \gg 1$  and  $\Delta\theta \ll 1$  with  $\Delta\theta = \theta_{\text{obs}} - \theta_j$ . The value of the flux density for  $\epsilon_m \leq \epsilon_\gamma \leq \epsilon_c$  agrees with the flux reported in Rossi et al. (2002) and Nakar & Piran (2018). It is worth noting that when  $\Delta\theta = 0^\circ$  and  $F_{\nu,\text{max,off}}$  is divided by  $\Omega = 4\pi\delta_D^2$  (Lamb et al. 2018), the relations derived in Sari et al. (1998) are recovered.

In order to find the evolution of the bulk Lorentz factor ( $\Gamma_j$ ) for a decelerated off-axis jet, the kinetic equivalent energy calculated through the Blandford-McKee condition

$E_{k,j} = \frac{4}{3}\pi m_p n R_{\text{off}}^3 \Gamma_j^2$  is obtained as follows. Taking into account the deceleration radius viewed off-axis  $R_{\text{off}} = \frac{\delta_D \Gamma_j}{(1+z)} t^{\frac{1}{2}}$  and the Doppler boost  $\delta_D \simeq \frac{2}{\Gamma_j \Delta\theta^2}$  for  $\Gamma_j^2 \Delta\theta^2 \gg 1$  with the energy limited to the opening angle  $E_{k,j} = \frac{\tilde{E}}{1-\cos\theta_j} \simeq \frac{2\tilde{E}}{\theta_j^2}$  (Granot et al. 2017a), the kinetic energy becomes  $\tilde{E} = \frac{16}{3}\pi m_p (1+z)^{-3} n \theta_j^2 t^3 \Gamma_j^2 \Delta\theta^{-6}$ . In this case, the bulk Lorentz factor evolves as

$$\Gamma_j = 8.3 (1+z)^{\frac{3}{2}} n_{-4}^{-\frac{1}{2}} \tilde{E}_{50}^{\frac{1}{2}} \theta_{j,5^\circ}^{-1} \Delta\theta_{15^\circ}^3 t_{100d}^{-\frac{3}{2}}. \quad (26)$$

Using the bulk Lorentz factor (eq. 26) and eqs. (25), we derive the relevant quantities of forward-shock synchrotron emission radiated in an off-axis jet. The minimum and cooling electron Lorentz factors are given by

$$\begin{aligned} \gamma_{m,\text{off}} &= 212.9 \epsilon_{e,-1} (1+z)^{\frac{3}{2}} n_{-4}^{-\frac{1}{2}} \tilde{E}_{50}^{\frac{1}{2}} \Delta\theta_{15^\circ}^3 \theta_{j,5^\circ}^{-1} t_{100d}^{-\frac{3}{2}}, \\ \gamma_{c,\text{off}} &= 9.1 \times 10^6 (1+z)^{-\frac{1}{2}} (1+Y)^{-1} \epsilon_{B,-4}^{-1} n_{-4}^{-\frac{1}{2}} \tilde{E}_{50}^{-\frac{1}{2}} \Delta\theta_{15^\circ}^{-1} \theta_{j,5^\circ} \\ &\quad \times t_{100d}^{\frac{1}{2}}, \end{aligned} \quad (27)$$

which correspond to a comoving magnetic field given by

$$B' = 1.9 \times 10^{-2} \text{ mG} (1+z)^{\frac{3}{2}} \epsilon_{B,-4}^{\frac{1}{2}} \tilde{E}_{50}^{\frac{1}{2}} \Delta\theta_{15^\circ}^3 \theta_{j,5^\circ}^{-1} t_{100d}^{-\frac{3}{2}}. \quad (28)$$

The synchrotron spectral breaks and the maximum flux can be written as

$$\begin{aligned} \epsilon_{m,\text{off}} &\simeq 1.5 \times 10^{-2} \text{ GHz} (1+z)^2 \epsilon_{e,-1}^2 \epsilon_{B,-4}^{\frac{1}{2}} n_{-4}^{-\frac{1}{2}} \tilde{E}_{50} \Delta\theta_{15^\circ}^{-4} \theta_{j,5^\circ}^{-2} \\ &\quad \times t_{100d}^{-3}, \\ \epsilon_{c,\text{off}} &\simeq 4.1 \text{ keV} (1+z)^{-2} (1+Y)^{-2} \epsilon_{B,-4}^{-\frac{3}{2}} n_{-4}^{-\frac{1}{2}} \tilde{E}_{50}^{-1} \Delta\theta_{15^\circ}^{-4} \theta_{j,5^\circ}^2 \\ &\quad \times t_{100d}^{-1}, \\ F_{\text{max,off}} &\simeq 5.6 \times 10^3 \text{ mJy} (1+z)^{-4} \epsilon_{B,-4}^{\frac{1}{2}} n_{-4}^{\frac{5}{2}} D_{26.5}^{-2} \tilde{E}_{50}^{-1} \Delta\theta_{15^\circ}^{-18} \\ &\quad \times \theta_{j,5^\circ}^2 t_{100d}^6. \end{aligned} \quad (29)$$

Using the observed synchrotron spectrum in the slow-cooling regime with eqs. (29), the synchrotron light curves can be written as

$$F_{\nu,\text{off}} = \begin{cases} A_{s1} t_{100d}^{\frac{1}{3}} \left(\frac{\epsilon_\gamma}{6 \text{ GHz}}\right)^{\frac{1}{3}}, & \epsilon_\gamma < \epsilon_m, \\ A_{sm} t_{100d}^{\frac{3(p-p)}{2}} \left(\frac{\epsilon_\gamma}{1 \text{ eV}}\right)^{-\frac{p-1}{2}}, & \epsilon_m < \epsilon_\gamma < \epsilon_c, \\ A_{sh} t_{100d}^{\frac{16-3p}{2}} \left(\frac{\epsilon_\gamma}{1 \text{ keV}}\right)^{-\frac{p}{2}}, & \epsilon_c < \epsilon_\gamma, \end{cases} \quad (30)$$

with the coefficients given by

$$\begin{aligned} A_{s1} &= 1.8 \times 10^4 \text{ mJy} (1+z)^{-\frac{14}{3}} \epsilon_{e,-1}^{-\frac{2}{3}} \epsilon_{B,-4}^{\frac{1}{3}} n_{-4}^{\frac{8}{3}} D_{26.5}^{-2} \tilde{E}_{50}^{-\frac{4}{3}} \\ &\quad \times \Delta\theta_{15^\circ}^{-\frac{58}{3}} \theta_{j,5^\circ}^{\frac{8}{3}}, \\ A_{sm} &= 1.5 \times 10^{-2} \text{ mJy} (1+z)^{p-5} \epsilon_{e,-1}^{p-1} n_{-4}^{-\frac{(p-11)}{4}} \epsilon_{B,-4}^{\frac{p+1}{4}} D_{26.5}^{-2} \tilde{E}_{50}^{\frac{p-3}{2}} \\ &\quad \times \Delta\theta_{15^\circ}^{2(p-10)} \theta_{j,5^\circ}^{(1-p)}, \end{aligned}$$

<sup>1</sup> For  $\Delta\theta = 0$ , the quantities become  $\delta_D \simeq \Gamma_j$  and  $R_{\text{off}} \simeq R$ , and the equivalent kinetic on-axis energy is recovered (Salmonson 2003).

<sup>2</sup> Other way to derive the equivalent kinetic energy is given as follows. The corresponding kinetic energy viewed off-axis for  $\theta_{\text{obs}} > 2\theta_j$  is given by  $E_{k,j} = \left(\frac{\delta_D(0)}{\delta_D(\Delta\theta)}\right)^3 E_{k,\text{on}}$  (Ioka & Nakamura 2017). Considering the Blandford-McKee condition, the equivalent kinetic off-axis energy is given by  $E_{k,j} = \frac{32}{3}\pi m_p (1+z)^{-3} n t^3 \Gamma_j^8 (1+\Gamma_j^2 \Delta\theta^2)^{-3}$ . Taking into account that energy is limited to the opening angle  $E_{k,j} \simeq \frac{2\tilde{E}}{\theta_j^2}$  (Granot et al. 2017a), the kinetic energy becomes  $\tilde{E} = \frac{16}{3}\pi m_p (1+z)^{-3} n \theta_j^2 t^3 \Gamma_j^2 \Delta\theta^{-6}$  for  $\Gamma_j^2 \Delta\theta^2 \gg 1$ .

$$A_{\text{fh}} = 3.5 \times 10^{-4} \text{ mJy} (1+z)^{p-6} (1+Y)^{-1} \epsilon_{e,-1}^{p-1} \epsilon_{B,-4}^{\frac{p-2}{4}} D_{26.5}^{-2} \\ \times n_{-4}^{-\frac{(p-10)}{4}} \tilde{E}_{50}^{\frac{p-4}{2}} \Delta\theta_{15^\circ}^{2(p-11)} \theta_{j,5^\circ}^{(2-p)}. \quad (31)$$

### 3.1. Lateral expansion

In this case, the beaming cone of the radiation emitted off-axis,  $\Delta\theta$ , broaden increasingly until this cone reaches our field of view ( $\Gamma_j \sim \Delta\theta^{-1}$ ; Granot et al. 2002, 2017a). In the lateral expansion phase, the break in the density flux should occur around

$$t_{\text{br,off}} = 205.6 \text{ d k} \left( \frac{1+z}{1.02} \right) n_{-4}^{-\frac{1}{3}} \tilde{E}_{50}^{\frac{1}{3}} \Delta\theta_{15^\circ}^2, \quad (32)$$

In this phase, the synchrotron spectral breaks and the maximum synchrotron flux are

$$\begin{aligned} \epsilon_{m,\text{off}} &\simeq 7.6 \times 10^{-3} \text{ GHz} (1+z) \epsilon_{e,-1}^2 \epsilon_{B,-4}^{\frac{1}{2}} n_{-4}^{-\frac{5}{6}} \tilde{E}_{50}^{\frac{2}{3}} t_{100\text{d}}^{-2}, \\ \epsilon_{c,\text{off}} &\simeq 2.6 \text{ keV} (1+z)^{-1} (1+Y)^{-2} \epsilon_{B,-4}^{-\frac{3}{2}} n_{-4}^{-\frac{5}{6}} \tilde{E}_{50}^{-\frac{3}{2}}, \\ F_{\text{max,off}} &\simeq 2.5 \times 10^3 \text{ mJy} (1+z)^2 \epsilon_{B,-4}^{\frac{1}{2}} n_{-4}^{\frac{5}{6}} D_{26.5}^{-2} \tilde{E}_{50}^{\frac{5}{3}} t_{100\text{d}}^{-1}. \end{aligned} \quad (33)$$

Given the synchrotron spectrum, the synchrotron spectral breaks and the maximum flux (eq. 33) during this phase, the light curve when in the slow-cooling regime is

$$F_{\nu,\text{off}} = \begin{cases} A_{\text{sl}} t_{100\text{d}}^{-\frac{1}{3}} \left( \frac{\epsilon_\gamma}{6 \text{ GHz}} \right)^{\frac{1}{3}}, & \epsilon_\gamma < \epsilon_m, \\ A_{\text{sm}} t_{100\text{d}}^{-p} \left( \frac{\epsilon_\gamma}{1 \text{ eV}} \right)^{-\frac{p-1}{2}}, & \epsilon_m < \epsilon_\gamma < \epsilon_c, \\ A_{\text{sh}} t_{100\text{d}}^{-p} \left( \frac{\epsilon_\gamma}{1 \text{ keV}} \right)^{-\frac{p}{2}}, & \epsilon_c < \epsilon_\gamma, \end{cases} \quad (34)$$

with the coefficients given by

$$\begin{aligned} A_{\text{sl}} &= 9.9 \times 10^2 \text{ mJy} (1+z)^{\frac{5}{3}} \epsilon_{e,-1}^{-\frac{2}{3}} \epsilon_{B,-4}^{\frac{1}{2}} n_{-4}^{\frac{5}{6}} D_{26.5}^{-2} \tilde{E}_{50}^{\frac{10}{3}}, \\ A_{\text{sm}} &= 4.4 \times 10^{-4} \text{ mJy} (1+z)^{\frac{(p+3)}{2}} \epsilon_{e,-1}^{p-1} \epsilon_{B,-4}^{\frac{p+1}{4}} n_{-4}^{-\frac{(p-3)}{12}}, \\ A_{\text{sh}} &= 1.7 \times 10^{-5} \text{ mJy} (1+z)^{\frac{(p+2)}{2}} (1+Y)^{-1} \epsilon_{e,-1}^{p-1} \epsilon_{B,-4}^{\frac{p-2}{4}} \\ &\quad \times D_{26.5}^{-2} \tilde{E}_{50}^{\frac{(p+3)}{3}}, \\ &\quad \times n_{-4}^{-\frac{(p+2)}{12}} D_{26.5}^{-2} \tilde{E}_{50}^{\frac{(p+2)}{3}}. \end{aligned} \quad (35)$$

The observed fluxes agree with those reported in Granot et al. (2017a).

## 4. CASE OF APPLICATION: GRB 170817A

### 4.1. Multiwavelength Afterglow Observations

*X-ray data.*— During the first week after the GBM trigger, an X-ray campaign was performed without any detections, although upper limits were placed (i.e. see Margutti et al. 2017b; Troja et al. 2017). From the 9th up to 256th day after the GW trigger, X-ray fluxes have been detected by the Chandra and XMM-Newton satellites (Troja et al. 2017; Margutti et al. 2018; Alexander et al. 2018; D’Avanzo et al. 2018; Margutti et al. 2017a; Haggard et al. 2018).

*Optical data*— A thermal electromagnetic counterpart, in the infrared and optical bands, was detected at  $\sim 11$  hours after the GBM trigger (see for e.g. Coulter et al. 2017, and references therein), and after the first detection multiple infrared/optical telescopes followed this event (Smartt et al. 2017). Later, weak optical fluxes ( $m = 26.54 \pm 0.14$ ; Lyman et al. 2018) mag and ( $m = 26.90 \pm 0.25$ ; Margutti et al. 2018) were reported by Hubble Space Telescope (HST) at  $\sim 110$  and 137 days after the GW trigger.

*Radio data.*— The VLA and ALMA reported radio upper limits during the first two weeks after the GW event. On the sixteenth day after the GW trigger, and for more than seven months, the radio flux at 3 and 6 GHz was reported by Very Large Array (VLA; Abbott et al. 2017b; Mooley et al. 2017; Dobie et al. 2018; Troja et al. 2017).

### 4.2. Modelling the afterglow emission

Our afterglow model presented through the shock-breakout material and the off-axis jet is dependent on a set of 8 parameters,  $\Xi_{\text{fow,b}} = \{ \tilde{E}, n, p, \theta_j, \Delta\theta, \epsilon_B, \epsilon_e, \alpha_s \}$ <sup>3</sup>. To find an adequate set of values inside the parameter space we utilize the Markov-Chain Monte Carlo (MCMC) method, a Bayesian statistical technique that allows us to find best-fit values through a sampling process. By using these parameters, we determine a suitable prior distribution, to be utilized alongside a normal likelihood upon which an eight parameter  $\sigma$  is introduced, that allows us to generate samples for the posterior distributions of our on-axis model. We utilize the No-U-Turn Sampler (NUTS) from the PyMC3 python distribution (Salvatier J. 2016) to generate a total 21000 samples, of which 7000 are utilized for tuning and subsequently discarded. In all simulations we have employed a set of normal, continuous, distributions for our priors. With this specific choice we can simulate a more unbiased and uninformative set of priors.

Output is presented in the Figures 4, 5 and 6, alongside Table 1. These figures are Corner Plots (Foreman-Mackey 2016), a specific plot where the diagonal is a one-dimensional kernel density estimation (KDE) describing the posterior distribution and the lower triangle is the bi-dimensional KDE. The best fit value of each parameter is shown in green color. Table 1 reports our chosen quantiles (0.15, 0.5, 0.85) retrieved from inference.

In accordance with the values obtained after describing the multiwavelength light curves and the SEDs at  $15 \pm 2$ ,  $110 \pm 5$  and  $145 \pm 20$  days of GRB170817A, we found that i) for the shock-breakout material the bulk Lorentz factor becomes  $\Gamma_c \simeq 3.1(t/15\text{d})^{-0.24}$ , the equivalent kinetic energy and the observed electromagnetic energy  $E_{k,c} = 3 \times 10^{49} \text{ erg} (\beta_c \Gamma_c)^{-4.3} \simeq 3.8 \times 10^{47} \text{ erg}$  and  $E_{\text{obs},\gamma} = 5.4 \times 10^{46} \text{ erg}$ , respectively, which corresponds to an efficiency of  $\sim 16\%$  and ii) for the relativistic off-axis jet the bulk Lorentz factor becomes  $\Gamma_j \simeq 4.6(t/140\text{d})^{-\frac{3}{2}}$  the equivalent kinetic energy and the released electromagnetic energy are  $E_{k,j} \simeq \frac{2\tilde{E}}{\theta_j^2} \simeq 7.01 \times 10^{51} \text{ erg}$  and  $E_\gamma = 5.4 \times 10^{46} \text{ erg} (1 + \Delta\theta^2 \Gamma_j^2)^3 \simeq 4.8 \times 10^{51} \text{ erg}$ , respectively, which corresponds to an efficiency of  $\sim 11\%$ . For the shock-breakout material, the flux evolves as  $F_\nu \propto t^{0.64}$  for  $\epsilon_m < \epsilon_\gamma < \epsilon_c$  and  $F_\nu \propto t^{0.09}$  for  $\epsilon_c < \epsilon_\gamma$ . The cooling spectral break  $\epsilon_c \sim 11.2 \text{ keV}$  is above the X-ray band and the characteristic break  $\epsilon_m = 0.02 \text{ GHz}$  is below the radio band at 15 days. The X-ray, optical and radio fluxes peak at  $\sim 30$  days, and later they evolve as  $F_\nu \propto t^{-0.76}$ . At  $\sim 500$  s, the X-ray flux will vary from  $\propto t^{-0.76}$  to  $\propto t^{-1.03}$  whereas the optical and radio fluxes will continue evolving as  $F_\nu \propto t^{-0.76}$ . During the non-relativistic phase ( $\beta_c \ll 1$ ), the flux will evolve in accordance with the synchrotron spectrum given in eq. (24). For the relativistic off-axis jet, the cooling

<sup>3</sup> Due to the merger shock-breakout material is viewed on-axis, we have considered that the opening angle could be approximated as  $\theta_c \approx \Delta\theta$

spectral break,  $\epsilon_c \sim 3.5$  keV, is above the X-ray band and the characteristic break,  $\epsilon_m = 0.03$  GHz, is below the radio band at 100 days. During this period, the observed flux increases as  $F_\nu \propto t^{4.2}$  (eq. 34), as predicted in Nakar & Piran (2018). The X-ray, optical and radio fluxes peak at  $\sim 140$  days, and later they evolve as  $F_\nu \propto t^{-2.2}$ .

On the other hand, taking into consideration the GBM data during the first seconds, Veres et al. (2018) showed the evolution of the main peak ( $E_{\text{peak}}$ ) as a function of time, and the luminosity as a function of  $E_{\text{peak}}$ . Using simple power laws in both cases  $E_{\text{peak}} \propto (t - t_0)^k$  and  $L \propto E_{\text{peak}}^q$ , they obtained the best-fit values of  $k = -0.97 \pm 0.35$  for  $t_0 = -0.15 \pm 0.04$  s and  $q = 0.90 \pm 0.10$ . The values of  $k$  and  $q$  are consistent with the evolution of the cooling spectral break (eq. 29)  $\epsilon_c \propto t^{-(1.01-1.13)}$  and  $\tilde{L} \propto \epsilon_c^{\frac{5+8}{2\delta+4}} = \epsilon_c^{0.88-0.93}$  for  $3.0 < \alpha_s < 4.0$ . In order to find the values of parameters that reproduce this evolution, Figure 8 is presented. This figure exhibits the energy peak as a function of time since GW trigger. The red solid line is the fitted simple power law  $E_{\text{peak}} = A_0(t - t_0)^\alpha$  with  $A_0 = 30.2 \pm 7.97$  keV,  $t_0 = -0.15 \pm 0.04$  s,  $\alpha = -0.97 \pm 0.35$ ,  $\chi^2/\text{ndf} = 0.44/4$ . Dashed, dotted and dashed-dotted lines represent the cooling spectral break of our theoretical model for  $\alpha_s = 2.3$  and  $n = 0.6 \text{ cm}^{-3}$  (green line),  $\alpha_s = 3.2$  and  $n = 4 \text{ cm}^{-3}$  (gold line) and  $\alpha_s = 4.2$  and  $n = 12 \text{ cm}^{-3}$  (blue line), respectively. The values used are  $\tilde{E} = 3 \times 10^{49}$  erg,  $\epsilon_B = 10^{-1}$ ,  $\epsilon_e = 10^{-1}$  and  $p = 2.2$ . In all the cases, the cooling spectral break can successfully describe the early evolution of  $E_{\text{peak}}$  for  $1.2 < \alpha_s < 4.2$  and  $0.6 < n < 10 \text{ cm}^{-3}$ . If this is the case, the bulk Lorentz factor begins to change from  $\sim 12$  at a few seconds to  $\sim 3$  around one hundred days. If the cooling spectral break evolution enters the X-ray band, then the density of the circumburst medium must be much higher than the one found to explain the afterglow at tens of days. The high and low values of the ISM found at early and late times, respectively, could be explained through a stratified medium around the merger as discussed in other sGRBs (Wang & Huang 2018; Parsons et al. 2009; Norris et al. 2011).

## 5. DISCUSSION AND CONCLUSION

In the framework of the binary NS system, we have derived the dynamics of the forward shock and the synchrotron light curves from the outermost (shock-breakout) material and the relativistic off-axis jet. The resulting equivalent kinetic energy for the shock-breakout material is given by  $\tilde{E}(\beta_c \Gamma_c)^{-\delta}$  and for the relativistic jet is  $2\tilde{E}/\theta_j^2$ . We have analyzed the case in which the shock-breakout material and the relativistic jet are decelerated by a homogeneous medium and evolve in the fully adiabatic regime. The main differences between both ejected materials lie in the fact that the jet is moving at ultra-relativistic velocities, is narrowly collimated and is observed from a viewing angle. Taking into account the velocity regime, the values obtained of  $\alpha_s$  for the mildly-relativistic shock-breakout material ( $\alpha_s = 2.3$ ) agrees with the description presented by Tan et al. (2001) and the works previously described in Hotokezaka & Piran (2015) and Kyutoku et al. (2014). Considering the observed times of the lateral expansion for the shock-breakout material (eq. 18) and the relativistic off-axis jet (eq. 32), the observed flux of shock-breakout material peaks first due to the emission is

released on-axis from a material described by a power-law velocity distribution. It is worth mentioning that for  $\delta = 0$ , the observable quantities and light curves derived in Sari et al. (1998); Frajia et al. (2016); Dai & Lu (1999); Huang & Cheng (2003); Dermer et al. (2000); Granot et al. (2002); Rees (1999) are recovered. In addition, we have analyzed the shock-breakout material considering the values in the typical ranges: the medium density ( $10^{-6} \leq n \leq 1 \text{ cm}^{-3}$ ), magnetic microphysical parameter ( $10^{-4} \leq \epsilon_B \leq 10^{-1}$ ), power indices ( $2.2 \leq p \leq 3.6$ ) and ( $1.5 \leq \alpha_s \leq 3.5$ ) for a fiducial kinetic energy ( $\tilde{E} = 10^{49} - 10^{50}$  erg), microphysical parameter ( $\epsilon_e = 10^{-1}$ ) for an event located at a luminosity distance of  $D = 100$  Mpc.

For the shock-breakout material we have found that the cooling spectral break evolves in the  $\gamma$ -ray bands and the characteristic break in the IR - optical bands. The cooling (characteristic) spectral break evolves as  $\epsilon_c \propto t^{-(1.0-1.1)}$  ( $\epsilon_m \propto t^{-(0.9-1.0)}$ ), instead of the typical evolution  $\epsilon_c \propto t^{-0.5}$  ( $\epsilon_m \propto t^{-1.5}$ ) suggested by the decelerated jet (Sari et al. 1998). The analysis of the early spectral evolution of the tails as suggested by some authors (e.g. see Giblin et al. 1999; Frajia et al. 2012, 2017b) could illustrate whether the evolution of  $E_{\text{peak}}$  as early observed in  $\gamma$ -ray and optical bands could be generated by external shocks during the prompt phase. In addition, this analysis could reveal the type of scenario (e.g. internal or external shocks), circumburst medium (e.g. homogeneous or stratified), the regime (e.g. adiabatic or radiative) and the geometry of material that has been decelerated.

Considering the multiwavelength campaign dedicated to follow-up the electromagnetic counterpart of GW170817 (The LIGO Scientific Collaboration et al. 2017) and future campaigns, the light curves to be observed in X-rays at 1 keV, optical band at 1 eV and radio wavelength at 6 GHz were derived for the shock-breakout material and the relativistic off-axis jet. We found that fluxes have similar behaviors depending on which power-law segment of the spectrum are evolving. We have shown that they are strongly dependent on the values of  $p$  and  $\alpha_s$ ; at early times fluxes, in general, are dominated by those generated with small values of  $\alpha_s$  whereas at later times are dominated by those with larger values.

In a particular case, we have considered the multiwavelength afterglow observations detected from GW170817 and found the best-fit values of a set of 8 parameters,  $\Xi_{\text{fow,b}} = \{ \tilde{E}, n, p, \theta_j, \Delta\theta, \epsilon_B, \epsilon_e, \alpha_s \}$  for our afterglow model using the MCMC method. For the shock-breakout material, we found that the bulk Lorentz factor becomes  $\Gamma_c \simeq 3.1(t/15 \text{ d})^{-0.24}$  and the equivalent kinetic energy  $\simeq 3.31 \times 10^{47}$  erg which corresponds to an efficiency of  $\sim 16\%$ . The cooling spectral break  $\epsilon_c \sim 19.2$  keV is above the X-ray band and the characteristic break  $\epsilon_m = 1.2 \times 10^{-3}$  GHz is below the radio band at 15 days. The X-ray, optical and radio fluxes peak at  $\sim 30$  days, and later they evolve as  $F_\nu \propto t^{-0.76}$ . At  $\sim 500$  s, the X-ray flux will vary from  $\propto t^{-0.76}$  to  $\propto t^{-1.03}$  whereas the optical and radio fluxes will continue evolving as  $F_\nu \propto t^{-0.76}$ . For the relativistic jet, we found that the bulk Lorentz factor becomes  $\Gamma_j \simeq 4.6(t/140 \text{ d})^{-\frac{3}{2}}$ . The cooling spectral break  $\epsilon_c \sim 3.5$  keV is above the X-ray band and the characteristic break  $\epsilon_m = 0.03$  GHz is below the radio band at 100 days. During this period, the observed flux increases as  $F_\nu \propto t^{4.2}$  (eq. 34), as predicted in Nakar & Piran (2018).

The X-ray, optical and radio fluxes peak at  $\sim 140$  days, and later they evolve as  $F_\nu \propto t^{-2.2}$ .

Recently, [Mooley et al. \(2018\)](#) reported new detections in radio wavelengths collected with Very Long Baseline Interferometry (VLBI). These observations exhibited for almost 150 days (between 75 and 230 days post-merger) superluminal motion with apparent speed of  $\sim 4$ . This provided direct evidence that binary NS system in GW170817 launched a relativistic narrowly collimated jet with an opening angle less  $\lesssim 5^\circ$ , a bulk Lorentz factor of  $\sim 4$  (at the time of measurement), observed from a viewing angle of  $20^\circ \pm 5^\circ$ . Our model is consistent with the results shown by [Mooley et al. \(2018\)](#), which the earlier emission is dominated by the slower shock-breakout material, and the later emission ( $\gtrsim 80$  days post-merger) by a relativistic off-axis jet. Taking into account the values of  $\Delta\theta \simeq 16^\circ$  and  $\theta_j \simeq 5^\circ$  reported in Table 1, the value of the viewing angle  $\theta_{\text{obs}} \sim 21^\circ$  is found, which agrees with that reported in [Mooley et al. \(2018\)](#). The observed flux generated by the deceleration of the mildly-relativistic shock-breakout material dominates at early times ( $\lesssim 50$  days) and the relativistic off-axis jet dominates at later times ( $\gtrsim 80$  days). This behaviour is due to the fact that the mildly-relativistic shock-breakout material is seemed on-axis ( $\theta_c \simeq 16^\circ$ ) whereas the relativistic jet is off-axis with  $\theta_{\text{obs}} > 2\theta_j$ . It is worth mentioning that the values of opening angle, the bulk Lorentz factor and the viewing angle reported by [Mooley et al. \(2018\)](#) also agree with those found in our model.

The binary NS system ejects several materials during the merger. In addition to a relativistic jet and a shock-breakout material, a dynamical ejecta and/or neutrino-driven wind are also launched. Since the relativistic jet makes its way out inside the dynamical ejecta, the energy deposited laterally could create a cocoon. Depending on the duration and the energy deposited by the relativistic jet in the dynamical ejecta, the cocoon will be or not formed ([Murguia-Berthier et al. 2014; Nagakura et al. 2014; Nakar & Piran 2017; Lazzati et al. 2017a,b](#)). If the relativistic jet is launched before the ejecta begins to expand, then its propagation through the dynamical ejecta cannot inflate a cocoon and hence it will be neglected ([Gottlieb et al. 2018](#)). We argue that in GW170817 there was no delay between the explosion (i.e., the ejection of the shock breakout ejecta) and the ejection of the relativistic jet, so the cocoon emission is neglected. In this previous case the delay of  $1.74 \pm 0.05$  s ([Abbott et al. 2017b](#)) found between the NS merger GW chirp signal and the  $\gamma$ -ray flux detected by GBM could be interpreted in terms of the extra path length that radiation travels from the edge of the off-axis jet to an observer in comparison with the GW which is emitted in the observer's direction. This geometrical delay expressed in terms of  $\Delta\theta = 16^\circ$  and the distance from the central engine to the emitting region  $R_\gamma$  is given by (see Figure 1 shown in [Granot et al. 2017b](#))

$$t_{\Delta\theta} = R_\gamma [1 - \cos \Delta\theta] \simeq 1.71 \text{ s } R_{12.1}. \quad (36)$$

It is worth noting that although the jet moves at speed slightly less than the speed of light from the acceleration phase to the internal shocks take place  $R_\gamma$ , this extra delay is neglected  $t_\gamma \simeq R_\gamma \Gamma_j^{-2} \simeq 4.6 \times 10^{-3} \text{ s } R_{\gamma,12.1} \Gamma_{j,2}^{-2}$ . Therefore, the observed delay between the GW signal and the  $\gamma$ -ray flux can be explained in the framework of a geometrical delay  $t_{\Delta\theta}$ . [Tan et al. \(2001\)](#) studied a transrelativistic acceleration model,

in the context of a supernova explosion, and modelled the kinetic energy of the outer material expelled. These authors found that the equivalent kinetic energy of the outermost material could be described through a power-law velocity distribution and also showed that part of it would be given to the circumburst medium, generating a strong electromagnetic emission. [Kyutoku et al. \(2014\)](#) applied the transrelativistic acceleration model to describe the shock-breakout material ejected in the binary NS merger. They showed the kinetic energy distribution of the shock-breakout material for different polytropic indexes  $n = 3, 4$  and  $6$  and masses ejected by the shock breakout  $M_{\text{sh}} = 10^{-4}, 10^{-5}$  and  $10^{-6} M_{\text{sun}}$ . Given the values reported in Table 1, the equivalent kinetic energy is  $E_{k,c} (\gtrsim \beta_c \Gamma_c) \simeq 3 \times 10^{49} \text{ erg } (\beta_c \Gamma_c)^{-2.3} = 3.1 \times 10^{48} \text{ erg}$ , for  $\Gamma_c \simeq 3$ . This value agrees with the most optimistic scenario reported in Figure 2 ( $n=3$  and  $M_{\text{sh}} = 10^{-4} M_{\text{sun}}$ ) by [Kyutoku et al. \(2014\)](#). It is worth noting that although values of higher kinetic energies are difficult to resolve, by recent 3D merger simulations, relevant implications for the NS equation of state must be analyzed with caution.

[Margutti et al. \(2017b\)](#) and [Alexander et al. \(2017\)](#) studied the X-ray and radio light curves of GRB 170817A in a context of standard synchrotron emission from the forward-shock model. Authors concluded that the on-axis afterglow emitted by a jet was ruled out arguing that although this model can describe the X-ray light curve, it fails to comply the upper limits in the radio light curve which varies as  $\propto t^{\frac{1}{2}}$ . We propose that the X-ray, optical and radio fluxes are not emitted from a decelerated jet but from the fraction of the outermost layer moving towards us which evolves with a steeper slope  $F_\nu \propto t^{0.64}$  before the break. The evolution of this model since few days are below the upper limits and consistent with the observations.

The dynamics of different masses ejected from the merger with significant kinetic energies has been investigated as possible electromagnetic emitters ([Hotokezaka et al. 2013; Kyutoku et al. 2014; Hotokezaka & Piran 2015](#)). Authors suggested that the electromagnetic signatures associated with the deceleration of these relativistic and subrelativistic masses by the circumburst medium could be detected from  $\gamma$ -rays to radio wavelengths and could be observed at nearly all the viewing angles. For instance, [Kyutoku et al. \(2014\)](#) considered a power law velocity distribution with  $E \propto \Gamma^{-1.1}$  for  $n_p = 3$  and proposed that the shock-breakout material ejected at ultrarelativistic velocities ( $\Gamma \simeq 40 - 400$ ) could be decelerated emitting early photons by synchrotron radiation which would be detected in current X-ray and radio instruments. [Hotokezaka & Piran \(2015\)](#) studied the dynamics and the radio components emitted by different ejected masses including a dynamical ejected mass and a cocoon. Assuming a breakout material ejected at subrelativistic velocities  $\beta_c \Gamma \simeq 1$  for a velocity distribution of  $E_{k,c} \propto (\beta_c \Gamma_c)^{-3}$  for  $n_p = 3$ , authors showed that in all cases an early electromagnetic component from the decelerated material is expected at the radio wavelengths. The light curves derived in this paper are different to those derived in the above papers. In this paper, we derive the synchrotron light curves generated from the mildly relativistic shock-breakout material and the relativistic off-axis jet when both are decelerated by an homogeneous density for the adiabatic index  $n_p = 3$ . We have shown that at early times before 50 days, the emission originated from the decelerated shock-breakout material dominated and at later

times larger than  $\gtrsim 80$  days the emission is dominated from the off-axis jet. For instance, X-ray flux derived in [Kyutoku et al. \(2014\)](#) only decrease with time as  $\propto t^{-0.42}$ , and in our case X-ray fluxes increase as  $\propto t^{0.64}$  at early times. It is worth noting that masses ejected from a collapsar scenario to describe low-luminosity GRBs also have been considered (e.g. see; [Barniol Duran et al. 2015](#)).

While writing this paper we became aware of a recent preprint ([Nakar & Piran 2018](#)) which explains that the increase in X-ray and radio flux observed in GW170817 could be explained in terms of the synchrotron radiation originated in a decelerated material moving at larger angles. From the observations they obtained values of the bulk Lorentz factor and the isotropic equivalent energy similar to those reported in this paper for GW170817 event.

Electromagnetic counterpart observations from a binary

NS system associated with gravitational waves cast the merger scenario in new light. Similar analysis to the one developed in this paper with futures observations can shed light on the properties of the outer ejected materials.

#### ACKNOWLEDGEMENTS

We thank Enrico Ramirez-Ruiz, Jonathan Granot, Dafne Guetta, Fabio de Colle, Rodolfo Barniol-Duran and Diego Lopez-Camara for useful discussions. NF acknowledges financial support from UNAM-DGAPA-PAPIIT through grants IA102917 and IA102019. ACCDESP acknowledges that this study was financed in part by the Coordenao de Aperfeiamento de Pessoal de Nível Superior - Brasil (CAPES) - Finance Code 001 and also thanks the Professor Dr. C. G. Bernal for tutoring and useful discussions. PV thanks Fermi grants NNM11AA01A and 80NSSC17K0750.

#### REFERENCES

- Abbott, B. P., Abbott, R., Abbott, T. D., & et al. 2017a, Phys. Rev. Lett., 119, 161101
- , 2017b, The Astrophysical Journal Letters, 848, L12
- Alexander, K. D., Berger, E., Fong, W., et al. 2017, ApJ, 848, L21
- Alexander, K. D., Margutti, R., Blanchard, P. K., et al. 2018, ArXiv e-prints, arXiv:1805.02870
- Barniol Duran, R., Nakar, E., Piran, T., & Sari, R. 2015, MNRAS, 448, 417
- Berger, E. 2014, ARA&A, 52, 43
- Blandford, R. D., & McKee, C. F. 1976, Physics of Fluids, 19, 1130
- Bromberg, O., Tchekhovskoy, A., Gottlieb, O., Nakar, E., & Piran, T. 2017, ArXiv e-prints, arXiv:1710.05897
- Coulter, D. A., Foley, R. J., Kilpatrick, C. D., et al. 2017, ArXiv e-prints, arXiv:1710.05452
- Dai, Z. G., & Lu, T. 1999, ApJ, 519, L155
- D'Avanzo, P., Campana, S., Salafia, O. S., et al. 2018, ArXiv e-prints, arXiv:1801.06164
- Dermer, C. D., Chiang, J., & Mitman, K. E. 2000, ApJ, 537, 785
- Dobie, D., Kaplan, D. L., Murphy, T., et al. 2018, ApJ, 858, L15
- Foreman-Mackey, D. 2016, The Journal of Open Source Software, 1, doi:10.21105/joss.00024
- Fraija, N. 2015, ApJ, 804, 105
- Fraija, N., De Colle, F., Veres, P., et al. 2017a, ArXiv e-prints, arXiv:1710.08514
- Fraija, N., González, M. M., & Lee, W. H. 2012, ApJ, 751, 33
- Fraija, N., Lee, W. H., Veres, P., & Barniol Duran, R. 2016, ApJ, 831, 22
- Fraija, N., Veres, P., Zhang, B. B., et al. 2017b, ApJ, 848, 15
- Giblin, T. W., van Paradijs, J., Kouveliotou, C., et al. 1999, ApJ, 524, L47
- Goldstein, A., Veres, P., Burns, E., et al. 2017, ApJ, 848, L14
- Gottlieb, O., Nakar, E., & Piran, T. 2018, MNRAS, 473, 576
- Gottlieb, O., Nakar, E., Piran, T., & Hotokezaka, K. 2017, ArXiv e-prints, arXiv:1710.05896
- Granot, J., Gill, R., Guetta, D., & De Colle, F. 2017a, ArXiv e-prints, arXiv:1710.06421
- Granot, J., Guetta, D., & Gill, R. 2017b, ApJ, 850, L24
- Granot, J., Panaitescu, A., Kumar, P., & Woosley, S. E. 2002, ApJ, 570, L61
- Haggard, D., Nyka, M., Ruan, J. J., Evans, P., & Kalogera, V. 2018, The Astronomer's Telegram, 11242
- Hallinan, G., Corsi, A., Mooley, K. P., et al. 2017, ArXiv e-prints, arXiv:1710.05435
- Hotokezaka, K., Kyutoku, K., Tanaka, M., et al. 2013, ApJ, 778, L16
- Hotokezaka, K., & Piran, T. 2015, MNRAS, 450, 1430
- Huang, Y. F., & Cheng, K. S. 2003, MNRAS, 341, 263
- Huang, Y. F., Dai, Z. G., & Lu, T. 1999, MNRAS, 309, 513
- Ioka, K., & Nakamura, T. 2017, ArXiv e-prints, arXiv:1710.05905
- Kasen, D., Badnell, N. R., & Barnes, J. 2013, ApJ, 774, 25
- Kasliwal, M. M., Nakar, E., Singer, L. P., et al. 2017, Science, 358, 1559
- Kisaka, S., Ioka, K., Kashiyama, K., & Nakamura, T. 2017, ArXiv e-prints, arXiv:1711.00243
- Kyutoku, K., Ioka, K., & Shibata, M. 2014, MNRAS, 437, L6
- Lamb, G. P., Mandel, I., & Resmi, L. 2018, MNRAS, 481, 2581
- Lattimer, J. M., & Schramm, D. N. 1974, ApJ, 192, L145
- , 1976, ApJ, 210, 549
- Lazzati, D., Deich, A., Morsony, B. J., & Workman, J. C. 2017a, MNRAS, 471, 1652
- Lazzati, D., López-Cámarra, D., Cantiello, M., et al. 2017b, ApJ, 848, L6
- Lazzati, D., Perna, R., Morsony, B. J., et al. 2017c, ArXiv e-prints, arXiv:1712.03237
- Li, L.-X., & Paczyński, B. 1998, ApJ, 507, L59
- Livio, M., & Waxman, E. 2000, ApJ, 538, 187
- Lyman, J. D., Lamb, G. P., Levan, A. J., et al. 2018, ArXiv e-prints, arXiv:1801.02669
- Margutti, R., Fong, W., Eftekhari, T., et al. 2017a, The Astronomer's Telegram, 11037
- Margutti, R., Berger, E., Fong, W., et al. 2017b, ApJ, 848, L20
- Margutti, R., Alexander, K. D., Xie, X., et al. 2018, ArXiv e-prints, arXiv:1801.03531
- Meliani, Z., & Keppens, R. 2010, A&A, 520, L3
- Metzger, B. D. 2017, Living Reviews in Relativity, 20, 3
- Metzger, B. D., Bauswein, A., Goriely, S., & Kasen, D. 2015, MNRAS, 446, 1115
- Metzger, B. D., Martínez-Pinedo, G., Darbha, S., et al. 2010, MNRAS, 406, 2650
- Mooley, K. P., Nakar, E., Hotokezaka, K., et al. 2017, ArXiv e-prints, arXiv:1711.11573
- Mooley, K. P., Deller, A. T., Gottlieb, O., et al. 2018, ArXiv e-prints, arXiv:1806.09693
- Murguia-Berthier, A., Montes, G., Ramirez-Ruiz, E., De Colle, F., & Lee, W. H. 2014, ApJ, 788, L8
- Murguia-Berthier, A., Ramirez-Ruiz, E., Kilpatrick, C. D., et al. 2017, ApJ, 848, L34
- Nagakura, H., Hotokezaka, K., Sekiguchi, Y., Shibata, M., & Ioka, K. 2014, ApJ, 784, L28
- Nakar, E. 2007, Phys. Rep., 442, 166
- Nakar, E., & Piran, T. 2011, Nature, 478, 82
- , 2017, ApJ, 834, 28
- , 2018, ArXiv e-prints, arXiv:1801.09712
- Nakar, E., Piran, T., & Granot, J. 2002, ApJ, 579, 699
- Norris, J. P., Gehrels, N., & Scargle, J. D. 2011, ApJ, 735, 23
- Parsons, R. K., Ramirez-Ruiz, E., & Lee, W. H. 2009, ArXiv e-prints, arXiv:0904.1768
- Piran, T., Nakar, E., & Rosswog, S. 2013, MNRAS, 430, 2121
- Piro, A. L., & Kollmeier, J. A. 2017, ArXiv e-prints, arXiv:1710.05822
- Rees, M. J. 1999, A&S, 138, 491
- Rossi, E., Lazzati, D., & Rees, M. J. 2002, MNRAS, 332, 945
- Rosswog, S. 2005, ApJ, 634, 1202
- Rybicki, G. B., & Lightman, A. P. 1986, Radiative Processes in Astrophysics
- Salmonson, J. D. 2003, ApJ, 592, 1002
- Salvatier J., Wiecki T.V., F.C. . 2016, PeerJ Computer Science
- Sari, R. 1997, ApJ, 489, L37
- Sari, R., Piran, T., & Halpern, J. P. 1999, ApJ, 519, L17
- Sari, R., Piran, T., & Narayan, R. 1998, ApJ, 497, L17
- Savchenko, V., Ferrigno, C., Kuulkers, E., et al. 2017, ApJ, 848, L15
- Smartt, S. J., Chen, T.-W., Jerkstrand, A., & et al. 2017, ArXiv e-prints, arXiv:1710.05841
- Spergel, D. N., Verde, L., Peiris, H. V., et al. 2003, ApJS, 148, 175

- Tan, J. C., Matzner, C. D., & McKee, C. F. 2001, ApJ, 551, 946  
The LIGO Scientific Collaboration, the Virgo Collaboration, Abbott, B. P., et al. 2017, ArXiv e-prints, arXiv:1710.05838  
Troja, E., Lipunov, V. M., Mundell, C. G., & et al. 2017, Nature, 547, 425  
Troja, E., Piro, L., van Eerten, H., & et al. 2017, Nature, 000, 1  
Troja, E., Piro, L., Ryan, G., et al. 2018, ArXiv e-prints, arXiv:1801.06516  
van Eerten, H. J., Leventis, K., Meliani, Z., Wijers, R. A. M. J., & Keppens, R. 2010, MNRAS, 403, 300  
Veres, P., Mészáros, P., Goldstein, A., et al. 2018, ArXiv e-prints, arXiv:1802.07328  
Wang, X.-Y., & Huang, Z.-Q. 2018, ApJ, 853, L13  
Wijers, R. A. M. J., Rees, M. J., & Meszaros, P. 1997, MNRAS, 288, L51

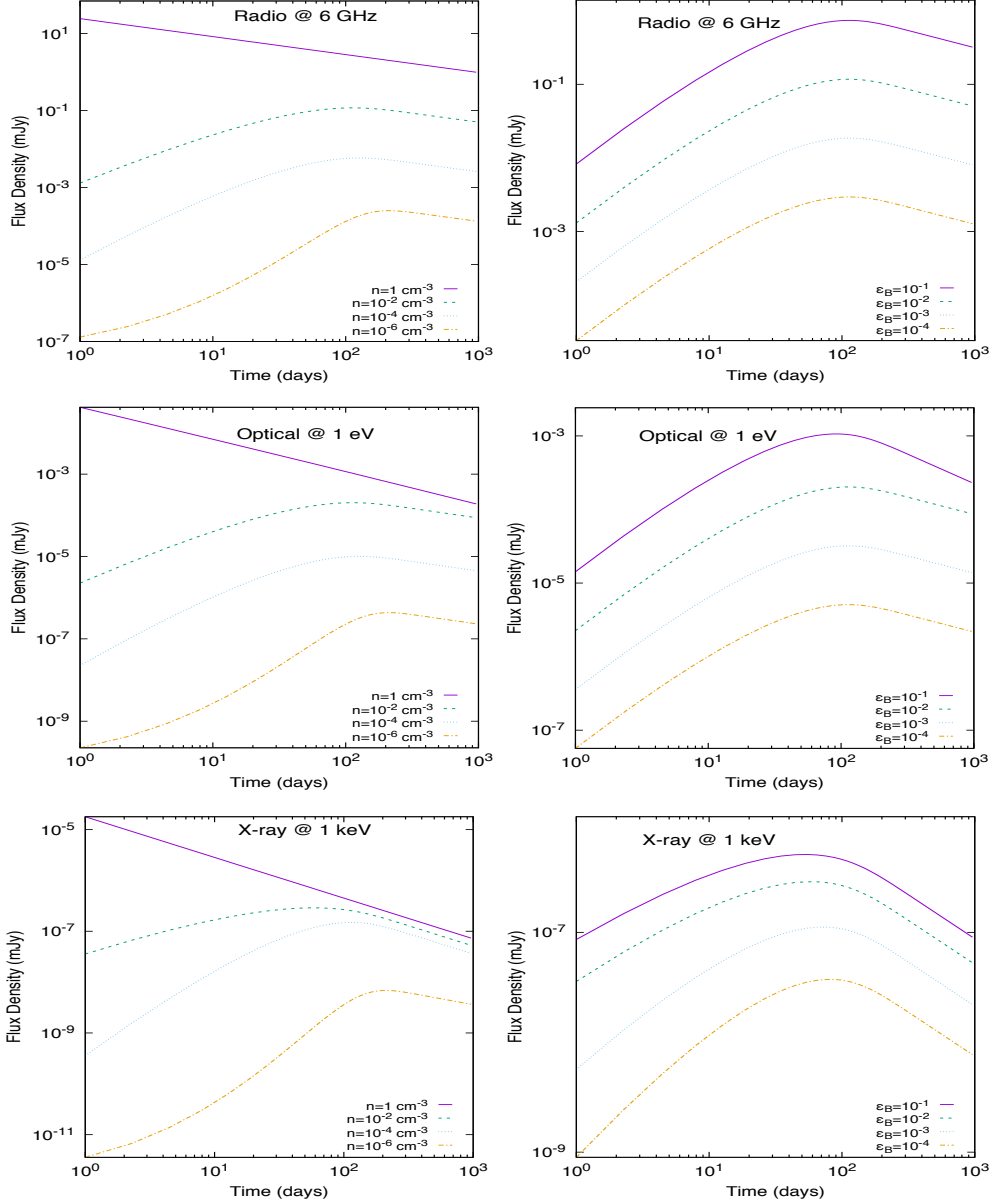


FIG. 1.— Radio (upper), optical (medium) and X-ray (lower) light curves of the synchrotron radiation emitted from the deceleration of the shock-breakout material. The left- and right-hand panels exhibit the light curves considering the magnetic microphysical parameter  $\epsilon_B = 10^{-2}$  and density  $n = 10^{-2} \text{ cm}^{-3}$ , respectively, for the values of fiducial energy  $\bar{E} = 10^{50} \text{ erg}$ , luminosity distance  $D=100 \text{ Mpc}$  and indices  $p = 2.2$ ,  $\alpha_s = 3.0$

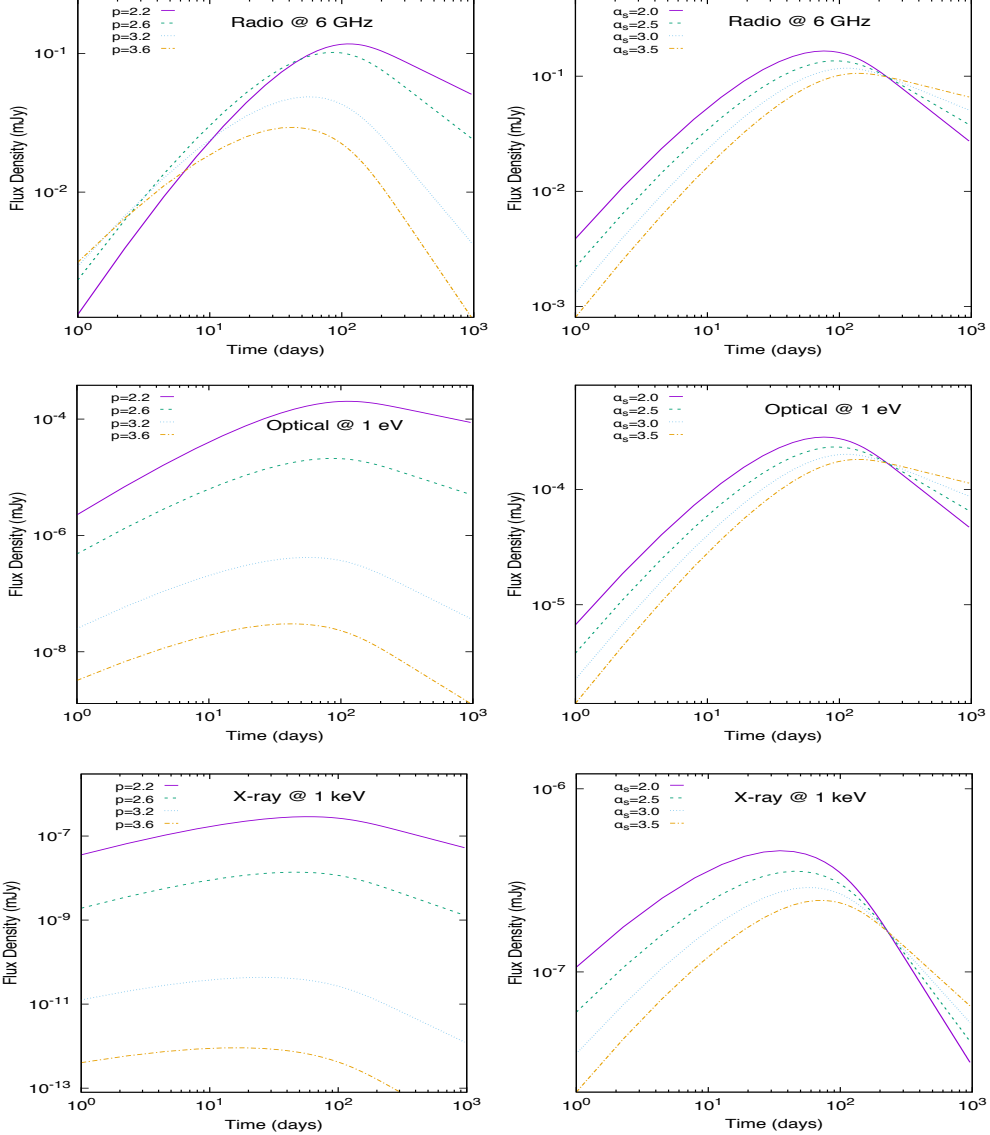


FIG. 2.— Radio (upper panel), optical (medium panel) and X-ray (lower panel) light curves of the synchrotron radiation emitted from the deceleration of the shock-breakout material. The left- and right-hand panels exhibit the light curves considering the indices  $\alpha_s = 3.0$  and  $p = 2.2$ , respectively, for the values of fiducial energy  $\bar{E} = 10^{50}$  erg, luminosity distance  $D = 100$  Mpc,  $n = 10^{-2}$  cm $^{-3}$ ,  $\epsilon_B = 10^{-2}$

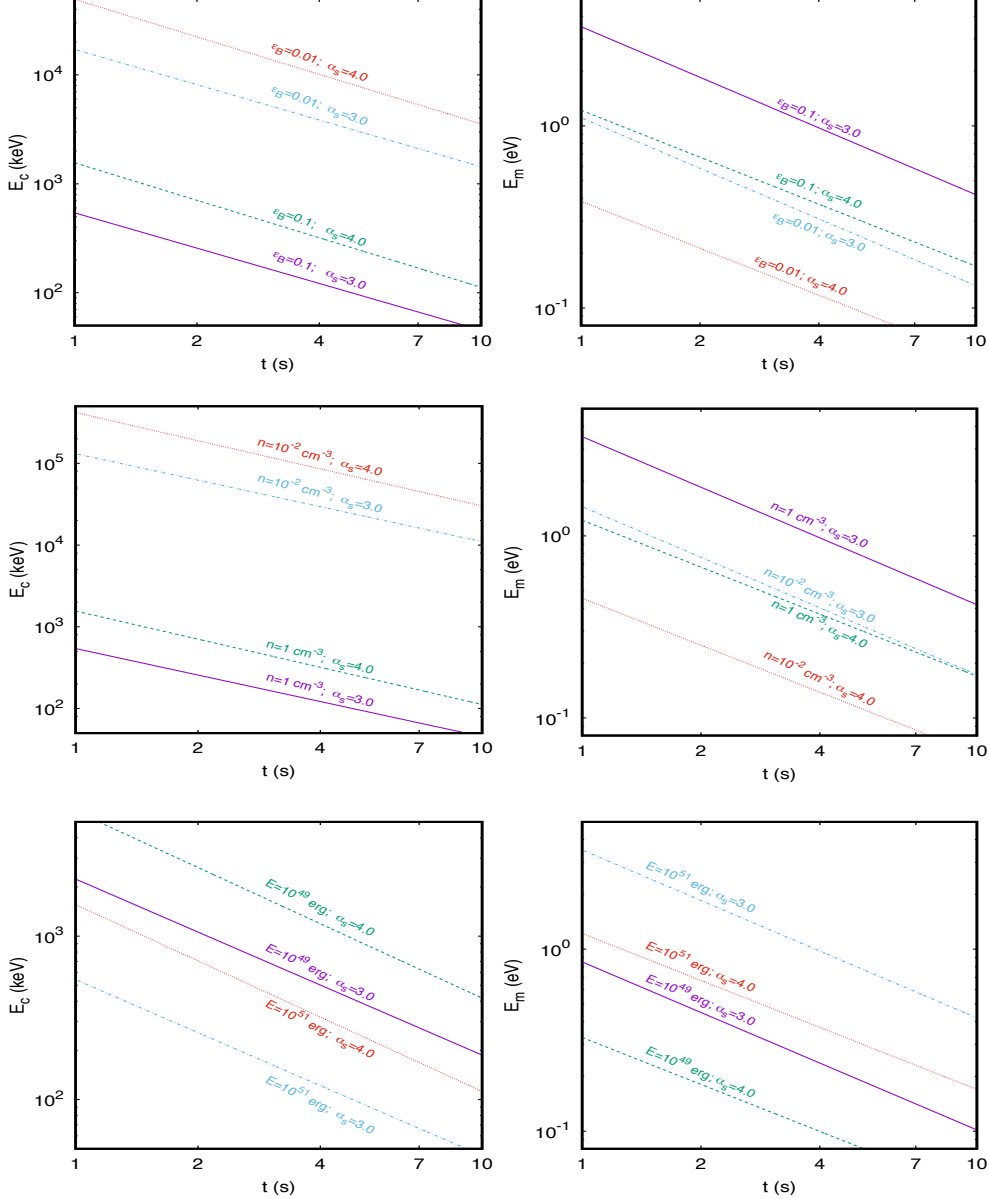


FIG. 3.— Evolution of synchrotron cooling (left-hand panels) and characteristic (right-hand panels) spectral breaks as a function of time for typical values in ranges  $10^{-2} < \epsilon_B < 10^{-1}$  (upper panel),  $10^{-2} < n < 1 \text{ cm}^{-3}$  (medium panel) and  $10^{49} < \dot{E} < 10^{51} \text{ erg}$  (lower panel) considering  $3.0 < \alpha_s < 4.0$  and  $p = 2.2$ .

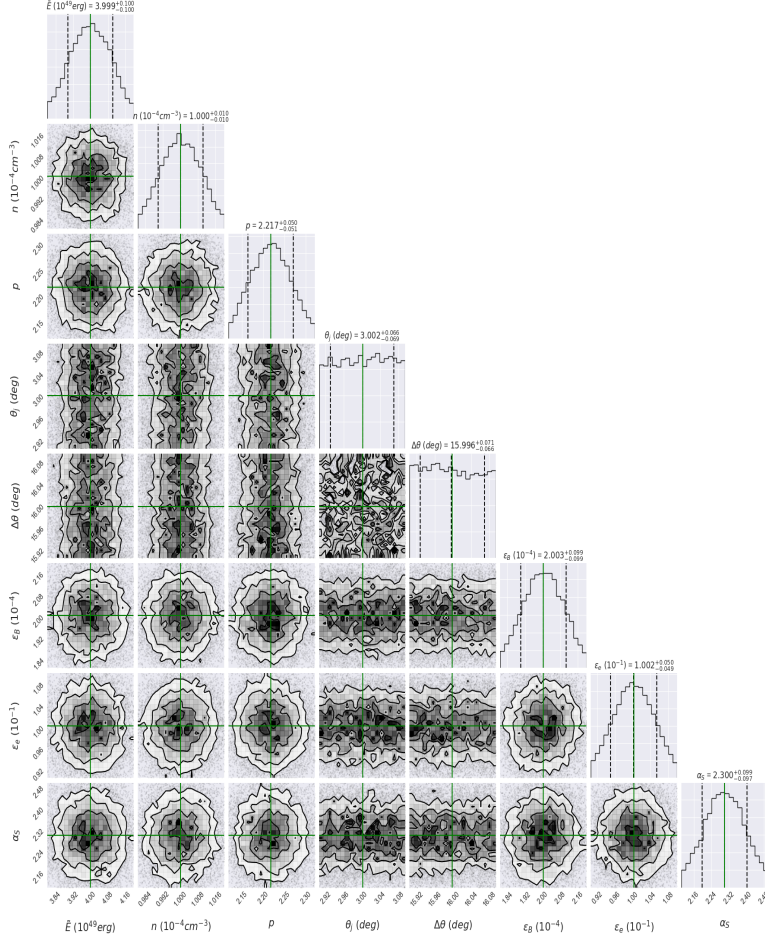


FIG. 4.— Corner plot demonstrating the results obtained from the MCMC simulation for our parameter set. Fit results for the radio light curve at 3 GHz using the synchrotron forward-shock model described in Section 2 and 3. Labels above the 1-D KDE plot indicate the quantiles chosen for each parameter. The best-fit value is shown in green. Values are reported in Table 1 (Col 2).

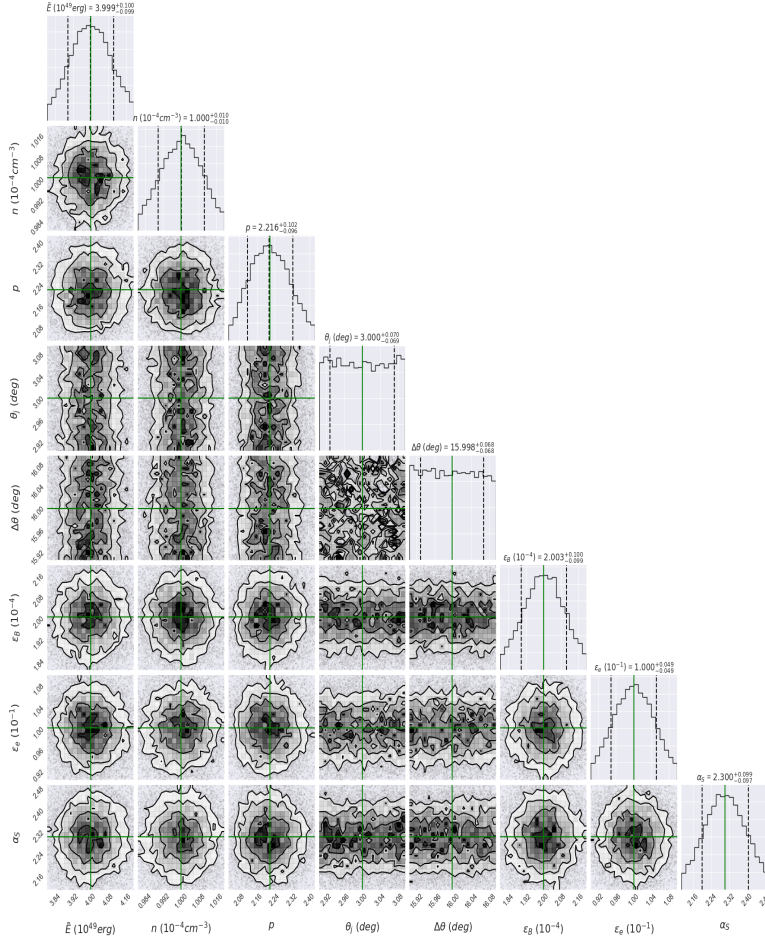


FIG. 5.— Same as Fig. 4, but it shows the fit results for the radio light curve at 6 GHz. Values are reported in Table 1 (Col 3).

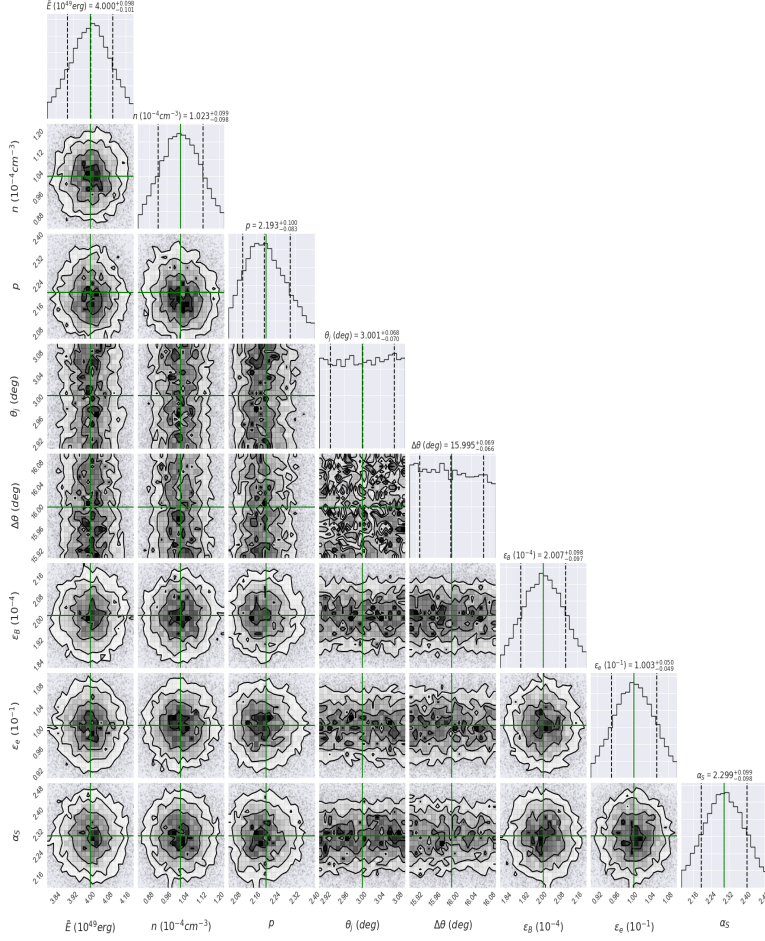


FIG. 6.— Same as Fig. 4, but it shows the fit results for the X-ray light curve. Values are reported in Table 1 (Col 4).

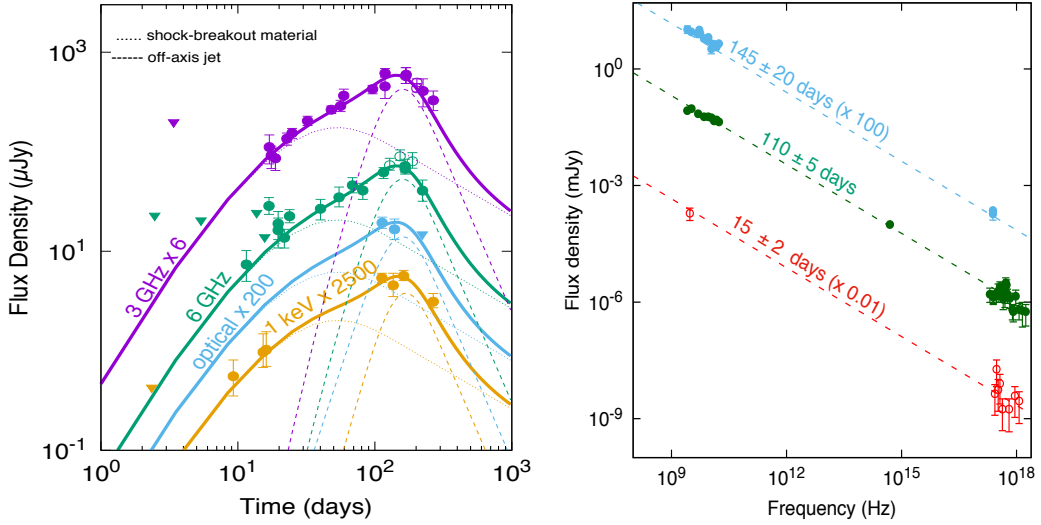


FIG. 7.— Left: Light curves of X-ray at 1 keV (gold; Troja et al. 2017; Margutti et al. 2017b,a; Haggard et al. 2018; Troja et al. 2017; Troja et al. 2018; Margutti et al. 2018), optical (blue; Margutti et al. 2018), and radio at 3 and 6 GHz (magenta and green; Troja et al. 2017; Hallinan et al. 2017; Mooley et al. 2017; Alexander et al. 2017) bands. Right: SEDs of the X-ray, optical and radio afterglow observations at 15 ± 2 (red), 110 ± 5 (green) and 145 ± 20 (blue) days. The values found after describing the light curves and SED are reported in Table 1.

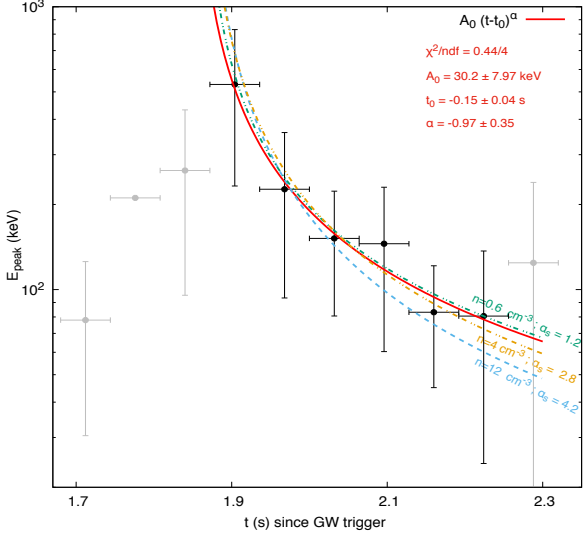


FIG. 8.— Peak energy as a function of time from the GW trigger. The red solid line is the fitted simple power law  $F = A_0(t-t_0)^\alpha$  with  $A_0 = 30.2 \pm 7.97 \text{ keV}$ ,  $t_0 = -0.15 \pm 0.04 \text{ s}$ ,  $\alpha = -0.97 \pm 0.35$ ,  $\chi^2/\text{ndf} = 0.44/4$ . Dashed, dotted and dashed-dotted lines represent the cooling spectral break of our theoretical model for  $\alpha_s = 1.6$  and  $n = 1 \text{ cm}^{-3}$  (green line),  $\alpha_s = 2.8$  and  $n = 4 \text{ cm}^{-3}$  (gold line) and  $\alpha_s = 4.2$  and  $n = 12 \text{ cm}^{-3}$  (blue line), respectively. The values used are  $\tilde{E} = 3 \times 10^{49} \text{ erg}$ ,  $\epsilon_B = 10^{-1}$ ,  $\epsilon_e = 10^{-1}$  and  $p = 2.2$

TABLE 1  
MEDIAN AND SYMMETRICAL 35% QUANTILES (0.15, 0.5, 0.85), TRUNCATED AT THE THIRD DECIMAL, AFTER DESCRIBING THE X-RAYS AND RADIO WAVELENGTHS AT 3 AND 6 GHz WITH OUR AFTERGLOW MODEL AS DESCRIBED IN SECTIONS 2 AND 3.

Parameters	Median		
	Radio (3 GHz)	Radio (6 GHz)	X-ray (1 keV)
$\tilde{E}$ ( $10^{49}$ erg)	$3.999_{-0.100}^{+0.100}$	$3.999_{-0.099}^{+0.100}$	$4.000_{-0.101}^{+0.098}$
n ( $10^{-4}$ cm $^{-3}$ )	$1.000_{-0.010}^{+0.010}$	$1.000_{-0.010}^{+0.010}$	$1.023_{-0.098}^{+0.099}$
p	$2.217_{-0.051}^{+0.050}$	$2.216_{-0.096}^{+0.102}$	$2.193_{-0.083}^{+0.100}$
$\theta_j$ (deg)	$3.002_{-0.069}^{+0.066}$	$3.000_{-0.069}^{+0.070}$	$3.001_{-0.070}^{+0.068}$
$\Delta\theta$ (deg)	$15.996_{-0.066}^{+0.071}$	$15.988_{-0.068}^{+0.068}$	$15.995_{-0.066}^{+0.069}$
$\varepsilon_B$ ( $10^{-4}$ )	$2.003_{-0.099}^{+0.099}$	$2.003_{-0.099}^{+0.100}$	$2.007_{-0.097}^{+0.098}$
$\varepsilon_e$ ( $10^{-1}$ )	$1.002_{-0.049}^{+0.050}$	$1.000_{-0.049}^{+0.049}$	$1.003_{-0.049}^{+0.050}$
$\alpha_s$	$2.300_{-0.097}^{+0.099}$	$2.300_{-0.097}^{+0.099}$	$2.299_{-0.098}^{+0.099}$